NUCLEON AND PION GLUON PARTON DISTRIBUTION FUNCTION FROM LATTICE QCD CALCULATION

By

Zhouyou Fan

A DISSERTATION

Submitted to
Michigan State University
in partial fulfillment of the requirements
for the degree of

Physics – Doctor of Philosophy

2022

ABSTRACT

NUCLEON AND PION GLUON PARTON DISTRIBUTION
FUNCTION FROM LATTICE QCD CALCULATION

By

Zhouyou Fan

Parton distribution functions (PDFs) are important to characterize the structure of the hadrons such as protons and neutrons. The contribution to the structure from quarks has been studied in detail during the past few decades. The structure in the gluon sector is also important but less studied. For high-energy hadrons, the gluon contribution dominates at small x, where x is the momentum fraction carried by a quark or gluon. At large x, the uncertainty of the gluon PDF is large, especially compared to that of the quark PDFs at large x. Gluon PDFs for nucleons and pions are mostly extracted from global analysis of experimental data using perturbation theory as a guide. Theoretically, lattice QCD provides an independent non-perturbative theoretical approach to calculate the gluon PDFs. We present the exploratory study of nucleon gluon PDFs from lattice QCD using the quasi-PDF approach. Using valence overlap fermions on the $2+1$-flavor domain-wall fermion gauge ensemble, the quasi-PDF matrix elements we obtain agree with the Fourier transform of the global-fit PDF within statistical uncertainty. We further study the x-dependent nucleon and pion gluon distributions via the pseudo-PDF approach on lattice ensembles with $2+1+1$ flavors of highly improved staggered quarks (HISQ) generated by the MILC Collaboration. Using clover fermions for the valence action, and adding momentum smearing, PDFs are found for pion boost momenta up to 2.56 GeV. Several lattice sizes and spacings ($a \approx 0.9, 0.12$ and 0.15 fm) were evaluated, resulting in three pion masses, $M_\pi \approx 220$, 310 and 690 MeV/c^2.

ACKNOWLEDGEMENTS

The researches described in this dissertation used resources of the National Energy Research Scientific Computing Center, a DOE Office of Science User Facility supported by the Office of Science of the U.S. Department of Energy under Contract No. DE-AC02-05CH11231 through ERCAP; facilities of the USQCD Collaboration, which are funded by the Office of Science of the U.S. Department of Energy, and supported in part by Michigan State University through computational resources provided by the Institute for Cyber-Enabled Research (iCER). The projects are partially supported by the US National Science Foundation under grant PHY 1653405 "CAREER: Constraining Parton Distribution Functions for New-Physics Searches".

I am deeply grateful to my advisor Professor Huey-Wen Lin for the thorough mentor-ship during my graduate study. I am not able to graduate within 5 years without her continual support and suggestions in daily research, rigorous work attitude and time arrangement.

I would like to thank Yi-Bo Yang for his help in the first exploratory study of gluon PDF and his patiently introduction of some basic ideas on LQCD and coding, Jian-Hui Zhang and Jiunn-Wei Chen for earlier discussions on the gluon quasi-PDF, Rui Zhang for useful discussions in the earlier stage of gluon pseudo-PDF study, Alejandro Salas and Santanu Mondal for their comments on this dissertation.

I thank MILC Collaboration for sharing the lattices used to perform this study. The LQCD calculations were performed using the Chroma software suite [1]. I thank JAM Collaboration for providing us the pion $xg(x)$ data with uncertainties for comparison.

Moreover, I would like to say thank you to my committee members, Professor Chien-Peng Yuan, Professor Scott Pratt, Professor Alexei Bazavov and Professor Joey Huston for their guidance and support.

Finally, I have my special thanks to my parents, who have encouraged me throughout my graduate career, especially when I felt depressed.

TABLE OF CONTENTS

LIST OF TABLES

LIST OF FIGURES

I. Introduction to Parton distribution functions (PDFs)

Parton Distribution Functions (PDFs) represent the probability density to find a parton carrying a momentum fraction x at energy scale μ, where the parton is quark or gluon inside a hadron. PDFs are important inputs for the calculations of the strong and weak interactions, one of the four fundamental forces. Therefore, the accuracy of the PDFs determines the accuracy of these calculations.

Gluons play an important role in binding quarks and the generation of most of the mass of light quark hadrons through the mechanism of dynamical breaking of chiral symmetry (DCSB). The gluon nucleon spin and momentum fractions are about $35-50\%$ at 2 GeV scale [29, 30, 31]. In current PDF analyses, gluon PDF dominates at low-x region especially at large scale μ. Gluon PDF $g(x)$ contributes to the next-to-leading order (NLO) in the deep inelastic scattering (DIS) cross section, and enters at leading order in jet production [32, 33]. To calculate the cross section for these processes in pp collisions, $g(x)$ needs to be known precisely. In this thesis, we mainly focus on the unpolarized nucleon and pion gluon PDFs.

I.1. unpolarized nucleon gluon PDFs

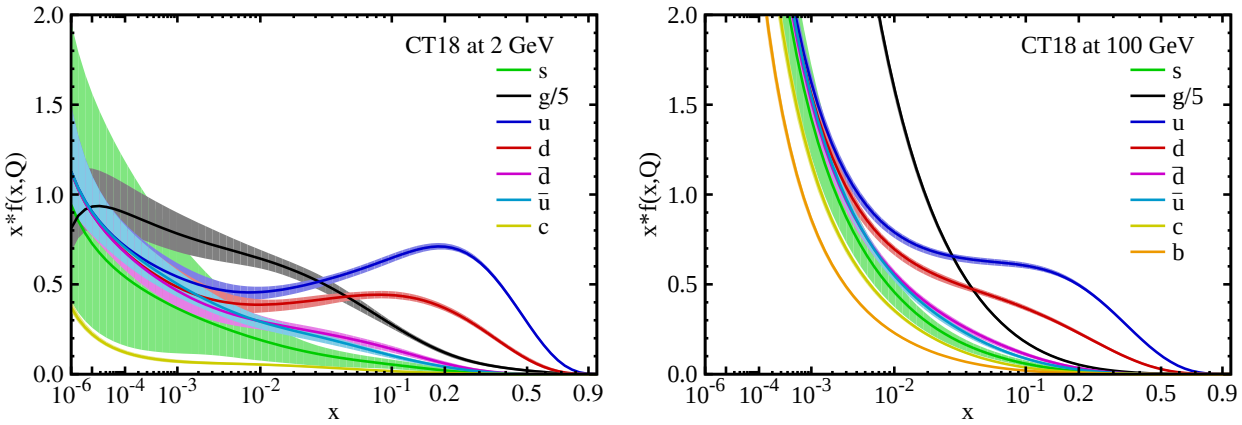

Figure 1 The CT18 unpolarized nucleon PDFs for $u, \overline{u}, d, \overline{d}, s = \overline{s}$, and g at $Q = 2$ GeV and $Q = 100$ GeV. The gluon PDF $g(x, Q)$ has been scaled down as $g(x, Q)/5$. This figure is taken from reference [2].

With the increasing high-precision measurements from LHC, RHIC, Tevatron, Jefferson Lab and HERA, quark distributions are now well-determined with only few-percent level in

many cases. However, gluon PDFs still have relatively large uncertainties because of the limited experiments in constraining them. In the unpolarized gluon PDF case, it is now constrained by the inclusion of processes such as inclusive jet production [34], top-quark pair distributions [35, 36], and direct photon production [37], inclusive deep-inelastic scattering (DIS) [38], D-meson production [39, 40], and the transverse momentum of Z bosons [41]. Although there is experimental data, e.g. top-quark pair production, which constrains $g(x)$ in the large-x region, and charm production, which constrains $g(x)$ in the small-x region. $g(x)$ is still experimentally the least known unpolarized PDF because the gluon does not couple to electromagnetic probes. The future U.S.-based Electron-Ion Collider (EIC) [42], planned to be built at Brookhaven National Lab, will further our knowledge of gluon distribution [43, 44]. The Electron-Ion Collider in China (EicC) [45], is also aim at contributing to the gluon distributions.

Currently, the global analysis of experimental measurements is the main approach to determine the PDFs. There are different collaborations have released their analyses of nucleon PDFs, including the unpolarized nucleon gluon PDF which of interest in this paper. The most recent global analyses PDF sets are CT18 PDF [2], NNPDF [46], and the MMHT14, ABMP, CJ, JAM, HERAPDF sets [47, 14, 16, 48, 49]. We show the PDF set from CT18 in Fig. 1. Different flavor quark and gluon unpolarized PDFs at $Q = 2$ GeV or $Q = 100$ GeV are shown in same plot. Since the gluon PDF $g(x, Q)$ has been scaled down as $g(x, Q)/5$ to fit with other quark PDFs in Fig. 1, it is easy to see that the gluon PDFs are dominated at small-x region, especially with larger energy scale.

I.2. pion gluon PDFs

Global analyses of pion PDFs mostly rely on Drell-Yan data. The early studies of pion PDFs were based mostly on pion-induced Drell-Yan data in conjunction with J/ψ-production data or direct photon production data to constrain the pion gluon PDF [50, 51, 52, 5, 53]. There are more recent studies, such as the work by Bourrely and Soffer [54], that extract the pion PDF based on Drell-Yan $\pi^+ W$ data. JAM Collaboration [4, 24] uses a Monte-Carlo approach to analyze the Drell-Yan πA and leading-neutron electroproduction data from HERA to reach the lower-x region, and revealed that gluons carry a significantly higher momentum fraction (about

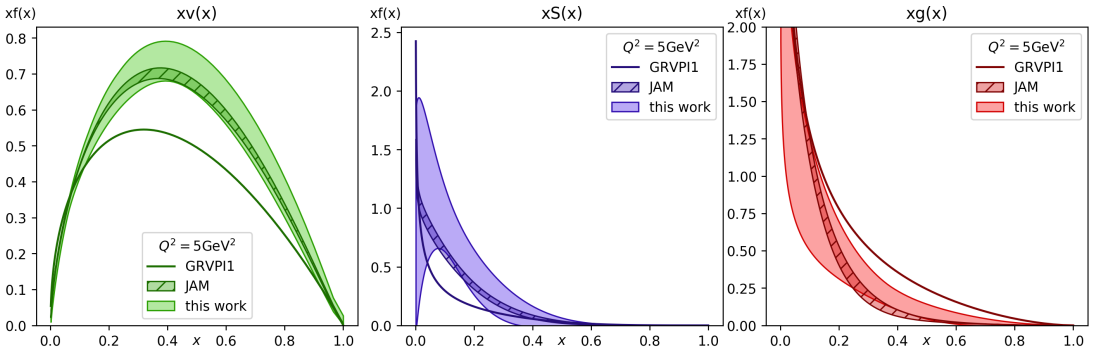

Figure 2 Comparison between the pion PDFs from the determination by xFitter collaboration [3], the JAM collaboration [4], and the GRVPI1 group [5]. This figure is taken from Fig. 3 in Ref. [3].

30%) in the pion than had been inferred from Drell-Yan data alone. The xFitter group [3] analyzed Drell-Yan πA and photoproduction data using their open-source QCD fit framework for PDF extraction and found that these data can constrain the valence distribution well but are not sensitive enough for the sea and gluon distributions to be precisely determined. The analysis done Ref. [55] suggests that the pion-induced J/ψ-production data provides an additional constraint on pion PDFs, particularly in the pion gluon PDF in the large-x region.

The pion valence- and sea-quark, gluon PDFs from xFitter collaboration [3], the JAM collaboration [4], and the `GRVPI1` group [5] are compared in Fig. 2. Similar to the nucleon PDFs case, pion gluon PDFs are dominated at small-x region. The valence-quark PDFs have the smallest relative errors among all the three plots, which indicates that they are better determined. Ultimately, the pion valence-quark distributions are better constrained than the gluon distribution from the global analysis of experimental data.

II. Lattice QCD

II.1. The continuum QCD

Lattice gauge theory is the main numerical tool to study the nonperturbative properties of QCD suggested by K. G. Wilson [56], which is a non-perturbative implementation of field theory using the Feynman path integral approach by introducing a finite lattice spacing and finite lattice size. Space-time is discretized and the path integral becomes finite due to the finite size. This discretization introduces deviations from continuum QCD calculations. Such deviations vanish when the lattice spacing is taken to zero, which is referred as the continuum limit. We introduce QCD starting with its Lagrangian in the continuum Minkowski space-time,

$$\mathcal{L}_{QCD} = \sum_f \bar{\psi}_f^\alpha(x)(\not{D}_{\alpha\beta} - m_f\delta_{\alpha\beta})\psi_f^\beta(x) - \frac{1}{4}\sum_a F_a^{\mu\nu}(x)F_{\mu\nu}^a(x) \tag{II.1}$$

where Greek letters α, β, μ, and ν are spinor indices, a is the color index, $N_c = 3$ is the number of colors for QCD and m_f is the quark mass with flavor f. The first and second terms in the right hand side are the fermion and gluon Lagrangians, respectively. The covariant derivative $\not{D}$ and the field strength tensor $F_{\mu\nu}$ are,

$$\not{D} = i(\partial_\mu - ig\frac{\lambda^a}{2}A_\mu^a)\gamma^\mu \tag{II.2}$$

$$F_{\mu\nu}^a = \partial_\mu A_\nu^a - \partial_\nu A_\mu^a + gf^{abc}A_\mu^b A_\nu^c \tag{II.3}$$

where A_μ^a and ψ_f^α are the gauge and quark fields, g is the bare coupling constant, λ^a are the generators of $SU(N_c)$, and f_{abc} are the corresponding structure constants.

The Euclidean Lagrangian $\mathcal{L}_E$ QCD is transformed from Eq. II.1 by substituting $t \to i\tau$,

$$\begin{aligned}\mathcal{L}_{QCD}^E =& \mathcal{L}_{gluon}^E + \mathcal{L}_{fermion}^E \\ =& \frac{1}{4}\sum_a F_a^{\mu\nu}(x)F_{\mu\nu}^a(x) + \sum_f \bar{\psi}_f^\alpha(x)(\not{D}_{\alpha\beta}^E + m_f\delta_{\alpha\beta})\psi_f^\beta(x)\end{aligned} \tag{II.4}$$

where the Euclidean covariant $\not{D}^E$ is,

$$\not{D}^E = \gamma_\mu^E D_\mu^E = (\partial_\mu + ig\frac{\lambda_a}{2}A_\mu^a)\gamma_\mu^E \tag{II.5}$$

where the γ_μ^E and λ_a are the Euclidean Dirac matrices and $SU(Nc)$ generators.

The partition function in Euclidean space-time is,

$$Z = \int \mathcal{D}A_\mu \, \mathcal{D}\psi \, \mathcal{D}\bar{\psi} \, e^{-\mathcal{S}^E} \tag{II.6}$$

where the Euclidean QCD action S^E is,

$$\mathcal{S}^E = \int d^4x \mathcal{L}^E_{QCD} \tag{II.7}$$

The thermal expectation value of physical observables can be obtained by,

$$\langle \mathcal{O} \rangle = \frac{\int \Pi_\mu \mathcal{D}A_\mu \Pi_{f=1}^{N_f} \mathcal{D}\psi_f \mathcal{D}\bar{\psi}_f \mathcal{O} \exp(-\mathcal{S}^E)}{\int \Pi_\mu \mathcal{D}A_\mu \Pi_{f=1}^{N_f} \mathcal{D}\psi_f \mathcal{D}\bar{\psi}_f \exp(-\mathcal{S}^E)} \tag{II.8}$$

In practice there are two approaches to evaluating the physical observables in QCD. One approach is to use perturbative methods to do the calculation when the strong coupling constant α_s is small in high energy or short distance interactions. Another approach is lattice gauge theory which regularizes on a four-dimensional discretized Euclidean space-time. The infrared and ultraviolet momentum cut-offs are introduced by the finite lattice size $L^3 \times T$ and lattice spacing a, which are π/L and π/a respectively. Equation II.8 can be computed via high performance computer because it becomes multiple integrations. A consequence of lattice gauge theory is that the Lorentz symmetry is lost. Since all the symmetries are restored in the continuum limit, to recover the real physics, we remove the discretization by taking the continuum limit $a \to 0$, $L \to \infty$ and $T \to \infty$.

In the following sections we will briefly review the discretized version of the fields, the correlation functions, and the nonperturbative renormalization on the lattice.

II.2. The formulation of Lattice QCD

On the lattice, the gluon fields are defined as the links between lattice sites and the fermion fields are defined on the lattice sites. We will discuss them in detail in Sec. II.2.1 and Sec. II.2.2.

II.2.1. Gauge actions

The original gauge action was introduced by Wilson in Ref. [56, 57]. The Wilson gauge action can be formed by the summation of the trace of the smallest closed loops on all lattice sites,

$$S_G[U] = \beta \sum_x \sum_{\mu<\nu} \text{tr}(1 - \frac{1}{N_c}\text{Re}\mathcal{P}_{\mu\nu}) \tag{II.9}$$

where the inverse the coupling $\beta = 2N_c/g^2$, g is the bare gauge coupling on the lattice, $\mathcal{P}$ is the plaquette representing the smallest closed loop,

$$\mathcal{P}_{\mu,\nu} = U_\mu(x)U_\nu(x + a\hat{\mu})U^\dagger_\mu(x + a\hat{\nu})U^\dagger_\nu(x). \tag{II.10}$$

The wilson link $U_\mu(x)$ is related to the continuum gauge fields $A_\mu(x)$ through,

$$U_\mu(x) = e^{iagA_\mu(x+\mu/2)}. \tag{II.11}$$

Based on the above Wilson gauge action construction, the leading correction is $O(a^2)$ in the continuum limit by taking $a \to 0$. There are many different improved actions which have less discretization errors.

To improve the gauge action, we write down an effective action which describes the behavior of Wilson's form of lattice QCD at finite a. Following [1, 2, 5–7] we write the effective action in the form,

$$S^{eff}_G = \int d^4x(L^0(x) + aL^1(x) + a^2L^2(x) + ...), \tag{II.12}$$

where L^0 is the usual QCD Lagrangian, the terms L^k, $k > 0$ are the additional correction terms which are built from products of quark and gluon fields with dimensions $d = 4 + k$. The leading correction term L^1 can be written as a linear combination of the following dimension-5 operators,

$$\begin{aligned}
L^1_1(x) =& \bar{\psi}(x)\sigma_{\mu\nu}F_{\mu\nu}(x)\psi(x),\\
L^1_2(x) =& \bar{\psi}(x)\overrightarrow{D}_\mu(x)\overrightarrow{D}_\mu(x)\psi(x) + \bar{\psi}(x)\overleftarrow{D}_\mu(x)\overleftarrow{D}_\mu(x)\psi(x),\\
L^1_3(x) =& m\text{tr}[F_{\mu\nu}(x)F_{\mu\nu}(x)],\\
L^1_4(x) =& m(\bar{\psi}(x)\gamma_\mu\overrightarrow{D}_\mu(x)\psi(x) - \bar{\psi}(x)\gamma_\mu\overleftarrow{D}_\mu(x)\psi(x)),
\end{aligned}$$

$$L_5^1(x) = m^2\bar{\psi}(x)\psi(x). \tag{II.13}$$

This list of operators may be further reduced by using the field equation $(\gamma_\mu D_\mu + m)\psi = 0$, which gives rise to the two relations

$$\begin{aligned} L_1^1 - L_2^1 + 2L_5^1 &= 0, \\ L_4^1 + L_5^1 &= 0. \end{aligned} \tag{II.14}$$

These relations may be used to eliminate the terms L_2^1 and L_4^1 from the set of operators. Thus it is sufficient to work with only the terms L_1^1, L_3^1 and L_5^1. For $O(a)$ improvement it is sufficient to add a single term including the L^1 terms to the fermion action. Relevant purely gluonic operators appear only at dimension 6, i.e., they contribute at $O(a^2)$. For the improvement of the gauge action we refer the reader to the original literature, where the Luscher–Weisz gauge action is presented [58, 59, 60]. The general form of the $O(a)$ improvement of the gauge action,

$$S_G = \int d^4x (L^0(x) + c_2 L_2^1(x) + c_3 L_3^1(x) + c_5 L_5^1(x)), \tag{II.15}$$

One-loop Symanzik improved gauge action is introduced by K. Symanzik in the book [61], where the corresponding coefficients are $c_2 = -1/12, c_3 = 0, c_5 = 1/2$. The "Iwasaki gauge action" introduced by Y.Iwasaki in 1983 [62] has the coefficient $c_2 = -0.331$. Such gauge actions are adopted by lattice collaborations to generate lattice ensembles. The MILC collaboration [63, 64] and the RBC collaboration [65] utilize the Symanzik improved gauge action and Iwasaki gauge action respectively.

II.2.2. Fermion action

To discretize the Dirac action, Wilson replaced the derivative with the symmetrized difference and included appropriate gauge links to maintain gauge invariance

$$\bar{\psi}D\psi = \frac{1}{2a}\bar{\psi}(x)\sum_\mu \gamma_\mu [U_\mu(x)\psi(x+\hat{\mu}) - [U_\mu^\dagger(x-\hat{\mu})\psi(x-\hat{\mu})] \tag{II.16}$$

It is easy to see that one recovers the Dirac action in the limit $a \to 0$ by Taylor expanding the U_μ and $\psi(x+\hat{\mu})$ in powers of the lattice spacing a, keeping only the leading term in a,

$$\frac{1}{2a}\bar{\psi}(x)\gamma_\mu[(1 + iagA_\mu(x + \frac{\hat{\mu}}{2}) + ...)(\psi(x) + a\psi^{'}(x) + ...)$$

$$
\begin{aligned}
&- (1 - iagA_\mu(x - \frac{\hat{\mu}}{2}) + ...)(\psi(x) - a\psi^{'}(x) + ...)] \\
=&\bar{\psi}(x)\gamma_\mu(\partial_\mu + \frac{a^2}{6}\partial_\mu^3 + ...)\psi(x) \\
&+ ig\bar{\psi}(x)\gamma_\mu[A_\mu + \frac{a^2}{2}(\frac{1}{4}\partial_\mu^2 A_\mu + (\partial_\mu A_\mu)\partial_\mu + A_\mu\partial_\mu^2) + ...]\psi(x),
\end{aligned}
\tag{II.17}
$$

which is the kinetic part of the continuum Dirac action to $O(a^2)$ in Euclidean space-time. Thus one arrives at the simplest, so called "naive" lattice action for fermions,

$$
\begin{aligned}
\mathcal{S}^N &= m_q \sum_x \bar{\psi}(x)\psi(x) \\
&+ \frac{1}{2a}\sum_x \bar{\psi}(x)\gamma_\mu[U_\mu(x)\psi(x+\hat{\mu}) - U_\mu^\dagger(x-\hat{\mu})\psi(x-\hat{\mu})] \\
&= \sum_x \bar{\psi}(x) M_{xy}^N[U]\psi(x)
\end{aligned}
\tag{II.18}
$$

where the interaction matrix M^N is

$$
M_{i,j}^N[U] = m_q\delta_{ij} + \frac{1}{2a}\sum_\mu[\gamma_\mu U_{i,\mu}\delta_{i,j-\mu} - \gamma_\mu U_{i-\mu,\mu}^\dagger\delta_{i,j+\mu}] \tag{II.19}
$$

The Euclidean γ matrices are hermitian, $\gamma_\mu = \gamma_\mu^\dagger$, and satisfy $\gamma_\mu, \gamma_\nu = 2\delta_{\mu\nu}$.

The naive-quark action has an exact "doubling" symmetry under the transformation:

$$
\begin{aligned}
\psi(x) \quad \rightarrow \quad \tilde{\psi}(x) \equiv& \gamma_5\gamma_\rho(-1)^{x_\rho/a}\psi(x) \\
=& \gamma_5\gamma_\rho \exp(ix_\rho\pi/a)\psi(x).
\end{aligned}
\tag{II.20}
$$

Thus any low energy-momentum mode $\psi(x)$ of the theory is equivalent to another mode $\tilde{\psi}(x)$ that has momentum $p_\rho \approx \pi/a$, the maximum value allowed on the lattice. This new mode is one of the "doublers" of the naive quark action. The doubling transformation can be applied successively in two or more directions. There are 15 doublers because of the four dimensions.

It is not possible to construct a lattice fermion action that is ultra local, has chiral symmetric and the correct continuum limit, and undoubled at the same time. There are several improved fermions that solve the doubling problem. The Wilson fermion [56] solves the doubling problem but breaks chiral symmetry. Staggered fermion also solves the doubling problem but brakes taste symmetry. Ginsparg-Wilson fermion extends chiral symmetry. This fermion action is local but not ultra local, which means it is still universal as the Wilson fermion.

II.2.2.1 Staggered Fermion

The staggered-quark discretization of the quark action is equivalent to the naive discretization of the quark action. Staggering is an important optimization in simulations. Consider the following local transformation of the naive-quark field:

$$\psi(x) \to \Omega(x)\,\chi(x) \qquad \bar{\psi}(x) \to \bar{\chi}(x)\,\Omega^\dagger(x) \tag{II.21}$$

where

$$\Omega(x) \equiv \gamma_x \equiv \prod_{\mu=0}^{3} (\gamma_\mu)^{x_\mu}, \tag{II.22}$$

and we have set the lattice spacing $a = 1$ for convenience. (We will use lattice units, where $a = 1$, in this and all succeeding appendices.) Note that

$$\Omega(x) = \gamma_n \qquad \text{for } n_\mu = x_\mu \mod 2; \tag{II.23}$$

there are only 16 different Ωs. It is easy to show that

$$\alpha_\mu(x) \equiv \Omega^\dagger(x)\gamma_\mu\Omega(x \pm \hat{\mu}) \;=\; (-1)^{x_\mu^<}, \tag{II.24}$$

$$1 = \Omega^\dagger(x)\Omega(x) \tag{II.25}$$

where $x_\mu^< \equiv x_0 + x_1 + \cdots + x_{\mu-1}$. Therefore, the staggered-quark action can be formulated by rewriting the naive-quark action as

$$\bar{\psi}(x)(\gamma \cdot \Delta + m)\psi(x) \;=\; \bar{\chi}(x)(\alpha(x) \cdot \Delta + m)\chi(x). \tag{II.26}$$

Remarkably the χ action is diagonal in spinor space; each component of χ is exactly equivalent to every other component. Consequently the χ propagator is diagonal in spinor space in *any background gauge field*:

$$\langle \chi(x)\bar{\chi}(y)\rangle_\chi \;=\; s(x,y)\,\mathbf{1}_{\text{spinor}}, \tag{II.27}$$

where $s(x,y)$ is the one-spinor-component staggered-quark propagator. Transforming back to the original naive-quark field we find that

$$S_F \;\equiv\; \langle \psi(x)\bar{\psi}(y)\rangle_\psi \;=\; s(x,y)\,\Omega(x)\Omega^\dagger(y). \tag{II.28}$$

This last result is a somewhat surprising consequence of the doubling symmetry, it illustrates that the spinor structure of the naive-quark propagator is completely independent of the gauge field. This is certainly not the case for individual tastes of naive quark, whose spins will flip back and forth as they scatter off fluctuations in the chromomagnetic field. The sixteen tastes of the naive quark field are packaged in such a way that all gauge-field dependence vanishes in the spinor structure.

We can introduce such a form factor by replacing the link operator $U_\mu(x)$ in the action with $F_\mu U_\mu(x)$, where smearing operator F_μ is defined by

$$\mathcal{F}_\mu \equiv \prod_{\rho\neq\mu} \left(1 + \frac{a^2\delta_\rho^{(2)}}{4}\right)\Bigg|_{\text{symm.}}, \tag{II.29}$$

and $\delta_\rho^{(2)}$ approximates a covariant second derivative when acting on link fields as

$$\begin{aligned}\delta_\rho^{(2)} U_\mu(x) \equiv \frac{1}{a^2} \big(&U_\rho(x)\, U_\mu(x+a\hat{\rho})\, U_\rho^\dagger(x+a\hat{\mu}) \\ &- 2U_\mu(x) \\ &+ U_\rho^\dagger(x-a\hat{\rho})\, U_\mu(x-a\hat{\rho})\, U_\rho(x-a\hat{\rho}+a\hat{\mu})\big)\,.\end{aligned} \tag{II.30}$$

Equation II.29 holds given that $\delta_\rho^{(2)} \approx -4/a^2$ (and $\mathcal{F}_\mu$ vanishes) when acting on a link field that carries momentum $q_\rho \approx \pi/a$ [66].

Smearing the links with $\mathcal{F}_\mu$ removes the leading $O(a^2)$ taste-exchange interactions, but introduces new $O(a^2)$ errors. These can be removed by replacing $\mathcal{F}_\mu$ with [67]

$$\mathcal{F}_\mu \equiv \mathcal{F}_\mu - \sum_{\rho\neq\mu} \frac{a^2(\delta_\rho)^2}{4}, \tag{II.31}$$

where δ_ρ approximates a covariant first derivative:

$$\begin{aligned}\delta_\rho\, U_\mu(x) \equiv \frac{1}{a} \big(&U_\rho(x)\, U_\mu(x+a\hat{\rho})\, U_\rho^\dagger(x+a\hat{\mu}) \\ &- U_\rho^\dagger(x-a\hat{\rho})\, U_\mu(x-a\hat{\rho})\, U_\rho(x-a\hat{\rho}+a\hat{\mu})\big)\,.\end{aligned} \tag{II.32}$$

The new term has no effect on taste exchange but cancels the $O(a^2)$ part of $\mathcal{F}_\mu$. Improving the derivative by $\Delta_\mu \to \Delta_\mu - \frac{a^2}{6}\Delta_\mu^3$, and replacing links by a^2-accurate smeared links removes all tree-level $O(a^2)$ errors in the naive-quark action. The result is the widely used "ASQTAD"

action [67],

$$\sum_x \bar{\psi}(x) \left(\sum_\mu \gamma_\mu \left(\Delta_\mu(V) - \frac{a^2}{6} \Delta_\mu^3(U) \right) + m_0 \right) \psi(x), \tag{II.33}$$

where in the first difference operator,

$$V_\mu(x) \equiv \mathcal{F}_\mu^A \, U_\mu(x). \tag{II.34}$$

In practice, the operator V_μ is usually "tadpole" improved [68]; however, in reality, tadpole improvement is not needed when links are smeared and re-unitarized [69, 70].

The doubly smeared operator is simplified if we rearrange it as follows

$$\mathcal{F}_\mu^H \equiv \left(\mathcal{F}_\mu - \sum_{\rho \neq \mu} \frac{a^2 (\delta_\rho)^2}{2} \right) \mathcal{U} \, \mathcal{F}_\mu, \tag{II.35}$$

where the entire correction for a^2 errors is moved to the outermost smearing. The highly improved stag- gered quark (HISQ) discretization of the quark action is

$$\sum_x \bar{\psi}(x) \, \left(\gamma \cdot \mathcal{D}^{\mathrm{HISQ}} + m \right) \, \psi(x), \tag{II.36}$$

where

$$\mathcal{D}_\mu^{\mathrm{HISQ}} \equiv \Delta_\mu(W) - \frac{a^2}{6}(1+\epsilon) \Delta_\mu^3(X), \tag{II.37}$$

where the difference operators are,

$$W_\mu(x) \equiv F_\mu^H \, U_\mu(x), \tag{II.38}$$

and,

$$X_\mu(x) \equiv \mathcal{U} \, F_\mu^H \, U_\mu(x). \tag{II.39}$$

The approaches to computing radiative correction to ϵ are discussed in Ref. [71]. One approach is to adjust ϵ until the relativistic dispersion relation fulfilled nonperturbatively. Another approach is to compute the one-loop correction to ϵ using perturbation theory, by requiring the correct dispersion relation for a quark in 1-loop order.

Staggered fermions are widely used for dynamical simulations due to the reduced number of degrees of freedom. This property ensures staggered fermions to be numerically cheaper

to simulate while preserving chiral symmetry. However, a problem is that the action describes four degenerate tastes of quarks, while in a realistic QCD simulation one would like to have two light mass-degenerate u and d quarks and one heavier strange quark. Although the conceptual problems are not all resolved, simulations with staggered fermions have found good agreement with experimental results, as shown in Refs. [72, 73, 74].

II.2.2.2 Wilson-like Fermions

Wilson's solution to the doubling problem was to add a dimension five operator $ar\bar{\psi}\Box\psi$, whereby the extra fifteen species at $p_\mu = \pi$ get a mass proportional to r/a [56]. The Wilson action is

$$\begin{aligned}\mathcal{S}^W &= m_q \sum_x \bar{\psi}(x)\psi(x) \\ &+ \frac{1}{2a}\sum_x \bar{\psi}(x)\gamma_\mu[U_\mu(x)\psi(x+\hat{\mu}) - U^\dagger_\mu(x-\hat{\mu})\psi(x-\hat{\mu})] \\ &- \frac{r}{2a}\sum_x \bar{\psi}(x)[U_\mu(x)\psi(x+\hat{\mu}) - 2\psi(x) + U^\dagger_\mu(x-\hat{\mu})\psi(x-\hat{\mu})] \\ &= \sum_x \bar{\psi}^L(x) M^W_{xy}[U]\psi^L(x), \end{aligned} \tag{II.40}$$

where the interaction matrix M^W is

$$M^W_{i,j}[U] = \delta_{ij} + \kappa\sum_\mu[(r-\gamma_\mu)U_{i,\mu}\delta_{i,j-\mu} + (r+\gamma_\mu)U^\dagger_{i-\mu,\mu}\delta_{i,j+\mu}], \tag{II.41}$$

with the rescalling

$$\kappa = \frac{1}{2m_q a + 8r}\psi^L = \sqrt{m_q a + 4r}\psi = \frac{\psi}{\sqrt{2\kappa}}. \tag{II.42}$$

Even though the Wilson fermion fixes the doublers, it introduces $O(a)$ artifacts. To remove these artifacts, the clover-improvement is introduced by adding an additional dimension-5 operator to the Wilson action $\mathcal{S}^W$. The resulting clover action is,

$$\begin{aligned}\mathcal{S}^{clover} =& \mathcal{S}^W - \frac{iac_{sw}\kappa r}{4}\bar{\psi}(x)\sigma_{\mu\nu}F_{\mu\nu}\psi(x) \\ =& m_q\sum_x \bar{\psi}(x)\psi(x) \\ &+ \frac{1}{2a}\sum_x \bar{\psi}(x)\gamma_\mu[U_\mu(x)\psi(x+\hat{\mu}) - U^\dagger_\mu(x-\hat{\mu})\psi(x-\hat{\mu})]\end{aligned}$$

$$
\begin{aligned}
&-\frac{r}{2a}\sum_x \bar{\psi}(x)[U_\mu(x)\psi(x+\hat{\mu})-2\psi(x)+U_\mu^\dagger(x-\hat{\mu})\psi(x-\hat{\mu})]\\
&-\frac{iac_{sw}\kappa r}{4}\bar{\psi}(x)\sigma_{\mu\nu}F_{\mu\nu}\psi(x)\\
&=\sum_x \bar{\psi}^L(x)M^C_{xy}[U]\psi^L(x),
\end{aligned}
\tag{II.43}
$$

the fermion matrix M^C is given by [59]

$$
\begin{aligned}
M[U]^C_{i,j} =& \left(1-\frac{i}{2}\,c_{sw}\,\kappa\,\sigma_{\mu\nu}\,\mathcal{F}_{\mu\nu}(x)\right)\delta_{i,j}\\
&-\kappa\sum_\mu\left\{(1-\gamma_\mu)\,U_\mu(x)\,\delta_{i+\hat{\mu},j}+(1+\gamma_\mu)\,U_\mu^\dagger(x-\hat{\mu})\,\delta_{i-\hat{\mu},j}\right\}\quad ,
\end{aligned}
\tag{II.44}
$$

where we sum over μ and ν. The anti-symmetric and anti-Hermitian tensor $\mathcal{F}^C$ is given by

$$
\begin{aligned}
\mathcal{F}^C_{\mu,\nu} =& \frac{1}{8}\left[U_\mu(x)U_\nu(x+\hat{\mu})U_\mu^\dagger(x+\hat{\nu})U_\nu^\dagger(x)\right.\\
&+U_\nu(x)U_\mu^\dagger(x+\hat{\nu}-\hat{\mu})U_\nu^\dagger(x-\hat{\mu})U_\mu(x-\hat{\mu})\\
&+U_\mu^\dagger(x-\hat{\mu})U_\nu^\dagger(x-\hat{\nu}-\hat{\mu})U_\mu(x-\hat{\nu}-\hat{\mu})U_\nu(x-\hat{\nu})\\
&+U_\nu^\dagger(x-\hat{\nu})U_\mu(x-\hat{\nu})U_\nu(x-\hat{\nu}+\hat{\mu})U_\mu^\dagger(x)\\
&\left.-\,h.c.\right]\quad .
\end{aligned}
\tag{II.45}
$$

Staggered or Wilson-like fermions have their relative advantages and disadvantages. Staggered fermions do better when the chiral symmetry plays an essential role and the external states are Goldstone bosons. Wilson fermions are preferred due to their correspondence with Dirac fermions in terms of spin and flavor.

II.2.2.3 Other fermion actions

There are other fermion actions that are also commonly used in the lattice calculations. Overlap fermions originated from the initial papers on the overlap formulation [75, 76]. Neuberger presented the modern form of the overlap Dirac operator in Ref. [77] and showed in Ref. [78] that it is a solution of the Ginsparg–Wilson equation. Domain wall fermions were outlined in the seminal paper by Kaplan [79]. The ideas developed further in Ref. [80, 81, 82] gave rise to the formulation of domain wall fermions mainly used now. An example of dynamical simulations with domain wall fermions is given in Ref. [83]. Twisted mass QCD is a formulation which in its simplest form pertains to QCD with two mass-degenerate quark flavors of Wilson fermions

(QCD with isospin). Twisted mass QCD was first outlined in Refs. [84, 85]. An example of a lattice calculation of the nucleon parton distribution function is presented in Ref. [9]. Different fermion actions are used due to different physics goals and different computation resources.

II.2.2.4 Mixed-action

As described in the previous section, Wilson fermions break chiral and flavour symmetries. However, they are computationally expensive compared to improved staggered quarks. For example, in the $N_f = 2+1$ improved staggered case, the square root of the fermion determinant is employed to reduce the number of dynamical flavours from four to two for the up and down quarks, and the fourth root is taken to reduce the number of flavours from four to one for the strange quark [72]. Ensembles of gauge field configurations are then generated with these fractional power determinants as weight factors. A mixed action is defined [86] as one where the action used to generate the ensemble of gauge configurations, or sea quark action, is different from the valence quark action used to determine hadronic observables on those configurations. Since all lattice Dirac operators give the same continuum limit, the differences between the actions are $O(a)$ and vanish at the continuum limit in the mixed-action.

One advantage of using mixed-action fermions is that one can use computationally cheaper fermion actions for sea quarks, such as staggered-like fermion actions. There are disadvantages to using mixed-action fermions. One possible problem for the Wilson-type fermions is that they have "exceptional" configurations in the simulation because they do not preserve the chiral symmetry. The use of chiral fermions like the HISQ can help with this problem due to the condition number of the fermion matrix going like a single inverse power of the quark mass. One disadvantage of the mixed-action fermion is that one cannot match the valence and sea quarks to restore unitarity at finite lattice spacing, since the valence and sea quarks have different discretization effects. For example, one can utilize clover valence fermion on MILC collaboration generated $2 + 1 + 1$- flavor HISQ ensembles at physical pion mass with multiple fine lattice spacings [87].

II.3. Correlation functions

The evaluation of lattice correlation functions is a standard procedure in most lattice calculations . We compute quark propagators for each gauge configuration, combine them to construct

the hadron propagators, and average over all gauge configurations. We need to first identify the hadron interpolators and from these we can obtain the Euclidean correlator. The two-point and three-point correlators are discussed in detail in the following subsections.

II.3.1. Smearing

Link smearing

The correlation functions signal can be improved by smoothing or smearing the gauge field over time slices or over both space and time. Such smearing can be use because we are interested in long distance correlation, and it is typical for gauge theories to have violent gauge field short distance fluctuations. Smearing is done typically by replacing the link variables with local averages over short paths connecting the endpoints of the replaced link. One does not have to fix the gauge for smearing because it is a gauge covariant procedure.

We can then obtain the operators and propagators constructed on the smeared configurations. The smearing operator combines a fixed number of links which ensures the smearing to be local. Thus, it should have a negligible effect on the operators' long distance correlation signals in the continuum limit. There are several algorithms to smear the gauge fields. Here, we will briefly introduce three of them.

APE smearing is the first proposed smearing transformation used for operator improvement [88]. APE smearing averages over the original link U_μ and the six perpendicular staples $C_{\mu\nu}$ connecting its endpoints,

$$U_\mu^{'}(x) = (1-\alpha)U_\mu(x) + \frac{\alpha}{6}\sum_{\nu\neq\mu} C_{\mu\nu}(x) \tag{II.46}$$

$$\begin{aligned} C_{\mu\nu}(x) =& U_\nu(x)U_\mu(x+\hat{\nu})U_\nu(x+\hat{\mu})^\dagger \\ &+ U_\nu(x-\hat{\nu})^\dagger U_\mu(x-\hat{\nu})U_\nu(x-\hat{\nu}+\hat{\mu}) \end{aligned} \tag{II.47}$$

where the α parameter can be adjusted depending on the gauge coupling. The APE smearing reduces scaling violations, improves chiral symmetry, and reduces taste breaking. However, APE smearing has some disadvantages, it smears out short scale physical properties if repeated too many times, its projected link is not differentiable and it cannot be used in dynamical simulations.

The HYP smearing procedure is similar to the APE smearing, it contains 3 sets of APE

smearing that stays within a hypercube [89, 90].

$$\begin{aligned}
\bar{V}_{\mu,\nu\sigma}(x) =&(1-\alpha_1)U_\mu(x) + \frac{\alpha_1}{2} \sum_{\pm\rho\neq(\mu,\nu,\sigma)} U_\rho(x)\, U_\mu(x+\hat{\rho})\, U_\rho(x+\hat{\mu})^\dagger \\
\tilde{V}_{\mu,\nu}(x) =&(1-\alpha_2)U_\mu(x) + \frac{\alpha_2}{4} \sum_{\pm\sigma\neq(\mu,\nu)} \bar{V}_{\sigma,\mu\nu}(x)\, \bar{V}_{\mu,\nu\sigma}(x+\hat{\sigma})\, \bar{V}_{\sigma,\mu\nu}(x+\hat{\mu})^\dagger \\
U_\mu^{'}(x) =&(1-\alpha_3)U_\mu(x) + \frac{\alpha_3}{6} \sum_{\pm\nu\neq(\mu)} \tilde{V}_{\nu,\mu}(x)\, \tilde{V}_{\mu,\nu}(x+\hat{\nu})\, \tilde{V}_{\nu,\mu}(x+\hat{\mu})^\dagger
\end{aligned} \tag{II.48}$$

where the α_1, α_2 and α_3 are tunable parameters in the HYP smearing procedure. The HYP smearing is more compact and effective than APE smearing, but still not differentiable.

The stout smearing method [91] uses a particular way of projection by defining the new link after a smearing step as

$$U_\mu^{'}(x) = e^{iQ_\mu(x)} U_\mu(x), \tag{II.49}$$

$Q_\mu(x)$ is a traceless hermitian matrix constructed from staples,

$$\begin{aligned}
Q_\mu(x) =&\frac{i}{2}(\Omega_\mu(x)^\dagger - \Omega_\mu(x) - \frac{1}{3}\mathrm{tr}[\Omega_\mu(x)^\dagger - \Omega_\mu(x)]), \\
\Omega_\mu(x) =&(\sum_{\nu\neq\mu} \rho_{\mu\nu} C_{\mu\nu}(x)) U_\mu(x)^\dagger
\end{aligned} \tag{II.50}$$

where the staples $C_{\mu\nu}$ are given in Eq. II.47 and the factors $\rho_{\mu\nu}$ are tunable parameters. The new links have gauge transformation properties like the original ones. The advantage of stout smearing is that $U_\mu^{'}(n)$ is differentiable with respect to the link variables, which is beneficial in the applications like the hybrid Monte Carlo method for dynamical fermions.

Smeared action simulations are usually faster than unsmeared ones. One can even have multiple iterations of all these smearing steps. There are longer distance links getting involved with larger iteration steps, and the asymptotic behavior of the operators and propagators will be affected more with larger iteration steps. Therefore, one should carefully examine them to avoid the potential problems.

Quark smearing

Quark smearing within hadronic sources or sinks is used to increase the overlap with the desired physical state. The gauge link smearing was generalized by allowing iterative smearing of quark fields in interpolators that create hadronic states, in particular gauge covariant Wuppertal

smearing [92, 93, 94], hydrogen-like smearing [94], Jacobi smearing [95, 96], APE smearing was employed for the spatial gauge transporters within the quark smearing in Refs. [93, 94], Gaussian smearing [97, 98], "free form smearing" [99], Gauge fixed sources have been utilized in parallel to gauge covariant iterative smearing functions, wall sources for zero [100], non-zero momentum [101], box [102] sources, Gaussian "shell sources" [103], and sources with nodes [104]. Newer attempts have been made to introduce an anisotropy into Wuppertal smearing [105, 106].

In this thesis, Gaussian momentum smearing is used for the quark field which introduced in, Ref. [107],

$$S_{\text{mom}}\Psi(x) = \frac{1}{1+6\alpha}\big(\Psi(x) + \alpha\sum_j U_j(x)e^{ik\hat{e}_j}\Psi(x+\hat{e}_j)\big), \tag{II.51}$$

where k is the momentum-smearing parameter and α is the Gaussian smearing parameter. Gaussian momentum smearing is helpful to getting us a better signal at a higher boost nucleon momentum for the correlators.

II.3.2. propagator and inversion

The quark propagator governs the behavior of n-point functions and is important to analyze it. For free fermions this analysis is best done with the momentum space propagator $\tilde{D}(p)^{-1}$. For the case of massless fermions $m = 0$, the fixed p propagator has the correct naive continuum limit as $a \to 0$,

$$\tilde{D}(p)^{-1}|_{m=0} = \frac{-ia^{-1}\sum_\mu \gamma_\mu sin(p_\mu a)}{a^{-2}\sum_\mu sin(p_\mu a)^2} \overset{a\to 0}{\to} \frac{-i\sum_\mu \gamma_\mu p_\mu}{p^2} \tag{II.52}$$

The general quark propagator

$$G^{ij}_{\alpha\beta}(x,y) = \langle q^i_\alpha(x)\bar{q}^j_\beta(y)\rangle \tag{II.53}$$

satisfies

$$M^{ik}_{\alpha\gamma}(x,z)G^{kj}_{\gamma\beta}(z,y) = \delta_{ij}\delta_{\alpha\beta}\delta_{xy}, \tag{II.54}$$

where M is the lattice Dirac operator. The anti-quark propagator is related through

$$G(y,x) = \gamma_5 G(x,y)^\dagger \gamma_5, \tag{II.55}$$

which is an evident property from the lattice Dirac equation.

The sources to all propagators can be obtained by finding the solutions x_i to the Matrix equation,

$$Ax_i = b_i \tag{II.56}$$

where A is the Dirac matrix, b_i are the constructed our quark sources. The system of linear equations can be solved by iterative methods such as Conjugate Gradient (CG) [108] for symmetric positive definite matrices, the MINRES-method [109] for symmetric non-definite matrices or some sort of Bi-ConjugateGradient (BiCG) method [110] for non-symmetric matrices. We use multigrid-ConjugateGradient (MG-CG) algorithm [111, 112] in the Chroma software package [1]. The procedure of MG-CG is as following. To solve

$$Ax = b \tag{II.57}$$

and

$$(A + \sigma)x^\sigma = b \tag{II.58}$$

using the method of CG. The $(i+1)^{\text{th}}$ iterate x_{i+1} to the solution can be obtained from x_i,

$$x_{i+1} = x_i + \alpha_i p_i \tag{II.59}$$

where $x_1 = 0$ is the starting point, and p_i are the search directions which obey the recursion relation,

$$p_1 = g_1; \quad p_{i+1} = g_{i+1} + \beta_i p_i \quad \forall i \geq 1 \tag{II.60}$$

where g_i is the residue equal to $Ax_i - b$ and also obeys a recursion relation,

$$g_1 = -b; \quad g_{i+1} = g_i + \alpha_i A p_i \quad \forall i \geq 1 \tag{II.61}$$

Then, the coefficients α_i and β_i in Eqs. II.60 and II.61 are obtained as,

$$\alpha_i = -\frac{(g_i, g_i)}{(p_i, Ap_i)} \tag{II.62}$$

$$\beta_i = \frac{(g_{i+1}, g_{i+1})}{(g_i, g_i)} \tag{II.63}$$

Using the Lanczos connection, we write down the recursion relation for x_i^σ and p_i^σ with that

the normalized Lanczos vectors for A and $A+\sigma$ are the same,

$$g_i^\sigma = c_i^\sigma g_i \tag{II.64}$$

Then assuming that $x_1^\sigma = 0$, we have $c_1^\sigma = 1$. Because g_i^σ obeys the following recursion relation:

$$g_{i+1}^\sigma = \Big[1 + \frac{\alpha_i^\sigma \beta_{i-1}^\sigma}{\alpha_{i-1}^\sigma}\Big] g_i^\sigma + \alpha_i^\sigma (A+\sigma) g_i^\sigma - \frac{\alpha_i^\sigma \beta_{i-1}^\sigma}{\alpha_{i-1}^\sigma} g_{i-1}^\sigma. \tag{II.65}$$

Then we substitute Eq. II.64 into Eq. II.65,

$$\alpha_i^\sigma = \alpha_i \frac{c_{i+1}^\sigma}{c_i^\sigma} \tag{II.66}$$

$$\beta_i^\sigma = \beta_i [\frac{c_{i+1}^\sigma}{c_i^\sigma}]^2 \tag{II.67}$$

$$\frac{c_i^\sigma}{c_{i+1}^\sigma} = 1 - \alpha_i \sigma + \alpha_i \frac{\beta_{i-1}}{\alpha_{i-1}} \big[1 - \frac{c_i^\sigma}{c_{i-1}^\sigma}\big] \tag{II.68}$$

Note that $c_1^\sigma = 1$ and

$$c_2^\sigma = \frac{1}{1-\alpha_1 \sigma}. \tag{II.69}$$

The recursion relations for p_i^σ and x_i^σ are

$$p_1^\sigma = g_1; \quad p_{i+1}^\sigma = c_{i+1}^\sigma g_{i+1} + \beta_i^\sigma p_i^\sigma \quad \forall i \geq 1, \tag{II.70}$$

$$x_{i+1}^\sigma = x_i^\sigma + \alpha_i^\sigma p_i^\sigma. \tag{II.71}$$

The advantage of this method is that g_i^σ is trivially modified and the Eq. II.61 that involves the multiplication of matrix with a vector remains the same independent of σ.

MG-CG Algorithm [113]

Starting with $g_1 = -b$, $p_1 = -b$, $c_1^\sigma = 1$, $p_1^\sigma = -b$ and $x_1^\sigma = 0$. The iteration proceeds as follows:

i. Compute Ap_i and (p_i, Ap_i).

ii. Compute (g_i, g_i) and save this number, and compute α_i.

iii. Use Eq. II.61 to compute g_{i+1} then overwrite g_i.

iv. Compute (g_{i+1}, g_{i+1}) and β_i using the g_{i+1} in step iii.

v. Compute p_{i+1} using Eq. II.60 and overwrite p_i.

vi. Compute c_{i+1}^{σ} using Eq. II.69 in the first iteration and using Eq. II.62 from the second iteration onwards.

vii. Compute α_i^{σ} and β_i^{σ} using Eq. II.66 and Eq. II.67 respectively.

viii. Compute x_{i+1}^{σ} using Eq. II.71 and overwrite x_i^{σ}.

ix. Compute p_{i+1}^{σ} using Eq. II.70 and overwrite p_i^{σ}.

Once the solutions to the propagator equation are computed, we can obtain the correlation functions. We will expand the discussion of the correlation functions in the section.II.3.3.

II.3.3. Two-point correlators

The two-point correlation functions can be used to determine the hadron mass and are important in the calculation of the matrix elements discussed in the next subsection. Given an operator with pion quantum numbers, such as

$$\chi_{\Phi}(x) = \bar{q}_1(x)\gamma_5 q_2(x) \tag{II.72}$$

where the $\bar{q}_1(y)$ and $q_2(y)$ are the anti-quark and quark operators, the dimensionless two-point correlator from Euclidean time t_i to Euclidean time t_f with momentum $\vec{p}$ is

$$\begin{aligned}
C_{AB}^{\Phi}(t_i, t_f, \vec{p}) =& a^6 \sum_{\vec{x}_f} e^{-i(\vec{x}_f - \vec{x}_i)\cdot\vec{p}} \left\langle 0 \left| \chi_{\Phi,B}(x_f) \chi_{\Phi,A}^{\dagger}(x_i) \right| 0 \right\rangle \\
=& a^6 \sum_{n,\vec{k}} \sum_{\vec{x}_f} e^{-i(\vec{x}_f - \vec{x}_i)\cdot\vec{p}} \left\langle 0 \left| \chi_{\Phi,B}(x_f) \right| n(\vec{k}) \right\rangle \times \\
& \frac{1}{2VE_{n(\vec{k})}} \left\langle n(\vec{k}) \left| \chi_{\Phi,A}^{\dagger}(x_i) \right| 0 \right\rangle \\
=& a^6 \sum_{n,\vec{k}} \sum_{\vec{x}_f} e^{-i(\vec{x}_f - \vec{x}_i)\cdot\vec{p}} \left\langle 0 \left| \chi_{\Phi,B}(x_i) e^{i(x_f - x_i)\cdot k} \right| n(\vec{k}) \right\rangle \times \\
& \frac{1}{2VE_{n(\vec{k})}} \left\langle n(\vec{k}) \left| \chi_{\Phi,A}^{\dagger}(x_i) \right| 0 \right\rangle \\
=& a^6 \sum_{n,\vec{k}} \sum_{\vec{x}_f} \left\langle 0 \left| \chi_{\Phi,B}(x_i) \right| n(\vec{k}) \right\rangle \times \\
& \frac{e^{-(t_f - t_i)E_{n(\vec{k})}}}{2VE_{n(\vec{k})}} \left\langle n(\vec{k}) \left| \chi_{\Phi,A}^{\dagger}(x_i) \right| 0 \right\rangle e^{i(\vec{x}_f - \vec{x}_i)\cdot(\vec{k} - \vec{p})} \\
=& a^3 \sum_{n,\vec{k}} \left\langle 0 \left| \chi_{\Phi,B}(x_i) \right| n(\vec{k}) \right\rangle \times
\end{aligned}$$

$$\frac{e^{-(t_f-t_i)E_{n(\vec{k})}}}{2E_{n(\vec{k})}}\left\langle n(\vec{k})\left|\chi^{\dagger}_{\Phi,A}(x_i)\right|0\right\rangle\delta^{(3)}_{\vec{k},\vec{p}}\,e^{-i\vec{x}_i\cdot(\vec{k}-\vec{p})}$$
$$=a^3\sum_n\left\langle 0\left|\chi_{\Phi,B}(x_i)\right|n(\vec{p})\right\rangle\left\langle n(\vec{p})\left|\chi^{\dagger}_{\Phi,B}(x_i)\right|0\right\rangle\frac{e^{-(t_f-t_i)E_{n(\vec{p})}}}{2E_{n(\vec{p})}}$$

For $t_f \gg t_i$, the ground state meson i.e. the pion dominates and the result becomes

$$\Gamma^{\pi\pi}_{AB}(t_i,t_f,\vec{p})\to a^3\left\langle 0\left|\chi_{\Phi,B}(x_i)\right|\pi(\vec{p})\right\rangle\left\langle\pi(\vec{p})\left|\chi^{\dagger}_{\Phi,A}(x_i)\right|0\right\rangle\frac{e^{-(t_f-t_i)E_{\pi(\vec{p})}}}{2E_{\pi(\vec{p})}} \tag{II.73}$$

For operator with nucleon quantum numbers,

$$\chi_N(y)=\epsilon^{lmn}[q_1(y)^{l^T}i\gamma_4\gamma_2\gamma_5 q_2^m(y)]q_3^n(y), \tag{II.74}$$

where $\{l,m,n\}$ are color indices, $q_1(y)$, $q_2(y)$ and $q_3(y)$ are the quark operators, the nucleon like two-point correlator is

$$C^N_{AB}(t_i,t_f,\vec{p})=a^6\sum_{\vec{x}_f}\Gamma e^{-i(\vec{x}_f-\vec{x}_i)\cdot\vec{p}}\left\langle 0\left|\chi_{N,B}(x_f)\chi^{\dagger}_{N,A}(x_i)\right|0\right\rangle, \tag{II.75}$$

where the projection operator is $\Gamma=\frac{1}{2}(1+\gamma_4)$, let $|0^+(\vec{p})>$ to be the positive parity ground state i.e. the nucleon state with energy $e^{-(t_f-t_i)E^+_{n(\vec{p})}}$

$$C^N_{AB}(t_i,t_f,\vec{p})=a^6\sum_n\left\langle 0\left|\chi_{\Phi,B}(x_i)\right|n(\vec{p})\right\rangle\left\langle n(\vec{p})\left|\chi^{\dagger}_{\Phi,B}(x_i)\right|0\right\rangle\times$$
$$e^{-(t_f-t_i)E^+_{n(\vec{p})}}\frac{E^+_{n(\vec{p})}+m^+}{2E^+_{n(\vec{p})}} \tag{II.76}$$

The dimensionless correlator from Euclidean time t_i to Euclidean time t_f with momentum $\vec{p}$ is

$$C^N_{AB}(t_i,t_f,\vec{p};\,T)=a^9\sum_{\vec{x}_f}e^{-i(\vec{x}_f-\vec{x}_i)\cdot\vec{p}}\,T_{\alpha\beta}\left\langle 0\left|\chi^N_{\beta B}(x_f)\bar{\chi}^N_{\alpha A}(x_i)\right|0\right\rangle$$
$$=a^9\sum_{n,\vec{k},s}\sum_{\vec{x}_f}e^{-i(\vec{x}_f-\vec{x}_i)\cdot\vec{p}}\,T_{\alpha\beta}\left\langle 0\left|\chi^N_{\beta B}(x_f)\right|n(\vec{k},s)\right\rangle\times$$
$$\frac{m_n}{VE_{n(\vec{k})}}\left\langle n(\vec{k},s)\left|\bar{\chi}^N_{\alpha A}(x_i)\right|0\right\rangle$$
$$=a^9\sum_{n,\vec{k},s}\sum_{\vec{x}_f}e^{-i(\vec{x}_f-\vec{x}_i)\cdot\vec{p}}\,T_{\alpha\beta}\left\langle 0\left|\chi^N_{\beta B}(x_i)e^{i(x_f-x_i)\cdot k}\right|n(\vec{k},s)\right\rangle\times$$
$$\frac{m_n}{VE_{n(\vec{k})}}\left\langle n(\vec{k},s)\left|\bar{\chi}^N_{\alpha A}(x_i)\right|0\right\rangle$$
$$=a^9\sum_{n,\vec{k},s}\sum_{\vec{x}_f}T_{\alpha\beta}\left\langle 0\left|\chi^N_{\beta B}(x_i)\right|n(\vec{k},s)\right\rangle\times$$

$$
\begin{aligned}
&\frac{m_n e^{-(t_f-t_i)E_{n(\vec{k})}}}{VE_{n(\vec{k})}} \left\langle n(\vec{k},s) \left| \bar{\chi}^N_{\alpha A}(x_i) \right| 0 \right\rangle e^{i(\vec{x}_f-\vec{x}_i)\cdot(\vec{k}-\vec{p})} \\
=&a^6 \sum_{n,\vec{k},s} T_{\alpha\beta} \left\langle 0 \left| \chi^N_{\beta B}(x_i) \right| n(\vec{k},s) \right\rangle \times \\
&\frac{m_n e^{-(t_f-t_i)E_{n(\vec{k})}}}{E_{n(\vec{k})}} \left\langle n(\vec{k},s) \left| \bar{\chi}^N_{\alpha A}(x_i) \right| 0 \right\rangle \delta^{(3)}_{\vec{k},\vec{p}} e^{-i\vec{x}_i\cdot(\vec{k}-\vec{p})} \\
=&a^6 \sum_{n,s} T_{\alpha\beta} \left\langle 0 \left| \chi^N_{\beta B}(x_i) \right| n(\vec{p},s) \right\rangle \left\langle n(\vec{p},s) \left| \bar{\chi}^N_{\alpha A}(x_i) \right| 0 \right\rangle \times \\
&\frac{m_n}{E_{n(\vec{p})}} e^{-(t_f-t_i)E_{n(\vec{p})}}
\end{aligned}
\tag{II.77}
$$

where $T_{\alpha\beta}$ is some generic 4×4 matrix in Dirac spin space, and α, β are Dirac indices. For $t_f \gg t_i$, the ground nucleon state dominates and the result becomes

$$
\begin{aligned}
&C^N_{AB}(t_i, t_f, \vec{p};\ T) \\
&\to a^6 \sum_s T_{\alpha\beta} \left\langle 0 \left| \chi^N_{\beta B}(x_i) \right| N(\vec{p},s) \right\rangle \left\langle N(\vec{p},s) \left| \bar{\chi}^N_{\alpha A}(x_i) \right| 0 \right\rangle \frac{m_N}{E_{N(\vec{p})}} e^{-(t_f-t_i)E_{N(\vec{p})}}
\end{aligned}
\tag{II.78}
$$

II.4. Nonperturbative renormalization

Renormalization of lattice operators is a necessary ingredient to obtain many physical results from numerical simulations. There are approaches to do the nonperturbative renormalization, such as the chiral Ward identities to determine the renormalization constants [114, 115, 115], fix non-perturbative renormalization conditions directly on hadronic matrix elements [116], and calculate the quantities perturbatively in one-loop both in the continuum and on the lattice in the Landau gauge [117].

A regularization independent momentum subtraction (RI/MOM) scheme method which avoids completely the use of lattice perturbation theory and allows a non-perturbative determination of the renormalization constants of any composite operator is proposed in Ref. [118]. In the following subsection, I will introduce this method through a simple fermion operator case.

Fermion Operator Renormalization: For simplicity, we consider the forward amputated Green function $\Gamma_O(pa)$ of a two-fermion bare lattice operator $O_q(a) = \bar{\psi}(x)\Gamma\psi(x)$, computed between off-shell quark states with four-momentum p, with $p^2 = \mu^2$ in the Landau gauge. We

define the renormalized operator $O_q(\mu)$,

$$O_q(\mu) = Z_O^{\text{RI-MOM}}\Big(\mu a, g(a)\Big) O_q(a). \tag{II.79}$$

where the $Z_O^{\text{RI-MOM}}$ renormalization constant. By imposing the renormalization condition, as shown in Fig. 3,

$$Z_O^{\text{RI-MOM}}\Big(\mu a, g(a)\Big) Z_\psi^{-1}\Big(\mu a, g(a)\Big) \Gamma_O(pa)|_{p^2=\mu^2} = 1, \tag{II.80}$$

where $Z_\psi^{1/2}$ is the field renormalization constant, to be defined below. This procedure defines a renormalized operator $O(\mu)$ which is independent of the regularization scheme [119, 120]. It depends, however, on the external states and on the gauge. This does not affect the final results, which, combined with the continuum calculation of the renormalization conditions, at any given order of perturbation theory, will be gauge invariant and independent of the external states. Let us specify the different quantities entering Eq. II.80. Γ_O is defined in terms of the expectation value of the non-amputated Green function $G_O(pa)$, and of the quark propagator $S(pa)$

$$\Gamma_O(pa) = \frac{1}{12}\text{tr}\left(\Lambda_O(pa)\hat{P}_O\right), \tag{II.81}$$

where

$$\Lambda_O(pa) = S(pa)^{-1} G_O(pa) S(pa)^{-1}. \tag{II.82}$$

$\hat{P}_O$ is a suitable projector on the tree-level operator: $\hat{P}_O = \hat{1}$ ($\hat{P}_O = \gamma_5$) for the scalar (pseudoscalar) density. The factor $1/12$ ensures the correct overall normalization of the trace (colour$\times$spin=12). Projectors are very convenient when defining Green functions, particularly in the non-perturbative case. They have been extensively used in refs. [120]. Of course one can also use other definitions of Z_O.

$Z_\psi^{1/2}$ is the renormalization constant of the fermion field. It can be defined in different ways, some of which are equivalently perturbative. Beyond perturbation theory, the most natural definition of Z_ψ is obtained from the amputated Green function of the conserve vector current V^C. Indeed, one knows that for V^C the renormalization constant is equal to one:

$$Z_{V^C}^{-1} = \Gamma_{V^C} \times Z_\psi^{-1} = \frac{1}{48}\text{tr}\left(\Lambda_{V_\mu^C}(pa)\gamma_\mu\right)|_{p^2=\mu^2} \times Z_\psi^{-1} = 1, \tag{II.83}$$

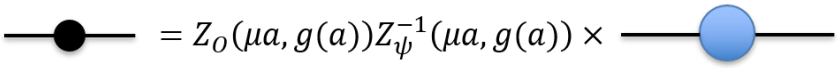

Figure 3 Non-perturbative renormalization condition. In the left hand side is the tree amputated Green's function, and the right hand side are the bare amputated Green's function and renormalization factors.

which implies

$$Z_\psi = \frac{1}{48}\mathrm{tr}\left(\Lambda_{V_\mu^C}(pa)\gamma_\mu\right)|_{p^2=\mu^2}. \tag{II.84}$$

The complete multiplicative renormalization constant in the $\overline{\mathrm{MS}}$ scheme needs a perturbative matching factor which converts from the RI-MOM renormalization at scale p^2 to the $\overline{\mathrm{MS}}$ scheme, in addition to the RI-MOM factors $Z_{\mathcal{O}}^{\text{RI-MOM}}(\mu_R^2)$,

$$Z^{\overline{\mathrm{MS}}}(\mu) = \mathcal{R}^{\overline{\mathrm{MS}}}(\mu, p^2)\, Z_{\mathcal{O}}^{\text{RI-MOM}}(p^2). \tag{II.85}$$

The conversion ratio $\mathcal{R}^{\overline{\mathrm{MS}}}(\mu, p^2)$ is derived up to 3-loop in Ref. [121],

$$\begin{aligned}\mathcal{R}^{\overline{\mathrm{MS}}}(\mu, p^2) &= 1 + \left[-\frac{517}{18} + 12\zeta_3 + \frac{5}{3}n_f\right]\left(\frac{\alpha_s}{4\pi}\right)^2 \\ &+ \left[-\frac{1287283}{648} + \frac{14197}{12}\zeta_3 + \frac{79}{4}\zeta_4 - \frac{1165}{3}\zeta_5 + \frac{18014}{81}n_f - \frac{368}{9}\zeta_3 n_f - \frac{1102}{243}n_f^2\right] \\ &\times \left(\frac{\alpha_s}{4\pi}\right)^3 + \mathcal{O}(\alpha_s^4).\end{aligned} \tag{II.86}$$

where n_f is the number of flavors and ζ_n is the Riemann zeta function evaluated at n. The strong coupling constant $\alpha_s(\mu)$ is evaluated in the $\overline{\mathrm{MS}}$ scheme by using its perturbative running to four loops [122]. The beta functions in the $\overline{\mathrm{MS}}$ scheme to 4-loops can be found in Ref. [123].

The renormalization condition needs to satisfy

$$\Lambda_{QCD} \ll \mu \ll 1/a, \tag{II.87}$$

to keep under control both non-perturbative and discretization effects. If such a window for μ does not exist, in current lattice simulations, an accurate matching of lattice operators to continuum ones becomes impossible in all methods.

Gluon Operator Renormalization: The common gluon operators definitions are,

$$\mathcal{O}_{\mu\nu}(z) \equiv \sum_{\alpha=0,1,2,3} \frac{1}{2}(\mathcal{O}(F^{\mu\alpha}, F_\alpha^\nu; z) + \mathcal{O}(F^{\nu\alpha}, F_\alpha^\mu; z))$$

$$-\frac{1}{4}\sum_{\alpha=0,1,2,3}\sum_{\beta=0,1,2,3}\mathcal{O}(F^{\alpha\beta},F^{\alpha}_{\beta};z), \tag{II.88}$$

with the operator $\mathcal{O}(F^{\mu}_{\nu},F^{\alpha}_{\beta};)$ defined by $F^{\mu}_{\nu}(z)U(z,0)F^{\alpha}_{\beta}(0)$. The field tensor $F_{\mu\nu}$ needed in the definition of the quasi-PDF operators is defined by

$$F_{\mu\nu}=\frac{i}{8a^2g}(\mathcal{P}_{[\mu,\nu]}+\mathcal{P}_{[\nu,-\mu]}+\mathcal{P}_{[-\mu,-\nu]}+\mathcal{P}_{[-\nu,\mu]}) \tag{II.89}$$

where the plaquette $\mathcal{P}_{\mu,\nu}=U_{\mu}(x)U_{\nu}(x+a\hat{\mu})U^{\dagger}_{\mu}(x+a\hat{\nu})U^{\dagger}_{\nu}(x)$ and $\mathcal{P}_{[\mu,\nu]}=\mathcal{P}_{\mu,\nu}-\mathcal{P}_{\nu,\mu}$. For the common gluon operators, the RI-MOM renormalization factor $Z_{\mathcal{O}}(\mu_R^2)$ can be obtained with the non-perturbative renormalization condition,

$$Z_g(p^2)Z^{\text{RI-MOM}}_{\mathcal{O}}(p^2)\Lambda^{\text{bare}}_{\mathcal{O}}(p)(\Lambda^{\text{tree}}_{\mathcal{O}}(p))^{-1}|_{p^2=\mu_R^2}=1, \tag{II.90}$$

where $Z_g(p^2)$ is the gluon field renormalization and $\Lambda_{\mathcal{O}}(p)$ is the amputated Green's function for the operator $\mathcal{O}$ in the Landau gauge-fixed gluon state. The tree level amputated Green's function is [124],

$$\begin{aligned}\Lambda^{\text{tree}}_{\mathcal{O}}(p)&=\langle\mathcal{O}_{\mu\nu}Tr[A_{\sigma}(p)A_{\tau}(-p)]\rangle^{\text{tree}}\\&=\frac{N_c^2-1}{2}(2p_{\mu}p_{\nu}g_{\sigma\tau}-p_{\tau}p_{\nu}g_{\sigma\mu}-p_{\tau}p_{\mu}g_{\sigma\nu}-p_{\sigma}p_{\nu}g_{\tau\mu}\\&-p_{\sigma}p_{\mu}g_{\tau\nu}+p_{\sigma}p_{\tau}g_{\mu\nu}-p^2g_{\sigma\tau}g_{\mu\nu}+p^2g_{\sigma\mu}g_{\tau\nu}+p^2g_{\sigma\nu}g_{\tau\mu})\end{aligned} \tag{II.91}$$

The gluon field renormalization $Z_g(p^2)$ is obtained through the gluon two-point function which is the trace of the gluon propagator,

$$D_{\mu\nu}(p)=\langle Tr[A_{\mu}(p)A_{\nu}(-p)]\rangle=Z_g(p^2)\frac{N_c^2-1}{2p^2}(g_{\mu\nu}-\frac{p_{\mu}p_{\nu}}{p^2}) \tag{II.92}$$

The gluon fields are calculated from the Landau gauge-fixed wilson link $U_{\mu}(x)$,

$$A_{\mu}(x+a\hat{e}_{\mu}/2)=\frac{1}{2ig_0}[(U_{\mu}(x)-U^{\dagger}_{\mu}(x))-\frac{1}{N_c}\text{Tr}(U_{\mu}(x)-U^{\dagger}_{\mu}(x))] \tag{II.93}$$

The momentum space lattice gluon fieds can be obtained with the Fourier transformation,

$$A_{\mu}(p)=\sum_x e^{-ip\dot{(}x+a\hat{e}_{\mu}/2)}A_{\mu}(x+a\hat{e}_{\mu}/2) \tag{II.94}$$

where $p_{\mu}=\frac{2\pi n_{\mu}}{aL_{\mu}}, n_{\mu}=0,...,L_{\mu}-1$. Therefore, the RI-MOM renormalization factor $Z^{\text{RI-MOM}}_{\mathcal{O}}(\mu_R^2)$

can be obtained from the wilson link $U_\mu(x)$.

Similar to the quark case, the complete multiplicative renormalization constant in the $\overline{\text{MS}}$ scheme is,

$$Z^{\overline{\text{MS}}}(\mu) = \mathcal{R}^{\overline{\text{MS}}}(\mu, p^2)\, Z_O^{\text{RI-MOM}}(p^2). \tag{II.95}$$

In this work, the 1-loop expression for this matching, derived in Ref. [125], is used:

$$\mathcal{R}^{\overline{\text{MS}}}(\mu^2, \mu_R^2) = 1 - \frac{g^2 N_f}{16\pi^2}\left(\frac{2}{3}\log(\mu^2/\mu_R^2) + \frac{10}{9}\right) - \frac{g^2 N_c}{16\pi^2}\left(\frac{4}{3} - 2\xi + \frac{\xi^2}{4}\right). \tag{II.96}$$

where N_f and N_c are the numbers of flavors and colors respectively, $\xi = 0$ in the Landau gauge, and g^2 is defined by $1/\alpha(\mu)$ [126, 127, 128]. The renormalization constant $Z^{\overline{\text{MS}}}$ can be used to calculate the renormalized gluon moments and gluon gravitational form factors of the nucleon and pion, where the renormalized gluon moments are calculated and used in the calculation of gluon PDF in the following pseudo-PDF sections.

III. Bjorken x-dependence PDF from lattice QCD

For decades, Bjorken x-dependence parton distributions cannot be directly determined in Euclidean lattice QCD, because their field-theoretic definition involves fields at light-like separations. One way to obtain the PDFs in lattice QCD is to calculate the Mellin moments. PDFs can be reconstructed from the inverse Mellin transform with a sufficient number of Mellin moments. However, the calculation is limited to the lowest three moments, because power-divergent mixing occurs between twist-two operators on the lattice. With this limitation, the lowest three moments are insufficient to fully reconstruct the momentum dependence PDFs without significant model dependence [129]. Moving beyond the lowest three moments requires overcoming the challenge of power-divergent mixing for lattice-QCD twist-two operators. One novel approach to this problem [130] builds upon the physical intuition that as long as the scale associated with the operator is taken to be much larger than the hadronic scale but much smaller than the inverse lattice spacing. Other approaches that avoid power-divergent mixing have also been suggested, including "auxiliary heavy/light quark" [131, 132, 133, 134], "operator product expansion (OPE) without OPE" [135, 136, 137, 138, 139, 140, 141, 142], and "hadronic tensor" [143, 144, 145, 146, 147, 148].

Following the proposal of Large-Momentum Effective Theory (LaMET) [149, 150, 151], many approaches are proposed to determining the x- dependence of PDFs directly from lattice QCD. The LaMET method calculates lattice quasi-distribution functions, defined in terms of matrix elements of equal-time and spatially separated operators, and then takes the infinite-momentum limit to extract the lightcone distribution. The quasi-PDF can be related to the P_z-independent lightcone PDF through a factorization theorem that factors from it a perturbative matching coefficient with corrections suppressed by the hadron momentum [150]. The factorization can be calculated exactly in perturbation theory [152, 153]. Many lattice works have been done on nucleon and meson PDFs, and generalized parton distributions (GPDs) based on the quasi-PDF approach [154, 155, 156, 157, 158, 159, 160, 161, 9, 6, 162, 10, 7, 163, 8, 164, 165, 166, 167, 168, 169, 170, 171, 172, 173, 174, 175, 176, 177, 178, 179, 180, 181]. Alternative approaches to lightcone PDFs in lattice QCD are "good lattice cross sections" [152, 182, 183, 184, 185] and the pseudo-PDF approach [186, 187, 188, 189, 190, 191, 192, 193, 194, 13, 12, 195, 196, 197]. In this chapter, we will mainly focus on the introduction of LaMET and

pseudo-PDF approaches in the Sec. III.1 and Sec. III.2 respectively.

III.1. Large Momentum Effective Theory

Feynman defined parton density in an infinite momentum frame (IMF). One can view a hadron as a beam of non-interacting partons (quarks and gluons) with the parton momentum density $q(x)$ and $g(x)$, where Bjorken $x = k_z/P_z$ is the fraction of longitudinal momentum of the parton, k_z is the parton momentum and P_z is the hadron momentum which goes to infinity to approach the light-cone property. Later, people found that the most convenient formulation of parton density is in the formalism of light-cone correlation. The unpolarized quark and gluon distribution in the nucleon in the light-cone coordinates [198],

$$q(x,\mu^2) = \int \frac{d\xi^-}{4\pi} e^{-ix\xi^- P^+} \langle P| \bar{\psi}(\xi^-)\gamma_+ e^{ig\int_0^{\xi^-} A_+(\xi^-)d\xi^-}\psi(0)\,|P\rangle\,,$$
$$xg(x,\mu^2) = \int \frac{d\xi^-}{2\pi P^+} e^{-ix\xi^- P^+} \langle P|F_\mu^+(\xi^-)\mathcal{P}e^{-ig\int_0^{\xi^-} d\eta^- A^+(\eta^-)}F^{\mu+}(0)|P\rangle$$

where the nucleon momentum P^μ is along the z-direction, $P^\mu = (P^0, 0, 0, P^z)$, and $|P\rangle$ is the hadron state with momentum P, μ^2 is the renormalization scale, A^+ is a gluon potential matrix in the fundamental representation, $F_{\mu\nu} = T^a G^a_{\mu\nu} = T^a(\partial_\mu A^a_\nu - \partial_\nu A^a_\mu - g f^{abc} A^b_\mu A^c_\nu)$ is the gluon field tensor, and

$$\xi^\pm = \frac{1}{2}(\xi^0 + \xi^3) \tag{III.1}$$

$\xi^\mu(\mu = 0, 1, 2, 3)$ is the space-time coordinates.

However, one cannot directly calculate time-dependent correlations in the framework of non-perturbative QCD on a Euclidean lattice. Large momentum effective theory is proposed to overcome this difficulty. In LaMET, one can fist construct a Euclidean quasi operator O which becomes the light-cone operator o in the infinite momentum frame (IMF) limit. There could be many operators O become to the same light-cone operator in the IMF limit. Any two operators leading to the same light-cone operator could linear combine into operators that become same light-cone operator in the IMF limit. Because O is an Euclidean operator, one can compute the matrix element of O on the lattice. $O(P_z, a)$ depends on the momentum of the hadron P_z and the lattice spacing a (providing UV cutoff). The light-front operator $o(\mu)$ can be extracted from

$O(P_z, a)$ at a large P_z through an effective theory,

$$O(P_z, a) = Z(P_z, \mu)o(\mu) + \mathcal{O}(1/(P_z)^2) + ... \tag{III.2}$$

Z contains all the lattice artifact, but only depends on the UV physics, can be calculated in perturbation theory. Parton distribution can be extracted by accurately calculating the matching factor Z and higher-order corrections.

III.1.1. Non-singlet quark quasi-PDF

In the early days, the quasi-PDF studies are mostly limited to isovector quark distributions in nucleon and valence-quark distribution in meson. The non-singlet quark quasi distribution is defined as[149],

$$\tilde{q}(x, \mu^2, P_z) = \int \frac{dz}{4\pi} e^{-ixzP_z} \langle P| O_\Gamma(z) |P\rangle , \tag{III.3}$$

where the $O_\Gamma(z)$ is u - d isovector qPDF operator:

$$O_\Gamma(z) \equiv \overline{u}(z)\Gamma U(z,0)u(0) - \overline{d}(z)\Gamma U(z,0)d(0), \tag{III.4}$$

where the Dirac Γ used will determine the quantum numbers of the quark PDF — $\Gamma = \gamma_t$, $\gamma_z\gamma_5$, $i\sigma_{zj}$ (with $j \neq z$), for the unpolarized, longitudinally polarized, transversity case respectively. The Wilson link U is defined along the z direction

$$U(z_2, z_1) = \mathcal{P}exp(-ig \int_{z_1}^{z_2} d\eta A^z(\eta)), \tag{III.5}$$

As we discuss in Chapter. II, the renormalization factor for the local operators can be calculated in the RI/MOM scheme. For the LaMET (non-local) operators, the quark NPR factors were done in Refs. [161, 160]. For the quark PDF, we use the RI-MOM renormalization constant defined via

$$Z_\Gamma^{\rm mp}(z, p_z^R, a^{-1}, \mu_R) = \left. \frac{{\rm Tr}[\mathcal{P}\Lambda_{\rm tree}(p, z, \gamma_t)]}{{\rm Tr}[\mathcal{P}\Lambda(p, z, \gamma_t)]} \right|_{p^2=\mu_R^2,\ p_z=p_z^R} . \tag{III.6}$$

For the unpolarized case, $\Lambda_{\rm tree}(p, z, \gamma_t) = \gamma_t e^{-izp_z}$ is the tree level matrix element in the momentum space, $\mathcal{P} = \gamma_t - (p_t/p_x)\gamma_x$ is the projection operator corresponding to the so-called minimal projection, where only the term with the Dirac structure proportional to γ_t is kept [199, 200]. For the polarized case, $\Lambda_{tree}(z, p_z, \gamma_z\gamma_5) = \gamma_z\gamma_5 e^{-ip_z z}$, and the projection operator

$\mathcal{P}$ is chosen to be $\mathcal{P} = \gamma_5\gamma_z/4$. $\Lambda_{tree}(z, p_z, \gamma_z\gamma_5) = \gamma_z\gamma_5 e^{-ip_z z}$. For the transversity case, $\Lambda_{tree}(z, p_z, \gamma_z\gamma_5) = \gamma_z\gamma_5 e^{-ip_z z}$, and the projection operator $\mathcal{P}$ is chosen to be $\mathcal{P} = \gamma_5\gamma_z/4$. $\Lambda_{tree}(z, p_z, \gamma_z\gamma_5) = \gamma_z\gamma_5 e^{-ip_z z}$. The renormalization constant $Z_\Gamma(z, p_z^R, a^{-1}, \mu_R)$ depends on the lattice spacing a, as well as the other two scales p_z^R and μ_R which are unphysical scales introduced in the RI/MOM scheme [199, 161]. The non-singlet quark quasi-PDF can be related to the P^z-independent light-front PDF through,

$$\tilde{q}(x, \Lambda, p_z) = \int_{-1}^{1} \frac{dy}{|y|} Z\left(\frac{x}{y}, \frac{\mu}{yp_z}, \frac{\Lambda}{p_z}\right) q(y, p^z, \mu) + \mathcal{O}\left(\frac{M^2}{p_z^2}, \frac{\Lambda_{\text{QCD}}^2}{p_z^2}\right) \tag{III.7}$$

where Λ indicates the approximate non-perturbative scale of QCD, μ is the renormalization scale, Z is a matching kernel and M is the nucleon mass. Here the $\mathcal{O}\left(M^2/p_z^2\right)$ terms are target-mass corrections and the $\mathcal{O}\left(\Lambda_{\text{QCD}}^2/p_z^2\right)$ terms are higher-twist effects, both of which are suppressed at large nucleon momentum.

III.1.2. Gluon quasi-PDF

Similar to the the quark quasi distribution, the gluon quasi distribution is defined as,

$$\tilde{g}(x, \mu^2, P_z) = \int \frac{dz}{2\pi x P_z} e^{ixzP_z} \langle P|O_g(z)|P\rangle \tag{III.8}$$

We use the gluon operators defined in Ref. [201], which are multiplicatively renormalizable,

$$\begin{aligned}
O_{g,1}(z) &\equiv \sum_{i\neq z,t} O(F^{ti}, F^{zi}; z), \\
O_{g,2}(z) &\equiv \sum_{i\neq z,t} O(F^{ti}, F^{ti}; z), \\
O_{g,3}(z) &\equiv \sum_{i\neq z,t} O(F^{zi}, F^{zi}; z), \\
O_{g,4}(z) &\equiv \sum_{\mu=0,1,2,3} O(F^{z\mu}, F^{z\mu}; z),
\end{aligned} \tag{III.9}$$

where $O(F^{\mu\nu}, F^{\alpha\beta}; z) = F^\mu_\nu(z)U(z, 0)F^\alpha_\beta(0)$. The renormalization factor of the gluon quasi-PDF in the RI/MOM scheme is provide in Refs. [201, 164],

$$[e^{\overline{\delta m}|z|} Z_{O_{g,i}} Z_g]^{-1}(zn, p_z^R, 1/a, \mu_R) =$$

$$\left.\frac{P_{ij}^{ab}\langle 0|T[A_{a,i}(p)O_{g,i}(z,0)A_{b,j}(-p)]|0\rangle|_{amp}}{P_{ij}^{ab}\langle 0|T[A_{a,i}(p)O_{g,i}(z,0)A_{b,j}(-p)]|0\rangle_{amp,tree}}\right|_{\substack{p^2=-\mu_R^2\\ p_z=p_z^R}}, \tag{III.10}$$

in the case of $O_{g,1}$, where $\delta m \sim O(1/a)$ is the mass counterterm. Here $A_{a,i}(p)$ denotes the momentum space gluon field with momentum p. Z_g is the gluon field renormalization constant. P_{ij}^{ab} is a projection operator with color indices a, b and Lorentz indices i, j. A simple example of the projection is $P_{ij}^{ab} = \delta^{ab} g_{\perp,ij}$. However, calculating the gluon renormalization nonperturbatively suffers worse signal-to-noise than the corresponding nucleon calculation, making it harder to apply this strategies.

The factorization for the renormalized singlet quark and gluon quasi-PDFs after the nonperturbative renormalization is provided in Ref. [201],

$$\begin{aligned}
&\{\tilde{q}_i, \tilde{g}\}(x, P_z, \mu^{\overline{\rm MS}}, \mu^{\rm RI}, p_z^{\rm RI}) \\
&= \int_0^1 \frac{dy}{|y|} C_{\{q_i,g\},q_j}\left(\frac{x}{y}, \left(\frac{\mu^{\rm RI}}{p_z^{\rm RI}}\right)^2, \frac{yP_z}{\mu^{\overline{\rm MS}}}, \frac{yP_z}{p_z^{\rm RI}}\right) q_j(y, \mu^{\overline{\rm MS}}) \\
&+ \int_0^1 \frac{dy}{|y|} C_{\{q_i,g\},g}\left(\frac{x}{y}, \left(\frac{\mu^{\rm RI}}{p_z^{\rm RI}}\right)^2, \frac{yP_z}{\mu^{\overline{\rm MS}}}, \frac{yP_z}{p_z^{\rm RI}}\right) g(y, \mu^{\overline{\rm MS}}) \\
&+ \mathcal{O}\left(\frac{\Lambda_{\rm QCD}^2}{x^2P_z^2}, \frac{\Lambda_{\rm QCD}^2}{(1-x)^2P_z^2}, \frac{m_N^2}{P_z^2}\right)
\end{aligned} \tag{III.11}$$

where $p_z^{\rm RI}$ and $\mu^{\rm RI}$ are the momentum of the off-shell quark and the renormalization scale in the RI/MOM-scheme nonperturbative renormalization (NPR), the summation of j is over all quarks/anti-quarks, the coefficients C_{gg}, C_{qg}, $C_{q_iq_j}$ and C_{gq} are derived in Ref. [164]. The residual terms, $\mathcal{O}\left(\frac{\Lambda_{\rm QCD}^2}{x^2P_z^2}, \frac{\Lambda_{\rm QCD}^2}{(1-x)^2P_z^2}, \frac{m_N^2}{P_z^2}\right)$, come from the nucleon-mass correction and higher-twist effects, suppressed by the nucleon momentum.

Beginning from the quark/gluon quasi-PDF operators, then implementing the RI/MOM scheme for renormalization and the matching conditions for quark/gluon, the theoretical basis for directly extracting the unpolarized quark and gluon PDFs from lattice simulations is well established through quasi-PDF method.

III.2. Pseudo-PDF method

The pseudo-PDF method was first introduced in Refs. [202, 203] for quark PDFs. The unpolarized gluon PDF case using pseudo-PDF approach was proposed in Ref. [204] and polarized

case was later presented in 2022 in Ref. [205] after this thesis began. The general dependence of the matrix element $M(z, p_z)$ on the hadron momentum p and the displacement of the quark and antiquark fields z can be expressed as a function of the Lorentz invariants $\nu = z \cdot p$ (Ioffe time [206, 207]) and z^2, where z and p are general 4-vectors. We can thus introduce the Ioffe time pseudo-distribution (pITD),

$$\mathcal{M}(\nu, z^2) \equiv M(z, p_z)\,. \tag{III.12}$$

To eliminate the ultraviolet divergences in the pITD, we construct the reduced pseudo-ITD (RpITD) by taking the ratio of the pITD to the corresponding z-dependent matrix element at $P_z = 0$, and further normalize the ratio by the matrix element at $z^2 = 0$ as done in the first quark pseudo-PDF calculation [186],

$$\mathscr{M}(\nu, z^2) = \frac{\mathcal{M}(zP_z, z^2)\mathcal{M}(0 \cdot P_z, 0)}{\mathcal{M}(z \cdot 0, z^2)/\mathcal{M}(0 \cdot 0, 0)}. \tag{III.13}$$

By construction, the RpITD double ratios employed here are normalized to one at $z = 0$. It is directly related to the PDFs as

$$\mathscr{M}_{q,g}(\nu, z^2) = I_{q,g}(\nu, \mu^2) + \mathcal{O}(z^2)\,, \tag{III.14}$$

with $\mu^2 = 1/z^2$. Here $I(\nu, \mu^2)$ is the Ioffe time PDF [206, 207],

III.2.1. Quark pseudo-PDF

The quark Ioffe time PDF $I_q(\nu, \mu^2)$ is the Fourier transform of the quark PDF,

$$q(x, \mu^2) = \int \frac{d\nu}{2\pi} e^{-ix\nu} I_q(\nu, \mu^2), \tag{III.15}$$

the quark RpITDs are connected to through the matching below while ignoring the $\mathcal{O}(z^2)$ terms,

$$\mathscr{M}_q(\nu, z^2) = \int_0^1 dx \frac{q(x, \mu^2)}{\langle x \rangle_q} R_{qq}(x\nu, z^2\mu^2), \tag{III.16}$$

where μ is the renormalization scale in $\overline{\text{MS}}$ scheme and $\langle x \rangle_g = \int_0^1 dx\, x g(x, \mu^2)$ is the gluon momentum fraction of the nucleon.

$$R_{qq}(y, z^2, \mu^2) = \cos y - \frac{\alpha_s(\mu)}{2\pi} N_c \times$$

$$\left\{\left[\ln\left(z^2\mu^2\frac{e^{2\gamma_E+1}}{4}\right)+2\right]R_{q,B}(y)+R_{q,L}(y)\right\}, \tag{III.17}$$

where α_s is the strong coupling at scale μ, $N_c = 3$ is the number of colors, and $\gamma_E = 0.5772$ is the Euler-Mascheroni constant. For the term $R_{qq}(y, z^2, \mu^2)$, z was chosen to be $2e^{-\gamma_E-1/2}/\mu$ so that the logarithmic term vanishes, which suppresses the residuals containing higher order logarithmic terms, following the previous publication regarding the one-loop evolution of the pseudo-PDF [192]. Equation III.16 and the terms $R_{q,B}(y)$, $R_{q,L}(y)$ are defined in Eqs. 16 and 24 in Ref. [192].

III.2.2. Gluon pseudo-PDF

All the quark and gluon operators in Eq. III.4 and III.9 can be also used in pseudo-PDF method. Another unpolarized gluon operator is introduced in Ref. [204],

$$\mathcal{O}(z) \equiv \sum_{i\neq z,t}\mathcal{O}(F^{ti}, F^{ti}; z) - \sum_{i,j\neq z,t}\mathcal{O}(F^{ij}, F^{ij}; z), \tag{III.18}$$

which can directly used in the pseudo-PDF matching Eq. V.12. The gluon RpITDs are connected to through the matching below while ignoring the $\mathcal{O}(z^2)$ terms,

$$\begin{aligned}\mathscr{M}_g(\nu, z^2) = &\int_0^1 dx \frac{xg(x,\mu^2)}{\langle x\rangle_g} R_{gg}(x\nu, z^2\mu^2)\\ &+\frac{P_z}{P_0}\int_0^1 dx \frac{xq_S(x,\mu^2)}{\langle x\rangle_g} R_{gq}(x\nu, z^2\mu^2),\end{aligned} \tag{III.19}$$

where μ is the renormalization scale in $\overline{\text{MS}}$ scheme and $\langle x\rangle_g = \int_0^1 dx\, xg(x,\mu^2)$ is the gluon momentum fraction of the nucleon.

$$\begin{aligned}R_{gg}(y, z^2, \mu^2) = &\cos y - \frac{\alpha_s(\mu)}{2\pi}N_c\times\\ &\left\{\left[\ln\left(z^2\mu^2\frac{e^{2\gamma_E+1}}{4}\right)+2\right]R_{g,B}(y)+R_{g,L}(y)+R_{g,C}(y)\right\},\end{aligned} \tag{III.20}$$

Equation V.12 and the terms $R_{g,B}(y)$, $R_{g,L}(y)$, $R_{g,C}(y)$ are defined in Eqs. 7.21–23 and in the paragraph below Eq. 7.23 in Ref. [204]. Note that the lattice-calculated RpITDs are also connected to the singlet quark-PDF q_s via the quark-gluon matching kernel R_{gq} with an additional non-singlet quark term added to Eq. V.12.

Quasi-PDF (LaMET) and the pseudo-PDF approaches are faced with different technical problems of inferring the PDF from a Fourier transform due to the data in a limited range of z

or ν. Such effects have been discussed in [157, 208]. In particular, because x is the Fourier dual of ν, accessing a limited range of ν (or z) has the effect of introducing uncontrolled systematic errors at small x (roughly $x \lesssim 0.15$ for existing lattice calculations). These systematic errors can be controlled using increasingly large values of ν, although this requires an increased computational power. Therefore, improved computational methods are required to reliably extract PDFs at small x.

III.3. Nucleon Isovector Quark PDFs

With the well established quasi-PDF and pseudo-PDF approaches for quark PDF, lattice community significantly improves quantitative results on extracting x-dependent PDFs from lattice QCD. In the beginning of this chapter, we introduced many of these quark quasi-PDF and pseudo-PDF calculations. In this section, we will present more recent calculations of nucleon isovector quark distributions done at the physical pion mass.

The first unpolarized PDFs at the physical pion mass [209, 157] using the quasi-PDFs approach were determined using small momentum for unpolarized, helicity and transversity quark and antiquark distributions [210, 155, 211, 158, 156]. In the more recent studies, unpolarized, helicity and transversity quark PDFs are determined using much larger momentum at phyiscal pion mass. From top to bottom, each row of Fig. 4 shows the newer PDF results on ensembles with momenta above 2 GeV, and then renormalized at $\mu = \{3, 3, \sqrt{2}\}$ GeV, for isovector quark unpolarized [7], helicity [7], and transversity [8] PDFs, respectively. The lattice results agree with global fit unpolarized PDFs CT14 [26], NNPDF3.1 [15], CJ15 [16], helicity PDFs NNPDFpol1.1 [18], JAM17 [19], and transversity PDFs JAM17 [19], LMPSS17 [20], respectively. In the small-x region, larger zP_z data are needed for lattice calculations to have better control. The lattice QCD calculations can now obtain the non-singlet quark PDFs at physical pion mass at higher and higher momentum. The lattice-QCD calculations is not far away from providing an great impact on global analyzed PDFs with a better control on the current uncertainties.

Most x-dependence PDF lattice QCD calculations, however, are done using the popular quasi-PDF and pseudo-PDF techniques and mostly limited to isovector quark distributions in the nucleon and the valence-quark distribution in the pion and kaon. Gluon distributions in the

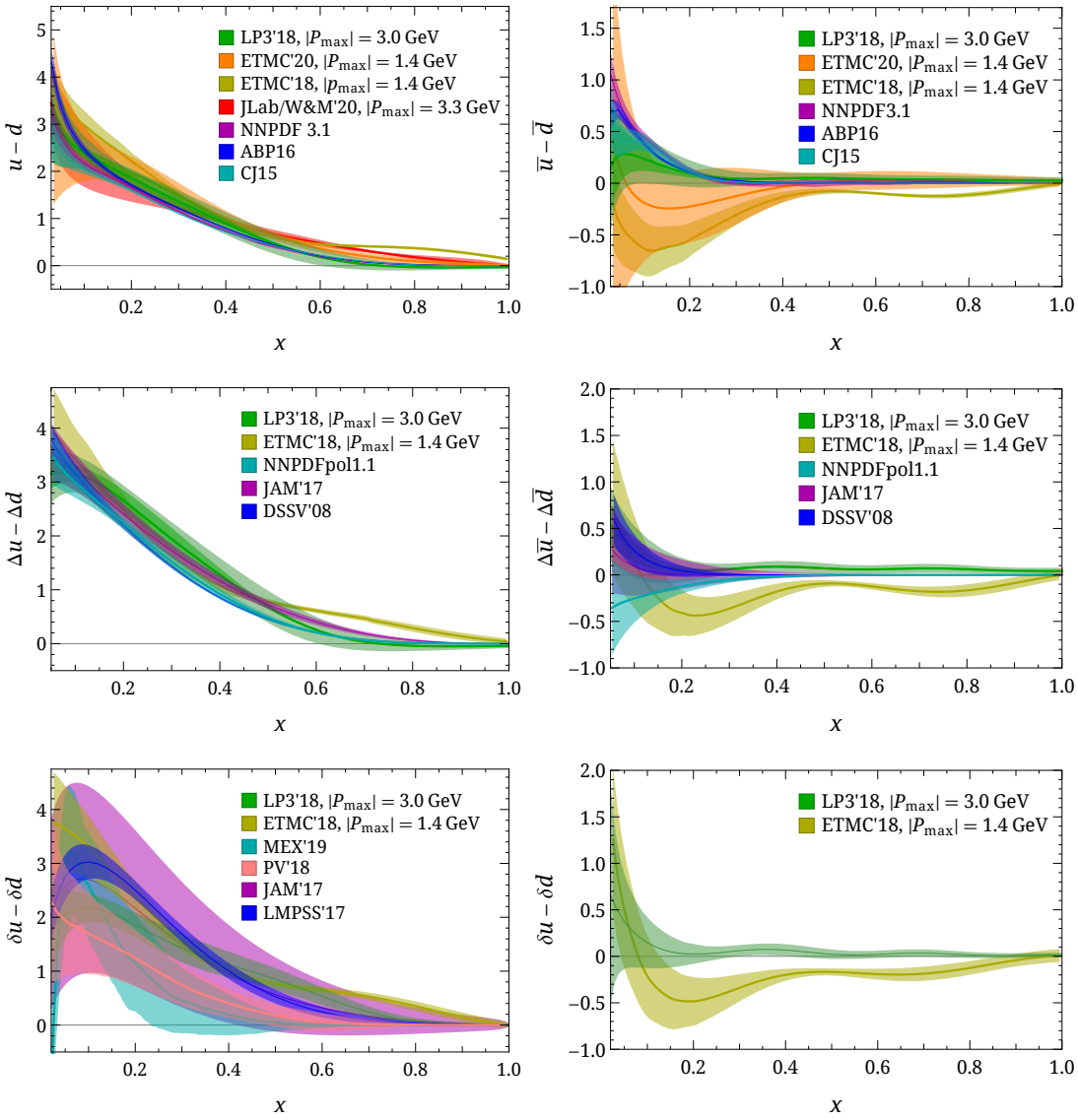

Figure 4 The lattice calculations of isovector nucleon unpolarized (top), helicity (middle) and transversity (bottom) with quark&antiquark, left&right column respectively, taken from [6, 7, 8, 9, 10, 11, 12, 13, 14, 15, 16, 17, 18, 19, 20, 21, 22]. These figures are taken from reference [23].

nucleon, pion and kaon are not studied on the lattice until this thesis started [163, 195, 212, 213, 214]. In this thesis, we present the first study of x-dependence gluon nucleon and pion distributions in the following Chapter. V and IV.

IV. Meson gluon PDF results

The lightest bound state in quantum chromodynamics (QCD), the pion, plays a fundamental role, since it is the Nambu-Goldstone boson of dynamical chiral symmetry breaking (DCSB). Studies of pion and kaon structure reveal the physics of DCSB, help to reveal the relative impact of DCSB versus the chiral symmetry breaking by the quark masses, and are important to understand nonperturbative QCD. Studying the pion parton distribution functions (PDFs) is important to characterize the structure of the pion and further understand DCSB and nonperturbative QCD [215, 43, 44]. Currently, we know less about the pion PDFs than the nucleon PDFs, because there are fewer experimental data sets for the global analysis of the pion PDFs, especially for the sea-quark and gluon distributions. The future U.S.-based Electron-Ion Collider (EIC) [42], planned to be built at Brookhaven National Lab, will further our knowledge of pion structure [43, 44]. In China, a similar machine, the Electron-Ion Collider in China (EicC) [45], is also planned to make impacts on the pion gluon and sea-quark distributions. In Europe, the Drell-Yan and J/ψ-production experiments from COMPASS++/AMBER [216] will aim at improving our knowledge of both the pion gluon and quark PDFs.

Global analyses of pion PDFs mostly rely on Drell-Yan data. The early studies of pion PDFs were based mostly on pion-induced Drell-Yan data and used J/ψ-production data or direct photon production to constrain the pion gluon PDF [50, 51, 52, 5, 53]. There are more recent studies, such as the work by Bourrely and Soffer [54], that extract the pion PDF based on Drell-Yan π^+W data. JAM Collaboration [4, 24] uses a Monte-Carlo approach to analyze the Drell-Yan πA and leading-neutron electroproduction data from HERA to reach the lower-x region, and revealed that gluons carry a significantly higher momentum fraction (about 30%) in the pion than had been inferred from Drell-Yan data alone. The xFitter group [3] analyzed Drell-Yan πA and photoproduction data using their open-source QCD fit framework for PDF extraction and found that these data can constrain the valence distribution well but are not sensitive enough for the sea and gluon distributions to be precisely determined. The analysis done Ref. [55] suggests that the pion-induced J/ψ-production data has additional constraint on pion PDFs, particularly in the pion gluon PDF in the large-x region. All in all, the pion valence-quark distributions are better constrained than the gluon distribution from the global analysis of

experimental data. While waiting for more experimental data sets, the study of the pion gluon distribution from theoretical side can provide useful information for the experiments.

The pion gluon PDF is rarely studied using continuum-QCD phenomenological models or through lattice-QCD (LQCD) simulations. Most model studies only predict the pion valence-quark distribution [217, 218, 219, 220, 221, 222, 223, 224, 225, 226, 227, 228, 229, 230, 231], but the gluon and sea PDFs are predicted by the Dyson-Schwinger equation (DSE) continuum approach [25, 232]. The prediction of the pion gluon PDF in DSE, based on an implementation of rainbow-ladder truncation of DSE, is consistent with the JAM pion gluon PDF result [4, 24] within two sigma. LQCD provides an first-principles calculations to improve our knowledge of nonperturbative pion gluon structure; however, there have been only two efforts to determine the first moment of pion gluon PDF [233, 234]. An early calculation in 2000 using quenched QCD predicted $\langle x\rangle_g = 0.37(8)(12)$, using Wilson fermion action with a lattice spacing $a = 0.093$ fm, lattice size $L^3 \times T = 24^4$, a large 890-MeV pion mass and 3,066 configurations at $\mu^2 = 4$ GeV^2 [233]. A more recent study in 2018 using $N_f = 2 + 1$ clover fermion action with a lattice spacing $a = 0.1167(16)$ fm, larger lattice size $32^3 \times 96$, 450-MeV pion mass, and 572,663 measurements, gave a larger first-moment result, $\langle x\rangle_g = 0.61(9)$ at $\mu^2 = 4$ GeV^2 [234]. In principle, a series of moments can be used to reconstruct the PDF. Although there are calculations of the first moment of the pion gluon PDF, there is little chance that sufficient higher moments of the pion gluon PDF can be obtained to perform such a reconstruction. A direct lattice calculation of the x-dependence of the pion gluon PDF is needed.

Only recently have lattice calculations of the gluon PDF become possible, when the necessary one-loop matching relations of the gluon PDF were computed for the pseudo-PDF [204] and quasi-PDF [201, 164] approaches. Both approaches make direct calculation of the x dependence of the pion gluon PDF feasible. In this work, we apply the pseudo-PDF method by using the ratio renormalization scheme to avoid the difficulty of calculating the gluon renormalization factors. We follow a developed procedure for using the pseudo-PDF method to obtain light-cone PDFs from Ioffe-time distributions (ITDs) by matching through two steps, evolution and scheme conversion [192, 186, 190, 12]. Another commonly used procedure is direct matching to the lightcone ITDs [191, 13]. Using the pseudo-PDF method also allows us to use lattice correlators at all boost momenta at small Ioffe-time. There have been a number of successful

pseudo-PDF calculations of nucleon isovector PDFs [186, 190, 13, 12] and pion valence-quark PDFs [191]. The earliest calculation was done on a quenched lattice [186], then the pion masses were set closer to the physical pion mass [190, 191, 13], and the calculation at physical pion mass was done recently [12]. The lattice-calculated PDFs in Refs. [190, 191, 13, 12] show good agreement with the global-analysis PDFs.

In this work, we present the first calculation of the full x-dependent pion gluon distribution using the pseudo-PDF method from two lattice spacings, 0.12 and 0.15 fm, and three pion masses: 690, 310 and 220 MeV. The rest of the paper is organized as follows. We present the procedure to obtain the lightcone gluon PDF from the reduced pseudo-ITDs, the numerical setup of lattice simulation, and how we extracted the reduced pseudo-ITDs from lattice calculated correlators, the final determination of the pion gluon PDF from our lattice calculations is compared with the NLO xFitter [3] and JAM pion gluon PDFs [4, 24], and the systematics induced by different steps are studied, and the lattice-spacing and pion-mass dependence are investigated.

IV.1. Ioffe-time distribution

In this thesis, we use the gluon pseudo-PDF matching introduced in Sec. III.2 and the unpolarized gluon operator defined in Eq. V.26. We neglect the pion quark PDF, since the total quark PDF is found to be much smaller than the gluon PDF in global fits [4, 3]. We will later estimate the systematic uncertainty introduced by this assumption. The gluon evolved pITD (EpITD), G is obtained by using the evolution term $R_1(y, z^2\mu^2)$,

$$G(\nu, \mu) = \mathscr{M}(\nu, z^2) + \int_0^1 dx R_1(x, z^2\mu^2)\mathscr{M}(x\nu, z^2). \tag{IV.1}$$

The z dependence of the EpITDs should be compensated by the $\ln z^2$ term in the evolution formula. In principle, the EpITD G is free of z dependence and is connected to the lightcone gluon PDF $g(x, \mu^2)$ through the scheme-conversion term $R_2(y)$,

$$G(\nu, \mu) = \int_0^1 dx \, \frac{xg(x, \mu^2)}{\langle x \rangle_g} R_2(x\nu), \tag{IV.2}$$

so the gluon PDF $g(x, \mu^2)$ can be extracted by inverting this equation.

On the lattice, we use clover valence fermions on three ensembles with $N_f = 2 + 1 + 1$

highly improved staggered quarks (HISQ) [71] generated by the MILC Collaboration [63, 64, 235, 236] with two different lattice spacings ($a \approx 0.12$ and 0.15 fm) and three pion masses (220, 310, 690 MeV). The masses of the clover quarks are tuned to reproduce the lightest light and strange sea pseudoscalar meson masses used by PNDME Collaboration [237, 238, 239, 240]. We use five HYP-smearing [89] steps on the gluon loops to reduce the statistical uncertainties, as studied in Ref. [163]. We use Gaussian momentum smearing for the quark fields [107] $q(x)+\alpha\sum_j U_j(x)e^{i(\frac{2\pi}{L})\mathbf{k}\hat{e}_j}q(x+\hat{e}_j)$, to reach higher meson boost momenta with the momentum-smearing parameter **k** listed in Table 4. Table 4 gives the lattice spacing a, valence pion mass M_π^{val} and η_s mass $M_{\eta_s}^{\text{val}}$, lattice size $L^3\times T$, number of configurations N_{cfg}, number of total two-point correlator measurements $N_{\text{meas}}^{\text{2pt}}$, and separation time t_{sep} used in the three-point correlator fits for the three ensembles. This allows us to reach the continuum limit and physical pion mass through extrapolation. The total amount of measurements vary in 10^5–10^6 for different ensembles.

ensemble	a12m220	a12m310	a15m310
a (fm)	0.1184(10)	0.1207(11)	0.1510(20)
M_π^{val} (MeV)	226.6(3)	311.1(6)	319.1(31)
$M_{\eta_s}^{\text{val}}$ (MeV)	696.9(2)	684.1(6)	687.3(13)
$L^3\times T$	$32^3\times 64$	$24^3\times 64$	$16^3\times 48$
P_z (GeV)	$[0, 2.29]$	$[0, 2.14]$	$[0, 2.05]$
k	3.9	2.9	2.3
N_{cfg}	957	1013	900
$N_{\text{meas}}^{\text{2pt}}$	731,200	324,160	21,600
t_{sep}	{5,6,7,8,9}	{5,6,7,8,9}	{4,5,6,7}

Table 1 Lattice spacing a, valence pion mass M_π^{val} and η_s mass $M_{\eta_s}^{\text{val}}$, lattice size $L^3\times T$, number of configurations N_{cfg}, number of total two-point correlator measurements $N_{\text{meas}}^{\text{2pt}}$, and separation times t_{sep} used in the three-point correlator fits of $N_f = 2+1+1$ clover valence fermions on HISQ ensembles generated by MILC Collaboration and analyzed in this study.

The two-point correlator for a meson Φ is

$$\begin{aligned} C_\Phi^{\text{2pt}}(P_z;t) &= \int dy^3 e^{-iy\cdot P_z}\langle\chi_\Phi(\vec{y},t)|\chi_\Phi(\vec{0},0)\rangle \\ &= |A_{\Phi,0}|^2 e^{-E_{\Phi,0}t} + |A_{\Phi,1}|^2 e^{-E_{\Phi,1}t} + ..., \end{aligned} \tag{IV.3}$$

where P_z is the meson momentum in the z-direction, $\chi_\Phi = \bar{q}_1\gamma_5 q_2$ is the pseudoscalar-meson interpolation operator, t is the Euclidean time, and $|A_{\Phi,i}|^2$ and $E_{\Phi,i}$ are the amplitude and energy for the ground-state ($i=0$) and the first excited state ($i=1$), respectively.

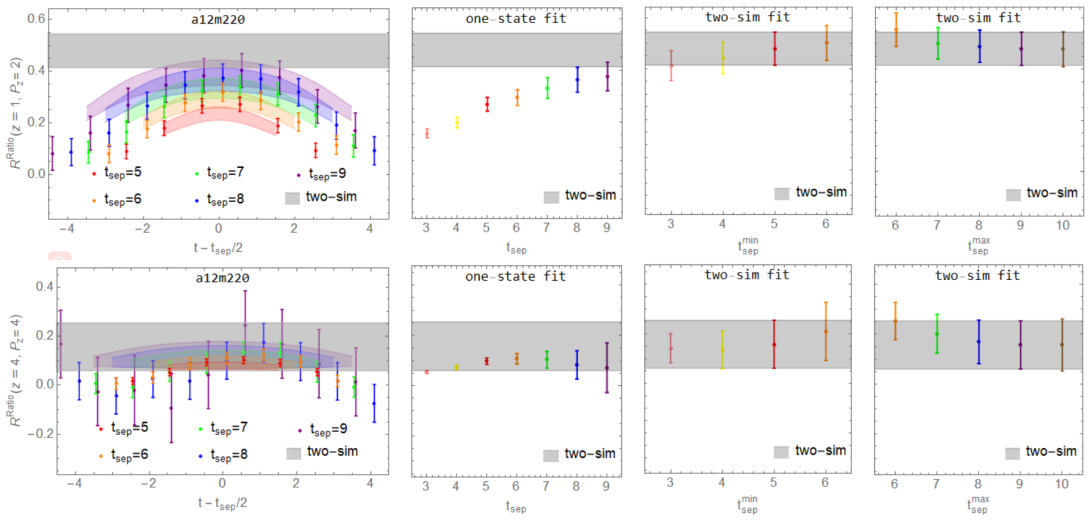

Figure 5 Example ratio plots (left), one-state fits (second column) and two-sim fits (last 2 columns) from the lightest pion mass $a \approx 0.12$ fm, $M_\pi \approx 220$ MeV for $P_z = 2 \times 2\pi/L$, $z = 1$ (upper row) and $P_z = 4 \times 2\pi/L$, $z = 4$ (lower row). The gray band shown on all plots is the extracted ground-state matrix element from the two-sim fit using $t_{\text{sep}} \in [5, 9]$. From left to right, the columns are: the ratio of the three-point to two-point correlators with the reconstructed fit bands from the two-sim fit using $t_{\text{sep}} \in [5, 9]$, shown as functions of $t - t_{\text{sep}}/2$, the one-state fit results for the three-point correlators at each $t_{\text{sep}} \in [3, 9]$, the two-sim fit results using $t_{\text{sep}} \in [t_{\text{sep}}^{\text{min}}, 9]$ as functions of $t_{\text{sep}}^{\text{min}}$, and the two-sim fit results using $t_{\text{sep}} \in [5, t_{\text{sep}}^{\text{max}}]$ as functions of $t_{\text{sep}}^{\text{max}}$.

The three-point gluon correlators are obtained by combining the gluon loop with pion two-point correlators. The matrix elements of the gluon operators can be obtained by fitting the three-point correlators to the energy-eigenstate expansion,

$$
\begin{aligned}
&C_\Phi^{\text{3pt}}(z, P_z; t_{\text{sep}}, t) \\
&= \int d^3y\, e^{-iy\cdot P_z} \langle \chi_\Phi(\vec{y}, t_{\text{sep}}) | \mathcal{O}(z,t) | \chi_\Phi(\vec{0}, 0) \rangle \\
&= |A_{\Phi,0}|^2 \langle 0|\mathcal{O}|0\rangle e^{-E_{\Phi,0} t_{\text{sep}}} + |A_{\Phi,0}||A_{\Phi,1}| \langle 0|\mathcal{O}|1\rangle e^{-E_{\Phi,1}(t_{\text{sep}}-t)} e^{-E_{\Phi,0} t} \\
&+ |A_{\Phi,0}||A_{\Phi,1}| \langle 1|\mathcal{O}|0\rangle e^{-E_{\Phi,0}(t_{\text{sep}}-t)} e^{-E_{\Phi,1} t} + |A_{\Phi,1}|^2 \langle 1|\mathcal{O}|1\rangle e^{-E_{\Phi,1} t_{\text{sep}}} + \ldots,
\end{aligned}
\tag{IV.4}
$$

where t_{sep} is the source-sink time separation, and t is the gluon-operator insertion time. The amplitudes and energies, $A_{\Phi,0}$, $A_{\Phi,1}$, $E_{\Phi,0}$ and $E_{\Phi,1}$, are obtained from the two-state fits of the two-point correlators. $\langle 0|\mathcal{O}|0\rangle$, $\langle 0|\mathcal{O}|1\rangle$ ($\langle 1|\mathcal{O}|0\rangle$), and $\langle 1|\mathcal{O}|1\rangle$ are the ground-state matrix element, the ground–excited-state matrix element, and the excited-state matrix element, respectively. We extract the ground-state matrix element $\langle 0|\mathcal{O}|0\rangle$ from the two-state fit of the three-point correlators, or a two-state simultaneous "two-sim" fit on multiple separation times

with the $\langle 0|\mathcal{O}|0\rangle$, $\langle 0|\mathcal{O}|1\rangle$ and $\langle 1|\mathcal{O}|0\rangle$ terms.

To verify that our fitted matrix elements are reliably extracted, we compare to ratios of the three-point to the two-point correlator

$$R^{\text{ratio}}(z, P_z; t_{\text{sep}}, t) = \frac{C^{\text{3pt}}(z, P_z; t_{\text{sep}}, t)}{C^{\text{2pt}}(P_z; t_{\text{sep}})}; \tag{IV.5}$$

if there were no excited states, the ratio would be the ground-state matrix element. The left-hand side of Fig. 25 shows example ratios for the gluon matrix elements from the lightest pion ensemble, a12m220, at selected momenta P_z and Wilson-line length z. We see the ratios increase with increasing source-sink separation going from 0.60 to 1.08 fm. At large separation, the ratios begin to converge, indicating the neglect of excited states becomes less problematic. The gray bands indicate the ground-state matrix elements extracted using the two-sim fit to three-point correlators at five t_{sep}. The convergence of the fits that neglect excited states can also be seen in second column of Fig. 25, where we compare one-state fits from each source-sink separations: the one-state fit results increase as t_{sep} increases, starting to converge at large t_{sep} to the two-sim fit results.

The third and fourth columns of Fig. 25 show two-sim fits using $t_{\text{sep}} \in [t_{\text{sep}}^{\text{min}}, 9]$ and $t_{\text{sep}} \in [5, t_{\text{sep}}^{\text{max}}]$ to study how the two-sim ground-state matrix elements depend on the source-sink separations input into fit. We observe that the matrix elements are consistent with each other within one standard deviation, showing consistent extraction of the ground-state matrix element, though the statistical errors are larger than those of the one-state fits. We observe larger fluctuations in the matrix element extractions when small $t_{\text{sep}}^{\text{min}} = 3$ and 4, or small $t_{\text{sep}}^{\text{max}} = 6$ and 7, are used. The ground state matrix element extracted from two-sim fits becomes very stable when $t_{\text{sep}}^{\text{min}} > 4$ and $t_{\text{sep}}^{\text{max}} > 7$.

Figure 6 shows the RpITD of the same examples $P_z = 2\times 2\pi/L$, $z = 1$ and $P_z = 4\times 2\pi/L$, $z = 4$ from two-sim fit results using $t_{\text{sep}} \in [t_{\text{sep}}^{\text{min}}, 9]$. The RpITD results, which are constructed to suppress lattice fluctuations, are very stable over the range of different fits considered. For a12m310 and a15m310 ensembles, the t_{sep} dependence of RpITDs is milder than those from a12m220 ensemble due to the heavier pion mass. Overall, our ground-state RpITDs from the two-sim fit are stable, and we use them to extract the gluon PDF.

Using the RpITDs extracted in the previous section, we examine the pion-mass and lattice-

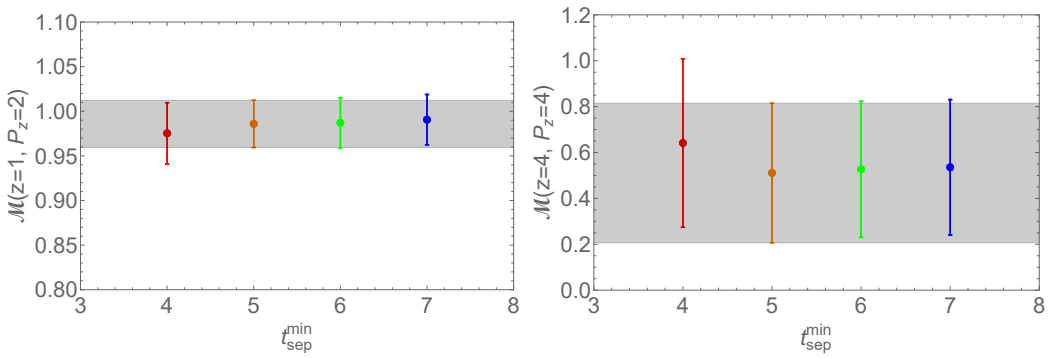

Figure 6 Example RpITDs from the a12m220 ensemble as functions of $t_{\rm sep}^{\rm min}$ for $P_z = 2 \times 2\pi/L$, $z = 1$ (top) and $P_z = 4 \times 2\pi/L$, $z = 4$ (bottom). The two-sim fit RpITD results using $t_{\rm sep} \in [t_{\rm sep}^{\rm min}, 9]$ are consistent with the ones final chosen $t_{\rm sep} \in [5, 9]$.

spacing dependence. The top of Fig. 26 shows the η_s RpITDs at boost momentum around 2 GeV as functions of the Wilson-line length z for the a12m220, a12m310, and a15m310 ensembles. We see no noticeable lattice-spacing dependence. The bottom of Fig. 26 shows the pion RpITDs with boost momentum around 1.3 GeV for the same ensembles. Again, there is no visible lattice-spacing or pion-mass dependence.

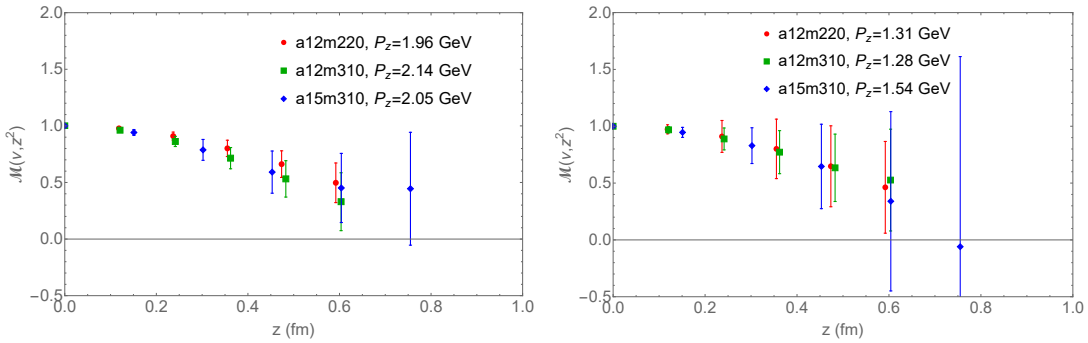

Figure 7 The η_s (top) and pion (bottom) RpITDs at boost momenta $P_z \approx 2$ GeV and 1.3 GeV, respectively, for the a12m220, a12m310, and a15m310 ensembles. In both cases, we observe weak lattice-spacing and pion-mass dependence.

To extract gluon PDFs, we follow the steps in Sec. V.3.1 between Eq. V.10 and Eq. IV.1 by first obtaining EpITDs and using Eq. IV.2 to extract $g(x)$. To obtain EpITDs, we need the RpITD $\mathscr{M}(\nu, z^2)$ to be a continuous function of ν to evaluate the $x \in [0, 1]$ integral in Eq. IV.1. We achieve this by using a "z-expansion"[1] fit [241, 242] following previous quark pseudo-PDF

[1]Note that the z in the "z-expansion" is not related to the Wilson link length z we use elsewhere.

calculations [191]. The following form is used [191]:

$$\mathscr{M}(\nu, z^2, a, M_\pi) = \sum_{k=0}^{k_{\max}} \lambda_k \tau^k, \tag{IV.6}$$

where $\tau = \frac{\sqrt{\nu_{\text{cut}}+\nu}-\sqrt{\nu_{\text{cut}}}}{\sqrt{\nu_{\text{cut}}+\nu}+\sqrt{\nu_{\text{cut}}}}$. Then, we use the fitted $\mathscr{M}(\nu, z^2)$ in the integral in Eq. IV.1. The fits are performed by minimizing the χ^2 function,

$$\chi^2_{\mathscr{M}}(a, M_\pi) = \sum_{\nu,z} \frac{(\mathscr{M}(\nu, z^2) - \mathscr{M}(\nu, z^2, a, M_\pi)^2}{\sigma^2_{\mathscr{M}}(\nu, z^2, a, M_\pi)}. \tag{IV.7}$$

The z-dependence in the $\mathscr{M}(u\nu, z^2)$ term of the evolution function comes from the one-loop matching term, which is a higher-order correction compared to the tree-level term; thus, the z-dependence can be neglected in $\mathscr{M}(\nu, z^2)$ in the integral in Eq. IV.1. We adopt as the best value $\nu_{\text{cut}} = 1$, as used in Ref. [191], but we also vary ν_{cut} in the range $[0.5, 2]$, and the results are consistent. We fix $\lambda_0 = 1$ to enforce the RpITD $\mathscr{M}(\nu, z^2)$ in Eq. V.11. The expansion order $k_{\max} = 3$ is used, because we can fit all the data points of $P_z \in [1, 5] \times 2\pi/L$ ($P_z \in [1, 7] \times 2\pi/L$ for a12m220 ensemble) and z up to 0.6 fm with $\chi^2/\text{dof} < 1$ using a 4-term z-expansion for each ensemble. The reconstructed bands from "z-expansion" on RpITDs are shown in the upper plot in Fig. 8. They describe the RpITD data points well for all ensembles.

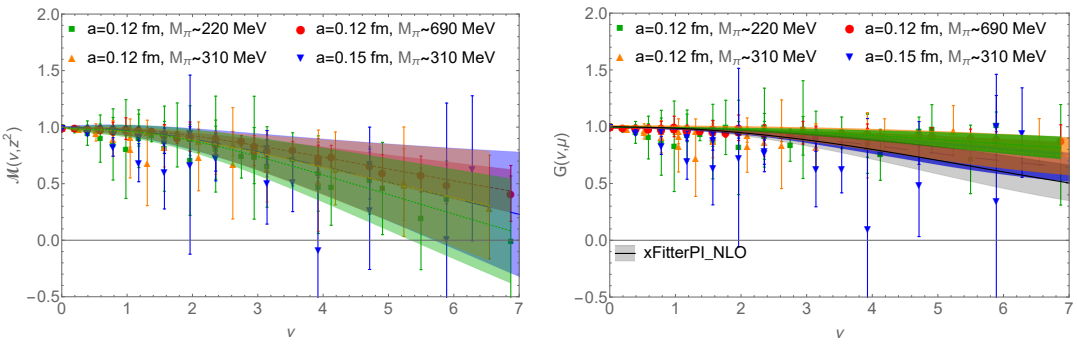

Figure 8 The RpITDs $\mathscr{M}$ with reconstructed bands from "z-expansion" fits (top) and the EpITDs G with reconstructed bands from the fits to the Eq. V.13 form (bottom) calculated on ensembles with lattice spacing $a \approx 0.12$ fm, pion masses $M_\pi \approx \{220, 310, 690\}$ MeV, and $a \approx 0.15$ fm, $M_\pi \approx 310$ MeV, noticing that $a \approx 0.12$, $M_\pi \approx 690$ MeV results are from a12m220 ensemble here.

After we have the continuous-ν fitted RpITDs, we obtain the EpITDs through Eq. IV.1. The RpITDs $\mathscr{M}$ and EpITDs G as functions of ν on all ensembles studied in this work are shown in Fig. 8. At some ν values, there are multiple z and P_z combinations for a fixed ν value.

Therefore, there are points in the same color and symbol overlapping at the same ν from the same lattice spacing and pion mass. To match with the lightcone gluon PDF through Eq. IV.2, the EpITDs $G(\nu, \mu)$ should be free of z^2 dependence. However, the EpITDs obtained from Eq. IV.1 have z^2 dependence from neglecting the gluon-in-quark contribution and higher-order terms in the matching. The EpITDs also depend on lattice-spacing a and pion-mass M_π. Recall that the RpITDs show weak dependence on lattice spacing a and pion mass M_π. We see that the effects of a and M_π dependence on the EpITDs are also not large; the EpITD results from different a, M_π are mostly consistent with each other, as shown in the second row of Fig. 8. We also observe a weak dependence on z^2 for the RpITDs and EpITDs in Fig. 8.

IV.2. Pion gluon PDF

The gluon PDF $g(x, \mu^2)$ can now be extracted from the EpITDs using Eq. IV.2. We assume a functional form, also used by JAM [4, 24], for the lightcone PDF to fit the EpITD,

$$f_g(x, \mu) = \frac{x g(x, \mu)}{\langle x \rangle_g(\mu)} = \frac{x^A (1-x)^C}{B(A+1, C+1)}, \tag{IV.8}$$

for $x \in [0, 1]$ and zero elsewhere. The beta function $B(A+1, C+1) = \int_0^1 dx\, x^A (1-x)^C$ is used to normalize the area to unity. Then, we apply the matching formula to obtain the EpITD G from the functional form PDF using Eq. IV.2. We fit the EpITDs $G(\nu, \mu)$ obtained from the parametrization to the EpITDs $G(\nu, z^2, \mu, a, M_\pi)$ from the lattice calculation. The fits are performed by minimizing the χ^2 function,

$$\chi^2_G(\mu, a, M_\pi) = \sum_\nu \frac{(G(\nu, \mu) - G(\nu, \mu, a, M_\pi))^2}{\sigma^2_G(\nu, \mu, a, M_\pi)}. \tag{IV.9}$$

We investigate the systematic uncertainty introduced by the different parametrization forms which are commonly used for $f_g(x, \mu)$ in PDF global analysis and some lattice calculations. The first one is the 2-parameter form in Eq. V.13. Second, we consider the 1-parameter form $N_1(1-x)^C$ used in xFitter's analysis [3] (also used in Ref. [51, 52]), which is equivalent to Eq. V.13 with $A = 0$. Third, we consider a 3-parameter form,

$$f_{g,3}(x, \mu) = \frac{x^A (1-x)^C (1 + D\sqrt{x})}{B(A+1, C+1) + DB(A+1+1/2, C+1)}, \tag{IV.10}$$

We fit the three different forms to the EpITDs of lattice data with $z_{\text{max}} \approx 0.6$ fm by applying

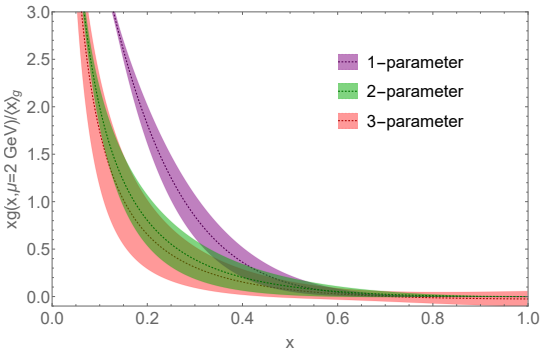

Figure 9 The $xg(x,\mu)/\langle x\rangle_g$ at $\mu^2 = 4$ GeV^2 as function of x (bottom) calculated with lattice spacing $a \approx 0.12$ fm, pion masses $M_\pi \approx 220$ MeV with the fitted bands of $z_{\text{max}} \approx 0.6$ fm from the 1-, 2- and 3-parameter fits described in Eq. V.13 and the paragraph after it.

the scheme conversion Eq. IV.2 to the 1-, 2- and 3-parameter PDF forms. Here, we focus on the result from the lightest pion mass $M_\pi \approx 220$ MeV at lattice spacing $a \approx 0.12$ fm. The χ^2/dof of the fits decreases as $1.47(72)$, $1.08(68)$, to $1.04(41)$, shows slightly better fit quality for 2- and 3-parameter fits. As shown in Fig. 9, there is a big discrepancy between the $f_g(x,\mu)$ fit bands from the 1-parameter fit and the 2-parameter fit in the $x < 0.4$ region, but the discrepancy between the 2- and 3-parameter fits is much smaller. Therefore, we conclude that 1-parameter fit on lattice data here is not quite reliable, and the fit results converge at the 2- and 3-parameter fits. The same conclusions hold for all other ensembles and pion masses. Therefore, using the 2-parameter form defined in Eq. V.13 (same parametrization as JAM) for our final results is very reasonable.

Another source of systematic uncertainty comes from neglecting the contribution of the quark term in the matching based on the assumption (motivated by global fits) that the pion $q_S(x)$ is smaller than the gluon PDF. Currently, there are no $q_S(x)$ results from lattice simulation since only the valence distribution of the pion has been done. Thus, we estimate the systematic due to omitting the $q_S(x)$ contribution by using the pion quark PDFs from xFitter [3] at NLO. Using these, we obtain revised RpITDs and EpITDs including the gluon-in-quark R_{gq} term focusing on example from the $a \approx 0.12$ fm, pion mass $M_\pi \approx 220$ MeV lattice, repeating the same procedure from Eq. IV.6 and fitting the EpITDs with Eq. V.13. On the left-hand side of Fig. 10, we show the mean value of $xg(x,\mu)/\langle x\rangle_g$ with both gluon-in-gluon (gg) and gluon-in-quark (gq) contributions (the blue solid line) compared to the a12m220 results using the gluon-in-gluon contribution only (the green solid line). There are 5 to 10% differences in the mean

value including the gluon-in-gluon contribution for $x < 0.9$, which indicates that the gluon-in-quark contribution is relatively small at $\mu^2 = 4\,\text{GeV}^2$ compared to the current statistical errors in the small-x region. In the $x > 0.9$ region, the gluon-in-quark contribution becomes more significant, but it remains smaller than the statistical error. Once studies are available with sufficiently reduced statistical uncertainty in the large-x region, the quark contribution will need to be included.

From the above analyses of the choice of fit form and the contribution of the quark term, we conclude that these systematics are negligible relative to the current statistics. Finite-volume systematics have not been taken into account in this work. However, the results of the finite-volume study on the nucleon isovector PDFs on the a12m220 ensemble with multiple lattice volumes (2.88, 3.84, 4.8 fm) suggest that the finite-volume effect is negligible at the current lattice precision [165]. This is consistent with a later study using chiral perturbation theory (ChPT), [243], also showing that momentum boost reduces the finite-volume effect, since the length contraction of the hadron makes the lattice effectively bigger. We expect the finite-volume error to be much smaller than the statistical ones. Therefore, we adopt the $z_{\text{max}} \approx 0.6$ fm ($z_{\text{max}} \approx 0.75$ fm for a15m310 ensembles) fits to the EpITDs, neglect the quark contribution term in the matching, and use the Eq. IV.2 fit form for our final results on all lattice ensembles. The $xg(x,\mu)/\langle x\rangle_g$ reconstructed fit bands of these ensembles are shown in the left plot in Fig. 10, comparing results from different lattice spacings and pion masses. The reconstructed fit bands with different pion mass $M_\pi \approx \{220, 310, 690\}$ MeV are consistent at the same lattice spacing $a \approx 0.12$ fm, indicating mild gluon PDF dependence on pion mass. Similarly, when comparing lattice-spacing dependence of pion PDFs using data around pion mass $M_\pi \approx 310$ MeV ($M_\pi \approx 690$ MeV in the inserted plot), we find that fitted PDF is slightly smaller in the $x > 0.1$ region for the 0.12-fm lattice, but still within one sigma, which indicates the lattice-spacing dependence is also mild. We also note that the bands from different ensembles show a differing speed of fall-off as $x \to 1$ in the large-x region. We study this fall-off behavior in more depth below.

The behavior of the gluon PDF fall-off in the large-x region is widely studied in both theory and global analyses. Perturbative QCD studies [244, 245] and DSE calculations [230, 25, 232] suggest that the gluon distribution $g(x,\mu^2) \sim (1-x)^C$ with $C \approx 3$ in the limit $x \to 1$. The

prediction from perturbative QCD [245] is based on the idea that the gluon PDF should be suppressed at large x relative to the quark PDF, because the quarks are the sources of large-x gluons; that is, $g(x,\mu^2)/q_v(x,\mu^2) \to 0$ as $x \to 1$. Early fits of experimental data gave $C \approx 2$ [51, 52] or $C < 2$ [5, 53], but the more recent global analysis from JAM collaboration yielded $C > 3$ [4, 24] and xFitter collaboration found $C \approx 3$ [3]. Our fitted parameter C is $3.6(1.5)$, $3.3(2.0)$, $4.7(2.8)$ for $M_\pi \approx \{690, 310, 220\}$ MeV, respectively, at lattice spacing $a \approx 0.12$ fm. These C results are consistent with each other and show a slightly increasing trend as the pion mass approaches the physical pion mass. For lattice spacings $a \approx \{0.15, 0.12\}$ fm, $C = \{2.2(1.5), 3.3(2.0)\}$, respectively, at $M_\pi \approx 310$ MeV, which suggests that C will increase toward the continuum limit. We also investigate the effect of the gluon-in-quark contribution on the C value, and it makes about 0.1 difference, which we neglect. Given that both the pion-mass and lattice-spacing extrapolations seem to show increasing C, it seems reasonable to conclude from this lattice-QCD study that $C > 3$.

We compare our reconstructed gluon PDF to those from global fits on the right-hand side of Fig. 10. It shows the $xg(x,\mu)/\langle x\rangle_g$ reconstructed fit band of $a \approx 0.12$ fm, $M_\pi \approx 220$ MeV lattice, from DSE calculation [25], and NLO pion gluon PDFs from xFitter [3] and JAM [4, 24] at $\mu^2 = 4\,\text{GeV}^2$. The JAM band appears somewhat wider than expected, because we reconstruct it by dividing $xg(x,\mu)$ by the mean value of $\langle x\rangle_g$; the correlated values needed for a correct error estimation were not available. Note that xFitter uses the fit form of Eq. V.13 with $A = 0$. Our fitted pion gluon PDF is consistent with JAM and DSE for $x > 0.2$, and with xFitter for $x > 0.5$ within one sigma. We also show $x^2 g(x,\mu)/\langle x\rangle_g$ for $x > 0.5$ region in the inserted plot on the right-hand side of Fig. 10. We see in this comparison that our results are of similar error size as the global-fit analysis and are useful to provide constraints from theoretical calculation in addition to the experimental data.

IV.3. Summary

In this work, we presented the first calculation of the pion gluon PDF from lattice QCD and studied its pion-mass and lattice-spacing dependence using the pseudo-PDF approach. We employed clover valence fermions on ensembles with $N_f = 2{+}1{+}1$ highly improved staggered quarks (HISQ) at two lattice spacings ($a \approx 0.12$ and 0.15 fm) and three pion masses (220, 310

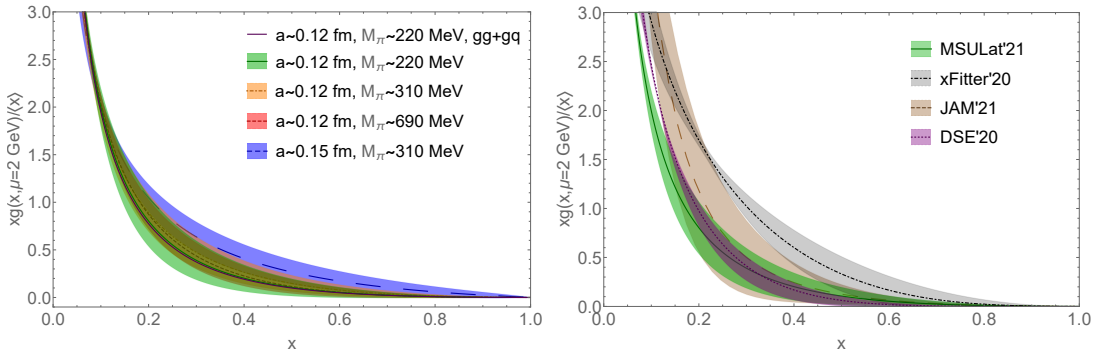

Figure 10 The pion gluon PDF $xg(x,\mu)/\langle x\rangle_g$ as a function of x obtained from the fit to the lattice data on ensembles with lattice spacing $a \approx \{0.12, 0.15\}$ fm, pion masses $M_\pi \approx \{220, 310, 690\}$ MeV (left plot and its inserted plot), and $xg(x,\mu)/\langle x\rangle_g$ ($x^2g(x,\mu)/\langle x\rangle_g$ in the inserted plot) as function of x obtained from lattices of $a \approx 0.12$ fm, $M_\pi \approx 220$ MeV (right), compared with the NLO pion gluon PDFs from xFitter'20 and JAM'21, and the pion gluon PDF from DSE'20 at $\mu = 2$ GeV in the $\overline{\text{MS}}$ scheme. The JAM'21 error shown is overestimated due to lack of available correlated uncertainties in its constituent components. Our PDF results are consistent with JAM [4, 24] and DSE [25] for $x > 0.2$, and xFitter [3] for $x > 0.5$.

and 690 MeV). These ensembles allowed us to probe the dependence of the pion gluon PDF on pion mass and lattice spacing. In both cases, the dependence appears to be weak compared to the current statistical uncertainty.

We investigated the systematics associated with the functional form used in the reconstruction fits as well as the systematics caused by neglecting the quark contribution in the matching. The effect of the assumed gluon PDF fit form was investigated by using various forms, which are all commonly used or proposed in other PDF works. We observe large effects changing the fit to $xg(x,\mu)/\langle x\rangle_g$ from 1- to 2-parameter form but convergence at 3 parameters. This implies the 2-parameter fits are sufficient for our calculation, and our finial pion gluon PDF results are presented using the 2-parameter fit results. We used the pion quark PDF from xFitter to make an estimation of the quark contribution to the pion gluon RpITD. We found the systematic errors it contributed are smaller than 10% of the statistical errors.

Our pion gluon PDF for the lightest pion mass is consistent with JAM'21 and DSE'20 for $x > 0.2$, and with xFitter'20 for $x > 0.5$ within uncertainty, as shown in our final comparison plots of the pion gluon PDF. We also studied the asymptotic behavior of the pion gluon PDF in the large-x region in terms of $(1-x)^C$. $C > 3$ is implied from our study at two lattice spacings and three pion masses. The future study of the pion gluon PDF from the lattice QCD with improved precision and systematic control when combined in global-fit analyses with the

results of anticipated experiments [216, 43, 45, 216] will provide best determination of the gluon content within the pion.

V. Nucleon gluon PDF

The unpolarized gluon parton distribution functions (PDFs) $g(x)$ and quark PDFs $q(x)$ are important inputs to many theory predictions for hadron colliders [26, 47, 15, 14, 16, 246, 247, 248]. For example, both $g(x)$ and $q(x)$ contribute to the deep inelastic scattering (DIS) cross section, and $g(x)$ enters at leading order in jet production [32, 33]. To calculate the cross section for these processes in pp collisions, $g(x)$ needs to be known precisely. Although there are experimental data like top-quark pair production, which constrains $g(x)$ in the large-x region, and charm production, which constrains $g(x)$ in the small-x region, $g(x)$ is still experimentally the least known unpolarized PDF because the gluon does not couple to electromagnetic probes. The Electron-Ion Collider (EIC), which aims to understand the role of gluons in binding quarks and gluons into nucleons and nuclei, is at least in part intended to address this gap in our experimental knowledge [42]. In addition to experimental studies, the theoretical approaches to determining gluon structure by calculation are continually improving. The recent calculations on nucleon PDFs based on quasi-PDF, pseudo-PDF, "good lattice cross sections" approaches are listed in the beginning of Chap. III

V.1. First Exploratory Study

In our first calculation of gluon quasi-PDF, we defined the gluon quasi-PDF matrix element and operator different with the LaMET operators we discussed in Sec. III.1,

$$\begin{aligned} \tilde{H}_0(z, P_z) &= \langle P|\mathcal{O}_0(z)|P\rangle, \\ \mathcal{O}_0 &\equiv \frac{P_0\left(\mathcal{O}(F^t_{\ \mu}, F^{\mu t}; z) - \frac{1}{4}g^{tt}\mathcal{O}(F^{\mu}_{\ \nu}, F^{\nu}_{\ \mu}; z)\right)}{\frac{3}{4}P_0^2 + \frac{1}{4}P_z^2}, \end{aligned} \tag{V.1}$$

renormalized at the scale μ with $\mathcal{O}(F^{\rho}_{\ \mu}, F^{\mu\tau}; z) = F^{\rho}_{\ \mu}(z)U(z,0)F^{\mu\tau}(0)$. When $z = 0$, $\tilde{H}_0(0, P_z)$ is a local operator and equals to $\langle x\rangle_g$. In the large momentum limit, only the leading twist contribution in $\tilde{g}(x)$ survives, and then $\tilde{g}(x)$ can be factorized into the the gluon PDF $g(y)$ and a perturbative calculable kernel $\mathcal{C}(x, y)$, up to mixing with the quark PDF and the higher-twist corrections $\mathcal{O}(1/P_z^2)$. This operator is later proved not multiplicatively renormalizable in Ref. [201] and not used in our following calculations.

Since the Lattice calculation of $\tilde{H}_0(z, P_z)$ is under the lattice regularization, a non-perturbative renormalization (NPR) of the glue operators $\mathcal{O}_0(z)$ is required to convert $\tilde{H}_0(z, P_z)$ into that

under the $\overline{\text{MS}}$ scheme with the perturbative matching in the continuum. This can be achieved following the glue NPR strategy introduced in Ref. [30] just recently for $\langle x \rangle_g$.

As shown in Refs. [201, 249], the $\mathcal{O}(F^z_\mu, F^{\mu z}; z)$ and $\mathcal{O}(F^\mu_\nu, F^{\nu\mu}; z)$ ($\mu, \nu \neq z$) structures in $\mathcal{O}_0$ should be renormalized separately before combined together, but its linear divergence [250, 251] is an overall multiplicative factor depending on the Wilson-link length z. For the linear divergence introduced by the Wilson link, an empirical observation in the quark unpolarized quasi-PDF case is that, the non-perturbative RI/MOM renormalization constant with $p^R_z = 0$ can be approximated by the nucleon iso-vector matrix element with $P_z = 0$ in the $z < 0.5$ fm region, with $\sim$10% deviation, while the systematic uncertainties due to the hadron IR structure is hard to estimate [200]. If the gluon case is similar, the linear divergence of the gluon quasi-PDF matrix element can be removed by defining the "ratio renormalization" (similar to the reduce Ioffe-time distribution considered in the quark case [203, 186, 208])

$$\tilde{H}^{Ra}_0(z, P_z, \mu) = \frac{\tilde{H}^{\overline{\text{MS}}}_0(0, 0, \mu)}{\tilde{H}_0(z, 0)} \tilde{H}_0(z, P_z) \tag{V.2}$$

as an approximation of the RI/MOM renormalized one, with $\tilde{H}^{Ra}_0(z, P_z, \mu) = \langle x \rangle^{\overline{\text{MS}}}_g(\mu)$.

After the renormalization, both the quark and gluon PDF contribute to the factorization of the gluon qausi-PDF [250], and the case with the gluon quasi-PDF operator defined here will be investigated in a future study. In this work, we will calculate the gluon quasi-PDF matrix element and apply the "ratio renormalization" to have a glimpse on the range of z and P_z one can reach on the lattice, and compare it with the FT of the gluon PDF.

Numerical setup: The lattice calculation is carried out with valence overlap fermions on 203 configurations of the $2 + 1$-flavor domain-wall fermion gauge ensemble "24I" [252] with $L^3 \times T = 24^3 \times 64$, $a = 0.1105(3)$ fm, and M^{sea}_π=330 MeV. For the nucleon two-point function, we calculate with the overlap fermion and loop over all timeslices with a 2-2-2 Z_3 grid source and low-mode substitution [253, 254], and set the valence-quark mass to be roughly the same as the sea and strange-quark masses (the corresponding pion masses are 340 and 678 MeV, respectively). Counting independent smeared-point sources, the statistics of the two-point functions are $203 \times 64 \times 8 \times 2 = 207,872$, where the last factor of 2 coming from the averaging between the forward and backward nucleon propagators.

On the lattice, $\mathcal{O}_0$ is defined by

$$\mathcal{O}_0 = -\frac{P_0\left(\mathcal{O}_E(F_{t\mu}, F_{\mu t}, z) - \frac{1}{4}\mathcal{O}_E(F_{\mu\nu}, F_{\nu\mu}; z)\right)}{\frac{3}{4}P_0^2 + \frac{1}{4}P_z^2} \tag{V.3}$$

where $\mathcal{O}_E(F_{\rho\mu}, F_{\mu\tau}, z) = 2\mathrm{Tr}\big[F_{\rho\mu}(z)U(z,0)F_{\mu\tau}(0)U(0,z)\big]$ is defined in the Euclidean space with the gauge link $U(z,0)$ in the fundamental representation, and the clover definition of the field tensor $F_{\mu\nu}$ is the same as that used in our previous calculation of the glue momentum fraction [30].

The choice for the quasi-PDF operator is not unique. Any operator that approaches the lightcone one in the large-momentum limit is a candidate, such as the other choices inspired by Eq. (**??**)

$$\begin{aligned}
\mathcal{O}_1(z) &\equiv \frac{1}{P_z}\mathcal{O}(F_{t\mu}, F_{z\mu}; z), \\
\mathcal{O}_2(z) &\equiv \frac{P_0\left(\mathcal{O}(F_{z\mu}, F_{\mu z}; z) - \frac{1}{4}g^{zz}\mathcal{O}(F_{\mu\nu}, F_{\nu\mu}; z)\right)}{\frac{1}{4}P_0^2 + \frac{3}{4}P_z^2},
\end{aligned} \tag{V.4}$$

as well as

$$\mathcal{O}_3(z) \equiv \frac{1}{P_0}\mathcal{O}(F_{z\mu}, F_{\mu z}; z) \tag{V.5}$$

proposed in Ref. [149]. These alternative operators $\mathcal{O}_{1,2,3}$ can be defined on the lattice similarly. As we will address in the latter part of this work, the quasi-PDF using $\mathcal{O}_{1,2,3}$ has larger higher-twist corrections and/or statistical uncertainty compared to that from using $\mathcal{O}_0$.

The bare glue matrix element $\tilde{H}_0(z, P_z)$ with the Wilson link length z and nucleon momentum $\{0, 0, P_z\}$ can be obtained from the derivative of the summed ratio following the recent high-precision calculation of nucleon matrix elements [255, 256],

$$\begin{aligned}
\tilde{R}(z, P_z; t_{\mathrm{sep}}) &= \sum_{0<t<t_{\mathrm{sep}}} R(z, P_z; t_{\mathrm{sep}}, t) \qquad - \sum_{0<t<t_{\mathrm{sep}}-1} R(z, P_z; t_{\mathrm{sep}} - 1, t) \\
&= \tilde{H}_0(z, P_z) + \mathcal{O}(e^{\Delta m t_{\mathrm{sep}}}),
\end{aligned} \tag{V.6}$$

where

$$R(z, P_z; t_{\mathrm{sep}}, t) \qquad \equiv \qquad \frac{E\langle 0|\Gamma^e \int \mathrm{d}^3y e^{-iy\cdot P}\chi(\vec{y}, t_{\mathrm{sep}})\mathcal{O}_0(z;t)\chi(\vec{0}, 0)|0\rangle}{(\frac{3}{4}E^2 + \frac{1}{4}P_z^2)\langle 0|\Gamma^e \int \mathrm{d}^3y e^{-iy_3P_3}\chi(\vec{y}, t_{\mathrm{sep}})\chi(\vec{0}, 0)|0\rangle}$$

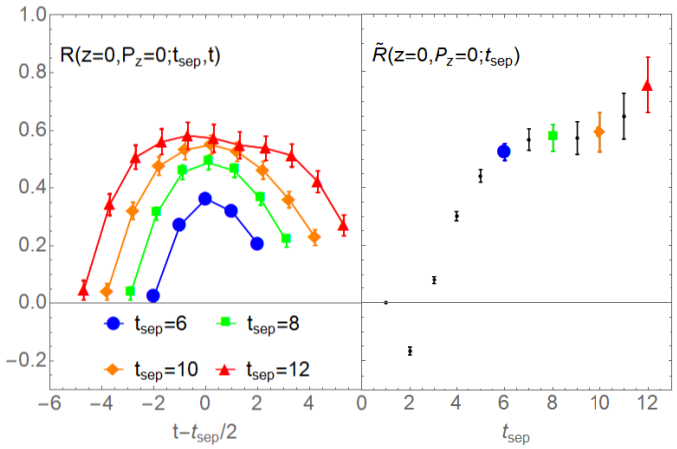

Figure 11 The ratio $R(t_{\rm sep}, t)$ for $\tilde{H}_0(0,0)$ at different $t_{\rm sep}$ as a function of operator insertion time t (left panel), and the ratio $\tilde{R}(t_{\rm sep})$ as a function of source-sink seperation $t_{\rm sep}$ (right panel). Four colored points in the right panel corresponds to the $\tilde{R}$ at the separations plotted in the left-panel.

and $\Gamma^e = \frac{1}{2}(1+\gamma_4)$. To further improve the signal of $\tilde{H}_0$, we applied up to 5 steps of HYP smearing on the glue operators.

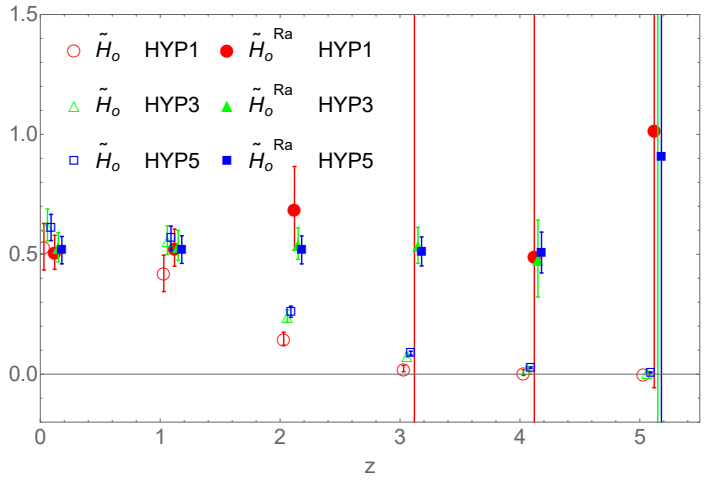

Figure 12 The bare $\tilde{H}(z, P_z = 0.46\,\text{GeV})$ and the renormalized one $\tilde{H}^{Ra}$ at 2 GeV with 1,3,5 HYP smearing steps, as functions of z. In $\tilde{H}^{Ra}$, the exponential falloff in the bare $\tilde{H}$ due to the linear divergence is removed by the "ratio renormalization factor" $Z(\mu, z) \equiv H_0^{\overline{\rm MS}}(0,0,\mu)/\tilde{H}_0(z,0)$. Some data using the same HYP smearing steps are shifted horizontally to enhance the legibility.

Results: As illustrated in Fig. 11 for $\tilde{H}_0(0,0)$ with 5 HYP smearing steps, the value of $\tilde{R}$ saturates after $t_{\rm sep} > 6$ and a constant fit can provide the same result as what can be obtained from the two-state fit of R with larger $t_{\rm sep}$. In the $t_{\rm sep} \gg t \gg 0$ limit, both $\tilde{R}$ and R saturate to the same $\tilde{H}_0(0,0) = \langle x \rangle_g^{\rm bare} = 0.55(8)$ as in the figure, while such a limit can be reached with smaller $t_{\rm sep}$ in the $\tilde{R}$ case. Using the renormalization constant of $\langle x \rangle_g$ in $\overline{\rm MS}$ at 2 GeV

with 5 steps of the HYP smearing calculated in Ref. [30] of 0.90(10) and ignoring mixing from the quark momentum fraction, the $\overline{\text{MS}}$ renormalized $\langle x \rangle_g^{\overline{\text{MS}}}(2\text{ GeV}) = \tilde{H}_0^{Ra}(0, 0, 2\text{ GeV}) = 0.50(7)(5)$ agrees with the phenomenological determination 0.42(2) [26] within uncertainties.

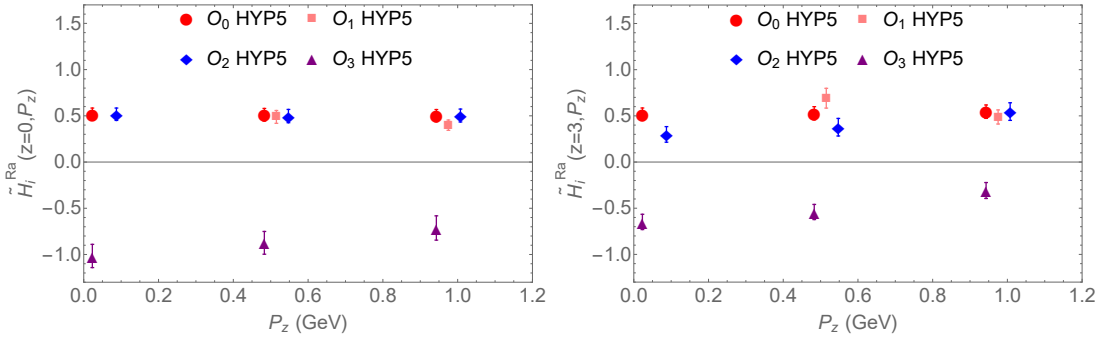

Figure 13 The renormalized $\tilde{H}^{Ra}_{i=0,1,2,3}(z, P_z)$ as a functions of P_z at z=0 (top) and 3 (bottom). Some data with the same P_z are shifted horizontally to enhance the legibility. The case with $\mathcal{O}_{i=3}$ suffers from a large contamination from higher-twist distributions, while the results with $\mathcal{O}_{i=0,1,2}$ are consistent with each other, especially at larger P_z.

Due to its linear divergence [251], the bare $\tilde{H}_0(z, P_z)$ decays exponentially as $|z|$ increases. Fig. 12 shows the z dependence of $\tilde{H}_0(z, P_z)$ with $P_z = 0.46$ GeV and 1, 3 and 5 HYP smearing steps. It is obvious to see that the decay rates decreases when more steps of smearing are applied, since the corresponding linear divergence becomes smaller. Note that $\tilde{H}_0(z, P_z)$ is purely real and symmetric with respect to z; thus, we just plot the real part in the positive-z region. The "ratio renormalized" matrix elements $\tilde{H}_0^{Ra}(z, P_z)$ with different HYP smearing steps are consistent with each other, as shown in Fig. 12, while more HYP smearing can reduce the statistical uncertainties significantly.

Then, we plot the "ratio renormalized" $\tilde{H}^{Ra}_{i=0,1,2,3}(z = 0, P_z)$ using $Z(\mu, z) \equiv \frac{\tilde{H}_0^{\overline{\text{MS}}}(0,0,\mu)}{\tilde{H}_0(0,0,\mu)}$ for the glue operator $\mathcal{O}_i$ with 5 HYP smearing steps and $P_z = 0.0$, 0.46, 0.92 GeV in the top panel of Fig. 13. All the cases with $\mathcal{O}_{i=0,1,2}$ provide consistent results, except $\mathcal{O}_3$ which suffers from large mixing with the higher-twist operator $\mathcal{O}(F^\mu_\nu, F^\nu_\mu; z)$. With larger P_z, the value of $\tilde{H}_3^{Ra}(0, P_z)$ becomes less negative as higher-twist contamination becomes smaller.

The lower panel of Fig. 13 shows $\tilde{H}^{Ra}_{i=0,1,2,3}(z = 3, P_z)$ with different operators and $P_z = 0.0$, 0.46, 0.92 GeV. The $\mathcal{O}_3$ case also suffers from large higher-twist contamination like the $z = 0$ case; the results with $\mathcal{O}_{i=0,1,2}$ seem to be slightly different from each other at $P_z = 0.46$ GeV, while the consistency at $P_z = 0.92$ GeV is much better. Since the operators $O_{0,1,2}$ can provide consistent results but the uncertainty using O_0 is slightly smaller than the other two

cases, we will concentrate on this case in the following discussion.

Finally, the coordinate-space gluon quasi-PDF matrix element ratios $\tilde{H}_0^{Ra}(z, P_z)$ are plotted in Fig. 14, compared with the corresponding FT of the gluon PDF, H(z, μ=2 GeV), based on the global fits from CT14 [26] and PDF4LHC15 NNLO [27]. Since the uncertainties increases exponentially at larger z, our present lattice data with good signals are limited to the range zP_z <2 or so, and the values at different zP_z are consistent with each other. At the same time, $H(z, 2\text{ GeV})$ doesn't changes much either in this region as in Fig. 14, as investigated in Ref. [208]. Up to perturbative matching and power correction at $\mathcal{O}(1/P_z^2)$, they should be the same, and our simulation results are within the statistical uncertainty at large z. The results at the lighter pion mass (at the unitary point) of 340 MeV is also shown in Fig. 14, which is consistent with those from the strange quark mass case but with larger uncertainties. We also study the pion gluon quasi-PDF (see Fig. 15) and similar features are observed.

In a recent work [257] involving part of the present authors, the glue momentum fraction $\langle x \rangle^{\overline{\text{MS}}}$ (corresponds to $\tilde{H}^{Ra}(0)$ here) is calculated on configurations with different lattice spacing, valence and sea quark masses. The value of $\langle x \rangle^{\overline{\text{MS}}}$ tend to be slightly larger with smaller quark mass, but the dependence is weak. Thus it hints that the entire gluon distribution may be also insensitive to either the valence or sea quark mass given the current statistical errors, up to $\sim$ 400 MeV pion mass or so. The quark case is similar; thus we don't expect the gluon quasi-PDF and the mixing with the quark PDF through the factorization to be very sensitive to the quark mass unless the statistical uncertainty can be reduced significantly.

If $\tilde{H}_0^{Ra}(z, P_z)$ keeps flat outside the region where we have good signal, the gluon quasi-PDF $\tilde{g}(x)$ will be a delta function at $x = 0$ through FT. On the other hand, the width of $\tilde{g}(x)$ will be ~ 0.5 in x if we suppose $\tilde{H}_0^{Ra}(z, P_z) = 0$ for all the zP_z >3. We conclude the FT of our present results of $\tilde{H}_0^{Ra}(z, P_z)$ cannot provide any meaningful constraint on the gluon PDF $g(x)$.

Summary and outlook: In summary, we present the first gluon quasi-PDF result for the nucleon and pion with multiple hadron boost momenta P_z and explore different choices of the operators. With proper renormalization, the quasi-PDF matrix elements we obtain agree with the FT of the global-fit PDF within statistical uncertainty, up to mixing from the quark PDF, perturbative matching and higher-twist correction $\mathcal{O}(1/P_z^2)$.

Since global fitting results shows that most of the contribution of $g(x)$ comes from the

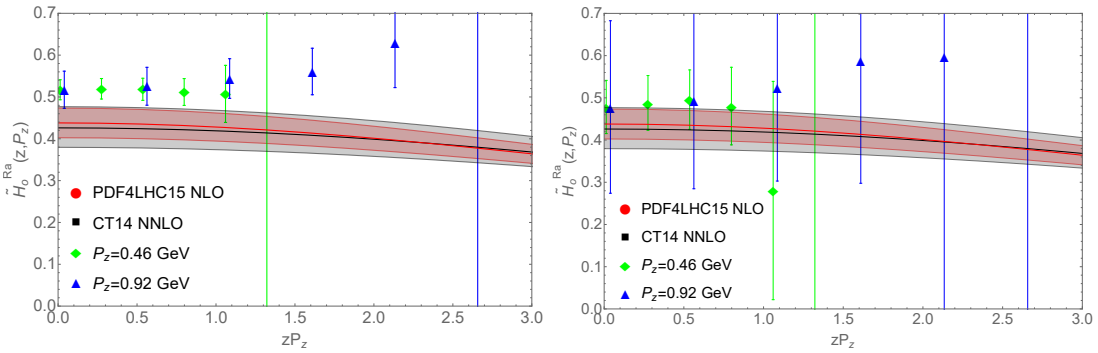

Figure 14 The final results of $\tilde{H}_0^{Ra}(z, P_z)$ at 678 MeV (top) and 340 MeV (bottom) pion mass as a functions of zP_z, in comparison with the FT of the gluon PDF from the global fits CT14 [26] and PDF4LHC15 NNLO [27]. The data with $P_z = 0.92$ GeV are shifted horizontally to enhance the legibility. They are consistent with each other within the uncertainty.

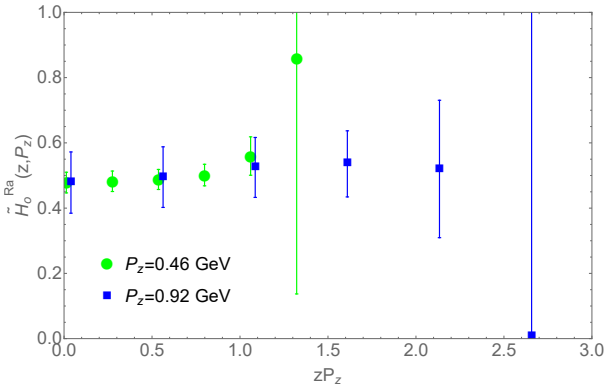

Figure 15 The similar figure for the pion gluon quasi-PDF matrix elements with $M_\pi = 678$ MeV. The shape is quite similar to the case in Fig. 14.

$x < 0.1$ region, the width of its FT, $H(zP_z)$, is pretty large as the $H(zP_z)$ becomes half of of its maximum value (at zP_z=0) at $zP_z \sim 7$. At the same time, the signal of the lattice simulation and also the validity of the factorization limit us to the small z region. Thus to discern the width of gluon PDF, the lattice simulation with much larger nucleon momentum P_z, such as 2-3 GeV, is needed. To archive a good signal with such a large P_z, the momentum smearing [107] and cluster decomposition error reduction [258] should be helpful.

In the theoretical side, the gluon quasi-PDF operator can be renormalized non-perturbatively in the RI/MOM scheme (the $\mathcal{O}(F^z_\mu, F^{\mu z}; z)$ and $\mathcal{O}(F^\mu_\nu, F^{\nu\mu}; z)$ ($\mu, \nu \neq z$) structures in $\mathcal{O}_0$ and $\mathcal{O}_2$ should be renormalized separately before combined together, while $\mathcal{O}_1$ is multiplicative renormalizable [201, 249]) based on the NPR strategy introduced in Ref. [30], and the matching to the gluon PDF can be calculated perturbatively following the framework used in the quark case [199].

V.2. First Pseudo-PDF Study

We later presented the first lattice-QCD results that access the x-dependence of the gluon unpolarized PDF of the nucleon via pseudo-PDF approach. This calculation is carried out using the $N_f = 2 + 1 + 1$ highly improved staggered quarks (HISQ) [71] lattices generated by the MILC collaboration [64] with spacetime dimensions $L^3 \times T = 24^3 \times 64$, lattice spacing $a = 0.1207(11)$ fm, and $M_\pi^{\text{sea}} \approx 310$ MeV. We apply 1 step of hypercubic (HYP) smearing [89] to reduce short-distance noise. The Wilson-clover fermions are used in the valence sector where the valence-quark masses is tuned to reproduce the lightest light and strange sea pseudoscalar meson masses (which correspond to pion masses 310 and 690 MeV, respectively), as done by PNDME collaboration [237, 238, 239, 240]. As demonstrated by PNDME and through our own calculation, we do not observe any exceptional configurations in our calculations caused by the mixed-action setup. Since our strange and light pion masses are tuned to match the corresponding sea values, we do not anticipate lattice artifacts other than potential $O(a)$ effects. Since this is at the same level as typical corrections to LaMET-type operators [259], it requires no special treatment. Such effects will be studied in future work.

We use Gaussian momentum smearing [107] is used for the quark field,

$$S_{\text{mom}}\Psi(x) = \frac{1}{1+6\alpha}\big(\Psi(x) + \alpha \sum_j U_j(x) e^{ik\hat{e}_j}\Psi(x+\hat{e}_j)\big), \tag{V.7}$$

where k is the momentum-smearing parameter and α is the Gaussian smearing parameter. In our calculation, we choose $k = 2.9$, $\alpha = 3$ with 60 iterations to help us getting a better signal at a higher boost nucleon momentum. These parameters are chosen after carefully scanning a wide parameter space to best overlap with our desired boost momenta. We use 898 lattices in total and calculate 32 sources per configuration for a total 28,735 measurements. In the previous gluon-PDF work [163], the nucleon two-point function was calculated with overlap fermions using all timeslices with a 2-2-2 Z^3 grid source and low-mode substitution [253, 254], which has 8 times more statistics and best signal at zero nucleon momentum. Even though the number of measurements in this work is smaller than the previous work, we see significant improvement in the signal-to-noise at large boost momenta with our momentum smearing, which allow us to extend our calculation to momenta as high as 2.16 GeV. We studied the $(ap)^n$ discretization effects on the nucleon two-point correlators using ensembles of different lattice spacing $a \approx 0.6, 0.9, 0.12$ fm, and the results indicate that these effects are not significant on the two-point correlators. We anticipate the discretization effects to be small in our calculation, based on the observation in the two-point correlators; a study using multiple lattice spacings for the gluon three-point correlators will be needed for future precision calculations.

The nucleons two-point correlators are then fitted to a two-state ansatz same as what we did in the pion gluon PDF Chapter IV. In this work, we use N_s to denote a nucleon composed of quarks such that $M_\pi \approx 690$ MeV and N_l to denote a nucleon composed of quarks such that $M_\pi \approx 310$ MeV. Figure 16 shows the effective-mass plots for the nucleon two-point functions with $P_z = [0, 5]\frac{2\pi}{L}$ for both masses. The bands show the corresponding reconstructed fits using Eq. 1 with fit range $[3, 13]$. The bands are consistent with the data except where P_z and t are both large. The error of the effective masses at large P_z and t region is too large to fit. However, our reconstructed effective mass bands still match the the data points for the smaller t values even for the largest $P_z = 5 \times 2\pi/L$. We check the dispersion-relation $E^2 = E_0^2 + c^2 P_z^2$ of the nucleon energy as a function of the momentum, as shown in Fig. 17, and the speed of light c for the light quark is consistent with 1 within the statistical errors.

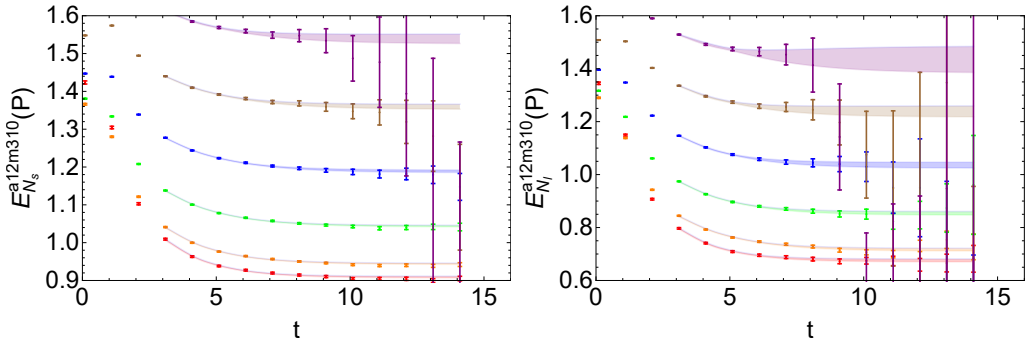

Figure 16 Nucleon effective-mass plots for $M_\pi \approx 690$ MeV (left) and $M_\pi \approx 310$ MeV (right) at $z = 0$, $P_z = [0, 5] \times \frac{2\pi}{L}$ on the a12m310 ensemble. The bands are reconstructed from the two-state fitted parameters of two-point correlators. The momentum $P_z = 5\frac{2\pi}{L}$ is the largest momentum we used, and it is the noisiest data set.

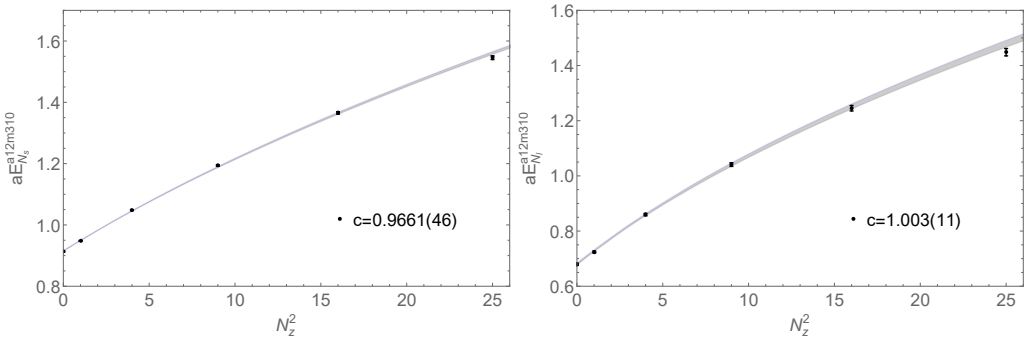

Figure 17 Dispersion relations of the nucleon energy from the two-state fits for $M_\pi \approx 690$ MeV (left) and $M_\pi \approx 310$ MeV (right)

We use the unpolarized gluon operator defined in Eq. V.26. We find the bare matrix elements to be consistent with up to 5 HYP-smearing steps, and the signal-to-noise ratios do not improve much with more steps. For the gluon operator used in this paper, we use 4 HYP smearing steps to reduce the statistical uncertainties, as studied in Ref. [163]. The matrix elements of gluon operators can be obtained by fitting the three-point function to its energy-eigenstate expansion same as we introduced in Chap. IV. Figure 18 shows example correlator plots from the ratio $R_N(P_z, t, t_{\text{sep}})$ as a function of the $t - t_{\text{sep}}/2$ for multiple source-sink separations for at $P_z = 2 \times 2\pi/L$ and $t_{\text{sep}} = \{6, 7, 8, 9\} \times a$. The reconstructed ratio plot, using the fitted parameters obtained from Eqs. (V.9) and (1) are plotted for each t_{sep}, and the gray band indicates the reconstructed ground-state matrix elements $\langle 0|\mathcal{O}_g|0\rangle$. The left-two plots in Fig. 18 show the two-simRR fits and two-sim fits using the $t_{\text{sep}} = \{6, 7, 8, 9\}a$, while the remaining two plots show individual two-state fits to the smallest and largest source-sink separations ($t_{\text{sep}} = \{6, 9\}a$). The plots of pion mass $M_\pi \approx 690$ MeV and $M_\pi \approx 310$ MeV are shown in the first row and second row respectively. The reconstructed ground state matrix elements (gray bands) for O_g are consistent for the fits with individual $t_{\text{sep}} = \{6, 9\}$, the two-sim fit results and the two-simRR fit within one sigma error. Therefore, the two-sim fits describe data from $t_{\text{sep}} = \{6, 7, 8, 9\}$ well for operator O_g. Thus, we use the two-sim fits to extract the ground-state matrix element $\langle 0|O_g|0\rangle$ of different z, P_z for the rest of this paper.

Our extracted bare ground-state matrix elements are stable across various fit ranges. Figure 19 shows example results from $M_\pi \approx 690$ MeV and $M_\pi \approx 310$ MeV nucleons with nucleon momentum $P_z \in [1, 5] \times 2\pi/L$ as the fit ranges for two- and three-point varies. In this case, the two-point correlator fit ranges are $[t_{\text{min}}, 13]$ and the three-point correlators fit ranges are $[t_{\text{skip}}, t_{\text{sep}} - t_{\text{skip}}]$. All the matrix elements from different fit ranges are consistent with each other in one-sigma error. The fit range choice $t^{\text{3pt}}_{\text{skip}} = 1$, $t^{\text{2pt}}_{\text{min}} = 2$ are not used, because the χ^2/dof of the 2-point correlator fits with $t^{\text{2pt}}_{\text{min}} = 2$ are much larger than the $t^{\text{2pt}}_{\text{min}} = 3$ cases. For the rest of this paper, we use the fitted matrix elements obtained from the fit-range choice $t^{\text{3pt}}_{\text{skip}} = 1$, $t^{\text{2pt}}_{\text{min}} = 3$. The extracted bare matrix elements are fitted for $P_z \in [0, 5] \times 2\pi/L$ and $z \in [0, 5] \times a$ to obtain the Ioffe-time distributions in pseudo-PDF calculation.

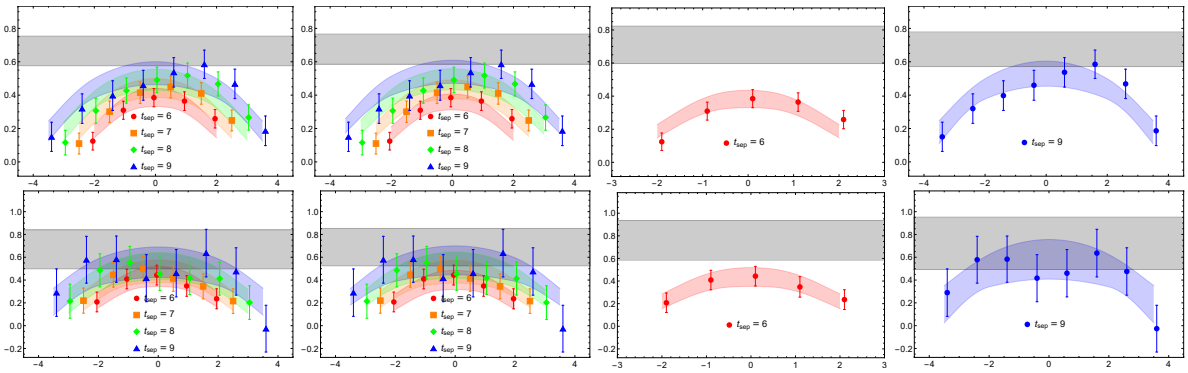

Figure 18 The three-point ratio plots for $M_\pi \approx 690$ MeV (top row) and $M_\pi \approx 310$ MeV (bottom row)nucleons $z = 1$ as functions of $t - t_{\text{sep}}/2$, as defined in Eq. IV.5. The results for nucleon momentum $P_z = 2 \times 2\pi/L$ are shown. The gray bands in each panel indicate the extracted ground-state matrix elements of the operator O_g. In each column, the plots show the fitted ratio and the extracted ground-state matrix elements from two-simRR and two-sim fits with all 4 source-sink separations, and the two-state fits using only the smallest and largest t_{sep} from left to right, respectively. The second column, which are the two-sim extracted ground-state matrix elements, are used in the subsequent analysis. The ground-state matrix elements extracted are stable and consistent among different fitting methods and three-point data input used.

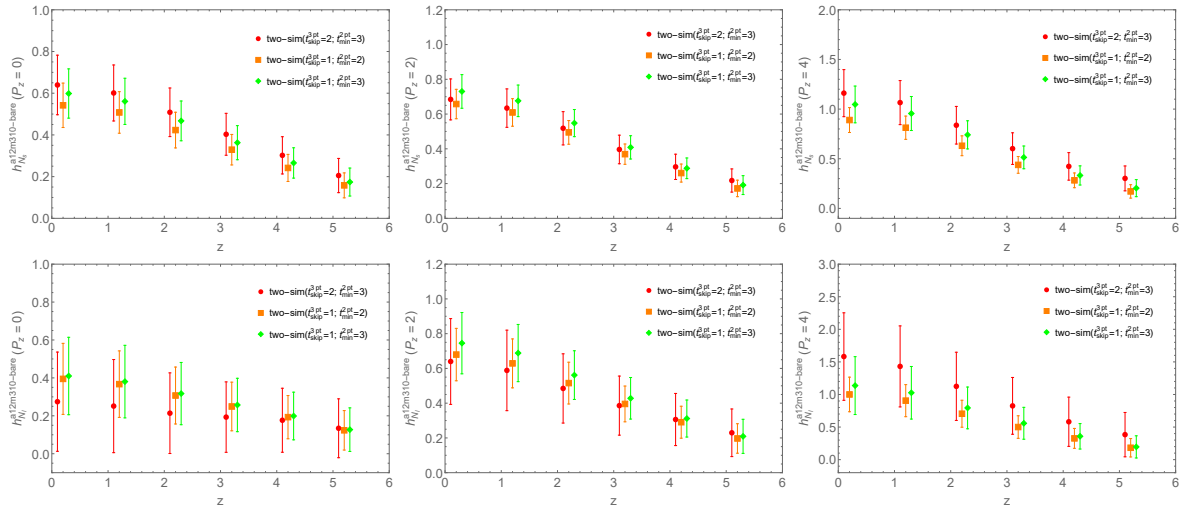

Figure 19 The fitted bare ground-state matrix elements without normalization by kinematic factors as functions of z obtained from the two-sim fit using different two- and three-point fit ranges for nucleon momentum $P_z \in \{0, 2, 4\} \times 2\pi/L$ from left to right, respectively, for $M_\pi \approx 690$ MeV (first row) and $M_\pi \approx 310$ MeV (second row) nucleons. The green points, which represent the fit-range choice $t^{\text{3pt}}_{\text{skip}} = 1$, $t^{\text{2pt}}_{\text{min}} = 3$ are used in the following analysis, because the errors of the matrix elements of this fit range are relatively smaller than the error of the red points. The orange points, which represent the fit-range choice $t^{\text{3pt}}_{\text{skip}} = 1$, $t^{\text{2pt}}_{\text{min}} = 2$, are not used because the χ^2/dof of the 2-point correlator fits with $t^{\text{2pt}}_{\text{min}} = 2$ are much larger than $t^{\text{2pt}}_{\text{min}} = 3$ cases.

V.2.1. Results and Discussions

We fit the reduced ITDs for each jackknife sample at each P_z and z value. The slope K is about -0.05 GeV^{-2} in our fit. Then, the jackknife samples of the reduced ITDs at physical pion mass are reconstructed from the fit parameters from each jackknife sample fit. Figure 20 shows the extrapolation results for the reduced ITDs at $P_z \in \{1, 5\} \times 2\pi/L$.

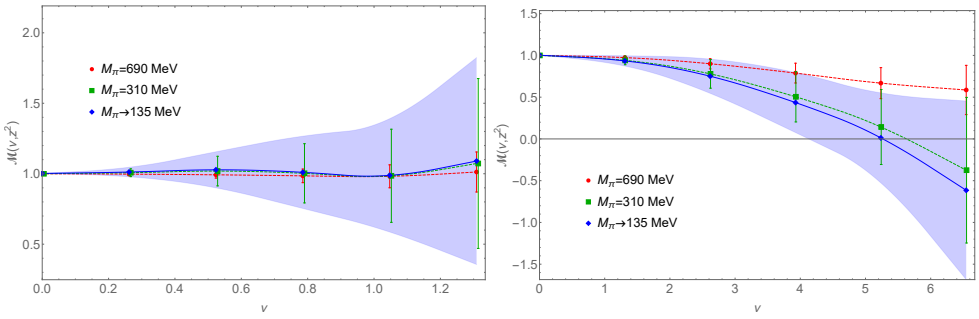

Figure 20 The reduced ITDs $\mathcal{M}(\nu, z^2)$ as functions of ν and their extrapolation to the physical pion mass at $P_z = 1 \times 2\pi/L$ (left) and $P_z = 5 \times 2\pi/L$ (right). The blue bands represent the fitted results of the reduced ITDs at the physical pion mass $M_\pi = 135$ MeV.

As shown in Fig. 21, the reduced ITDs of different z^2 from our lattice calculation show very little z dependence, because the z dependence cancels out when dividing out the ITD at $P = 0$ in the ratio defining the reduced ITD. Our fitted bands from the z-expansion fit match the reduced ITDs at different pion masses within the error bands. In Fig. 21, we can see that the fitted bands are mostly controlled by the small-z reduced ITDs, because the error grows significantly with increasing z. The reduced ITDs at physical pion mass are extrapolated from the pion masses at $M_\pi = 690$ and 310 MeV and are closer to the smaller pion mass at $M_\pi = 310$ MeV. As ν grows, the reduced ITDs decrease from $\mathcal{M}(0, z^2) = 1$. The decrease becomes faster when we go to smaller pion masses, but this trend is slight because the pion-mass dependence is weak in our case, as seen in Fig. 21, where the data and the fitted bands from 3 different pion masses are consistent within one sigma error.

The evolved ITDs at $M_\pi = 690$, 310 and extrapolated 135 MeV are obtained from Eq. IV.1. In the evolution, we choose $\mu = 2$ GeV and $\alpha_s(2\,\text{GeV}) = 0.304$. The z dependence of the evolved ITDs should be compensated by the $\ln z^2$ term in the evolution formula, which is confirmed in our evolution results. The evolved ITDs from different $z \in [1, 5] \times a$ are shown in Fig. 22 as points with different colors and are consistent with each other within one sigma error. Similar to the reduced ITDs, the evolved ITDs show small pion-mass dependence, because the

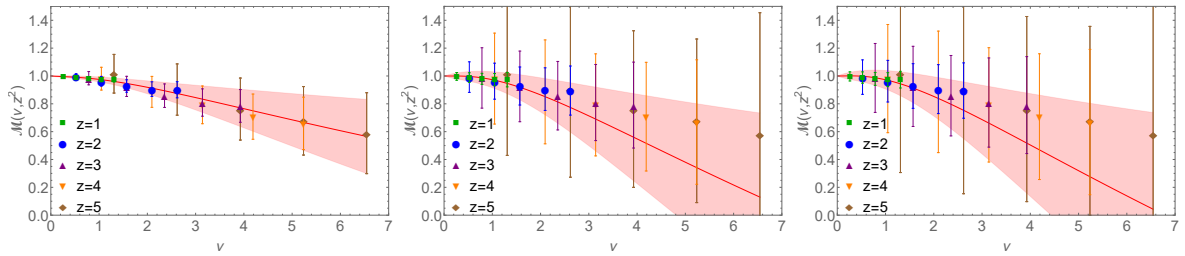

Figure 21 The reduced ITDs $\mathscr{M}(\nu, z^2)$ as functions of ν at pion masses $M_\pi = 690$, 310 and extrapolated 135 MeV from left to right, respectively. The points of different colors represent the reduced ITDs $\mathscr{M}(\nu, z^2)$ of different z^2 and the red band represents the z-expansion fit band.

data points from 3 different pion mass are consistent within one sigma error. According to the evolution function in Eq. IV.1, we can obtain the evolved ITD G by adding the reduced ITD $\mathscr{M}$ and an integral term related to $\mathscr{M}$. Due to the cancellation between the two terms, this can reduce the error in the evolved ITDs. This phenomenon is also seen in other pseudo-PDF calculations [190, 12].

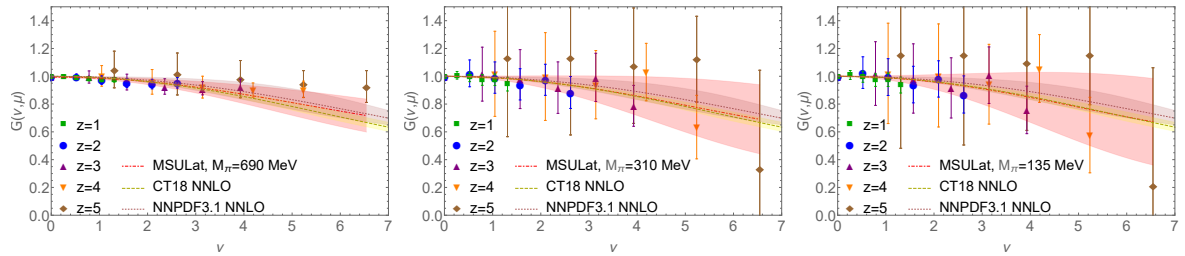

Figure 22 The evolved ITDs G as functions of ν at pion masses $M_\pi \approx 690$, 310 and extrapolated 135 MeV from left to right, respectively. The points of different colors represent the evolved ITDs $G(\nu, z^2)$ of different z values. The red band represents the fitted band of evolved ITD matched from the functional form PDF using the matching formula Eq. V.12. The yellow and pink bands represent the evolved ITD matched from the CT18 NNLO and NNPDF3.1 NNLO unpolarized gluon PDF, respectively. The evolution and matching are both performed at $\mu = 2$ GeV in the $\overline{\text{MS}}$ scheme.

The fit is performed on the evolved ITDs for $M_\pi = 690$, 310 and extrapolated 135 MeV separately. The fitted evolved ITD represented by the red band shows a decreasing trend as ν increases. The fit results for three pion masses are consistent with each other, as well as the evolved ITD from CT18 NNLO and NNPDF3.1 NNLO gluon unpolarized PDF, within one sigma error. However, the rate at which it decreases for smaller pion mass is slightly faster. The fit parameters and the goodness of the fit, χ^2/dof, are summarized in Table 2. From the functional form, it is obvious that parameter A constrains the small-x behaviour and parameter C constrains the large-x behaviour. However, the small-x results obtained from the lattice

calculation are not reliable. This is because the Fourier transform of the Ioffe time ν is related to the region around the inverse of the x and the large-ν results of evolved ITDs as shown in Fig. 22 have large error, which leads to poor constraint on the small-x behaviour of $xg(x,\mu)$. In contrast, the large-x behaviour of $xg(x,\mu)$ is constrained well because of the small error in the evolved ITDs in the small-ν region. Therefore, we have a plot that specifically shows the large-x region of $x^2g(x,\mu)$ in Fig. 23.

M_π (MeV)	A	C	χ^2/dof
690	$-0.622(14)$	$2.5(13)$	$0.35(45)$
310	$-0.611(8)$	$2.3(23)$	$0.19(36)$
135 (extrapolated)	$-0.611(9)$	$2.2(24)$	$0.19(38)$

Table 2 Our gluon PDF fit parameters, A and C, from Eq. V.13, and goodness of the fit, χ^2/dof, for calculations at two valence pion masses and the extrapolated physical pion mass.

A comparison of our unpolarized gluon PDF with CT18 NNLO and NNPDF3.1 NNLO at $\mu = 2$ GeV in the $\overline{\text{MS}}$ scheme is shown in Fig. 23. We compare our $xg(x,\mu)/\langle x_g\rangle_{\mu^2}$ with the phenomenological curves in the left panel. The middle panel shows the same comparison for $xg(x,\mu)$. Our $xg(x,\mu)$ extrapolated to the physical pion mass $M_\pi = 135$ MeV is close to the 310-MeV results and there is only mild pion-mass dependence compared with the 690-MeV results. We found that our gluon PDF is consistent with the one from CT18 NNLO and NNPDF3.1 NNLO within one sigma in the $x > 0.3$ region. However, in the small-x region ($x < 0.3$), there is a strong deviation between our lattice results and the global fits. This is likely due to the fact that the largest ν used in this calculation is less than 7, and the errors in large-ν data increase quickly as ν increases. To better see the large-x behavior, we multiply an additional x factor into the fitted $xg(x,\mu)$ and zoom into the range $x \in [0.5, 1]$ in the rightmost plot of Fig. 23. Our large-x results are consistent with global fits over $x \in [0.5, 1]$ though with larger errorbars, except for $x \in [0.9, 1]$ where our error is smaller than NNPDF, likely due to using fewer parameters in the fit. With improved calculation and systematics in the future, lattice gluon PDFs can show promising results.

To demonstrate the influence of the large-ν data on the fit results, we perform fits to the evolved ITDs with ν_{max} of 3 and 4, comparing with the original fits with $\nu_{\text{max}} = 6.54$. The fits with the ν_{max} cutoff are implemented on the lattice-calculated evolved ITDs and the evolved ITDs created by matching the CT18 NNLO gluon PDF. We show the evolved ITDs from the

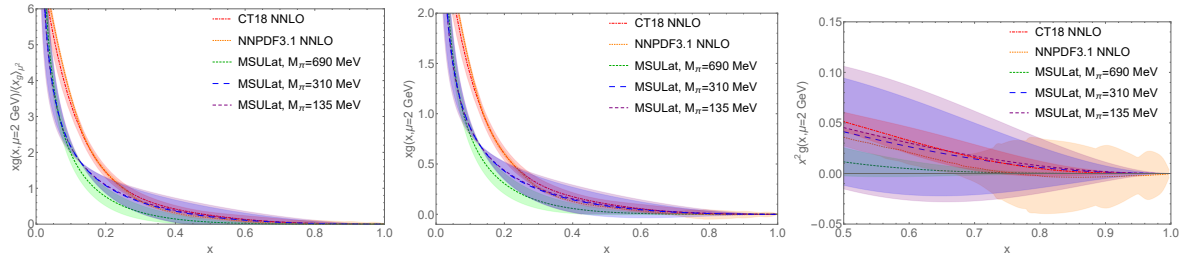

Figure 23 The unpolarized gluon PDF, $xg(x,\mu)/\langle x_g\rangle_{\mu^2}$ (left), $xg(x,\mu)$ (middle), $x^2g(x,\mu)$ in the large-x region as a function of x (right), obtained from the fit to the lattice data at pion masses $M_\pi = 135$ (extrapolated), 310 and 690 MeV compared with the CT18 NNLO (red band with dot-dashed line) and NNPDF3.1 NNLO (orange band with solid line) gluon PDFs. Our $x > 0.3$ PDF results are consistent with the CT18 NNLO and NNPDF3.1 NNLO unpolarized gluon PDFs at $\mu = 2$ GeV in the $\overline{\text{MS}}$ scheme.

$M_\pi = 310$ MeV lattice data and the fitted bands on the left-hand side of Fig. 24. The errors of the fit bands become smaller as larger-ν_{max} data are included even though the errors in the input points increases. As a result, we can see in the middle of Fig. 24 that the lattice gluon PDF errors shrink when the large-ν data help to constrain the fit.

Since our ability to accurately determine the PDFs in the small-x region is limited by the ν_{max} calculated on the lattice, we study the effect of the ν cutoff on our obtained x-dependent gluon PDF. To do so, we took the CT18 NNLO gluon PDF to construct a set of evolved ITDs using the same cutoffs $\nu_{\text{max}} = \{3, 4, 6.54\}$ used on the 310-MeV PDF. The right-hand side of Fig. 24 shows that when ν_{max} increases, the region the reconstructed PDF can recover extends to smaller x. Based on this observation, we estimate that with $\nu_{\text{max}} = 6.54$, the smallest x at which our lattice PDF can be trusted is around 0.25. We use the difference between the original CT18 input and the one reconstructed with a ν cutoff to estimate the systematic due to this cutoff effect on the higher moments.

We summarize our predictions for the second and third moments $\langle x_g^2\rangle_{\mu^2}$ and $\langle x_g^3\rangle_{\mu^2}$ at $\mu = 2$ GeV with their statistical and systematic errors in Table 3, together with the ones from CT18 NNLO and NNPDF3.1 NNLO results. The first error on our number corresponds to the statistical errors from the calculation, while the second error comes from combining in quadrature the systematic errors from four different sources: 1) The normalization of the global-PDF determination of the moment used in our calculation; 2) The finite-ν cutoff in the evolved ITDs, as discussed above. 3) The choice of strong coupling constant. To estimate this error, we vary α_s by 10%. Like previous pseudo-PDF studies [191], we find that the changes are no more

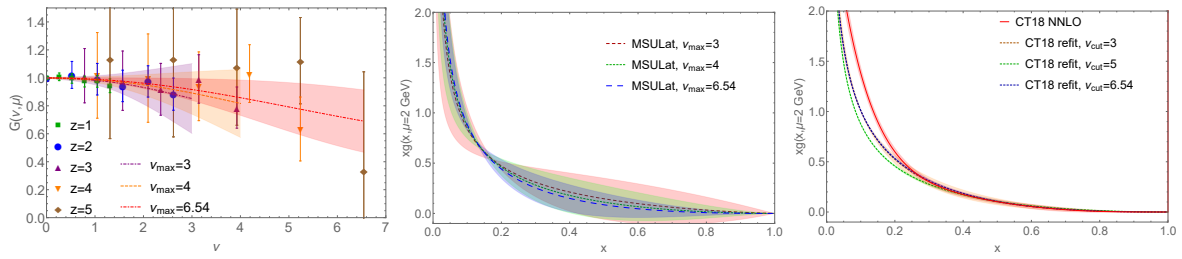

Figure 24 Left: The evolved ITDs G as functions of ν at $M_\pi \approx 310$ MeV with fits performed using different ν_{max} cutoff in the evolved ITDs. As we can see from the tightening of the fit band, the evolved ITDs at larger ν are still useful in constraining the fit despite their larger errors. Middle: The unpolarized gluon PDF obtained from the fits to the evolved ITDs at 310-MeV pion mass with different ν_{max}. The evolution and matching are both performed at $\mu = 2$ GeV in the $\overline{\text{MS}}$ scheme. The larger the ν input, the more precise the PDF obtained. Right: The 2-GeV $\overline{\text{MS}}$ renormalized unpolarized gluon PDF obtained from a fit to the evolved ITDs generated from the CT18 NNLO PDF with $\nu_{\text{max}} \in \{3, 5, 6.54\}$, compared with the original CT18 NNLO unpolarized gluon PDFs. As ν increases, we can see the gluon PDF is better reproduced toward small x. Using this exercise, we can see that our lattice PDF is only reliable in the $x > 0.25$ region. By taking the moments obtained from CT18 with a cutoff of $\nu_{\text{max}} = 6.54$ compared to those from the original PDF, we can estimate the higher-moment systematics in our lattice calculation.

than 5%; 4) The mixing with the quark singlet sector. We implement the gluon pseudo-PDF full matching kernel including the quark mixing term on CT18 NNLO unpolarized gluon PDF. The contribution of quark is about 4%, which is smaller than systematic errors from other sources. A more precise study of the effects of quark mixing on the unpolarized gluon PDF can be done when we have better control of statistical errors and other systematic errors. Overall, our moments are in agreement with the global-fit results. Future work including lighter pion masses and finer lattice-spacing ensembles will further help us reduce the systematics in the calculation.

moment	MSULat (690 MeV)	MSULat (310 MeV)	MSULat (135 MeV)	CT18	NNPDF3.1
$\langle x_g^2 \rangle_{\mu^2}$	0.040(15)(3)	0.043(26)(4)	0.045(30)(4)	0.0552(76)	0.048(13)
$\langle x_g^3 \rangle_{\mu^2}$	0.011(6)(2)	0.013(14)(3)	0.014(17)(3)	0.0154(37)	0.011(9)

Table 3 Predictions for the higher gluon moments from this work at pion mass for about 690 MeV, 310 MeV, and the extrapolated 135 MeV. The moments predictions are compared with the corresponding ones obtained from CT18 NNLO and NNPDF3.1 NNLO global fits. The first error in our number corresponds to the statistical errors from the calculation and the second errors are the systematic errors.

V.2.2. Summary and Outlook

In this paper, we present the first lattice calculation of the gluon parton distribution function using the pseudo-PDF method. The current calculation is only done on one ensemble with lattice spacing of 0.12 fm and two valence-quark masses, corresponding to pion masses around 310 and 690 MeV. In contrast to the prior lattice gluon calculation [163], we now use an improved gluon operator that is proved to be multiplicatively renormalizable. The gluon nucleon matrix elements were obtained using two-state fits. The use of the improved sources in the nucleon two-point correlators allowed us to reach higher nucleon boost momentum. As a result, we were able to attempt to extract the gluon PDF as a function of Bjorken-x for the first time. There are systematics yet to be studied in this work. Future work is planned to study additional ensembles at different lattice spacings so that we can include the lattice-discretization systematics. Lighter quark masses should be used to control the chiral extrapolation to obtain more reliable results at physical pion mass.

V.3. Updated Pseudo-PDF Study

We present the x-dependent nucleon distribution from lattice QCD using the pseudo-PDF approach, on lattice ensembles with $2+1+1$ flavors of highly improved staggered quarks (HISQ), generated by MILC Collaboration. We use clover fermions for the valence action and momentum smearing to achieve pion boost momentum up to 2.56 GeV on three lattice spacings $a \approx 0.9, 0.12$ and 0.15 fm and three pion masses $M_\pi \approx 220$, 310 and 690 MeV. We calculate the gluon momentum fraction $\langle x \rangle_g$ and combine with the $xg(x)/\langle x \rangle_g$ calculated from the pseudo-PDF approach to nucleon gluon unpolarized PDF $xg(x)$ for the first time through lattice QCD simulation. We extract our results to physical pion mass and continuum limit, and compare with the determination by global fits.

In Sec. V.3.1, we present the pseudo-PDF procedure to obtain the lightcone gluon PDF and how we extracted the reduced pseudo Ioffe-time distribution (pITDs) from lattice calculated correlators. In Sec. V.3.2.2, we present our calculation of the gluon nonperturbative renormalization factor and obtain the renormalized gluon momentum fraction $\langle x \rangle_g$. In Sec. V.3.2.1, the final determination of the nucleon unpolarized gluon PDF $xg(x)$ is obtained through the $xg(x)/\langle x \rangle_g$ and $\langle x \rangle_g$ calculation results, and compared with the phenomenology global fit PDF

results. A discussion of the systematics and the outlook for the nucleon gluon PDFs are included in the last Sec. V.3.3.

V.3.1. Lattice correlators and matrix elements

In this work, we follow the same procedure used to calculate the pion gluon PDF in Sec. II of Ref. [195, 212], following the pseudo-PDF procedure as in Refs. [186, 204]. The gluon operator we used is also the same one as in Eq. 1 in Ref. [212].

$$\mathcal{O}(z) \equiv \sum_{i \neq z,t} \mathcal{O}(F^{ti}, F^{ti}; z) - \frac{1}{4} \sum_{i,j \neq z,t} \mathcal{O}(F^{ij}, F^{ij}; z), \tag{V.8}$$

where the operator $\mathcal{O}(F^{\mu\nu}, F^{\alpha\beta}; z) = F^{\mu}_{\nu}(z) U(z,0) F^{\alpha}_{\beta}(0)$, z is the Wilson link length. To extract the ground-state matrix element to construct the reduced pITD defined in Eq. 4, we use a 2-state fit on the two-point correlators and a two-sim fit on the three-point correlators in Eqs. 11 and 12 in Ref. [212].

We present our calculation of the nucleon gluon PDFs on clover valence fermions on four ensembles with $N_f = 2 + 1 + 1$ highly improved staggered quarks (HISQ) [71] generated by the MILC Collaboration [64] with three different lattice spacings ($a \approx 0.9, 0.12$ and 0.15 fm) and three pion masses (220, 310, 690 MeV), as shown in Table. 4. Following the study in Ref. [163], five HYP-smearing [89] steps are used on the gluon loops to reduce the statistical uncertainties. We use Gaussian momentum smearing for the quark fields [107] $q(x) + \alpha \sum_j U_j(x) e^{i(\frac{2\pi}{L})\mathbf{k}\hat{e}_j} q(x + \hat{e}_j)$, to reach higher meson boost momenta with the momentum-smearing parameter $\mathbf{k}$ listed in Table 7. The measurements vary 10^6–10^7 for different ensembles. More measurements and various lattice spacings are studied comparing to our previous nucleon gluon PDF calculation on one a12m310 ensemble with 10^5 measurements [195].

To study the reliability of our fitted matrix-element extraction, we compare to ratios of the three-point to the two-point correlator R^{Ratio},

$$R^{\text{Ratio}}_{\Phi}(z, P_z; t_{\text{sep}}, t) = \frac{C^{\text{3pt}}_{\Phi}(z, P_z; t_{\text{sep}}, t)}{C^{\text{2pt}}_{\Phi}(P_z; t)} \tag{V.9}$$

where the three-point and two-point correlators are defined in Eqs. 11 and 12 in Ref. [212]. The left-hand side of Fig. 25 shows example ratios for the gluon matrix elements from a12m220 and a09m310 ensembles light nucleon correlators at pion masses $M_\pi \approx \{220, 310\}$ MeV at

ensemble	a09m310	a12m220	a12m310	a15m310
a (fm)	0.0888(8)	0.1184(10)	0.1207(11)	0.1510(20)
$L^3 \times T$	$32^3 \times 96$	$32^3 \times 64$	$24^3 \times 64$	$16^3 \times 48$
M_π^{val} (MeV)	313.1(13)	226.6(3)	309.0(11)	319.1(31)
$M_{\eta_s}^{\text{val}}$ (MeV)	698.0(7)	696.9(2)	684.1(6)	687.3(13)
P_z (GeV)	[0,2.18]	$[0, 2.29]$	$[0, 2.14]$	$[0, 2.56]$
N_{meas}	387,456	1,466,944	324,160	129,600
t_{sep}	{6,7,8,9}	{6,7,8,9}	{6,7,8,9}	{5,6,7,8}

Table 4 Lattice spacing a, valence pion mass M_π^{val} and η_s mass $M_{\eta_s}^{\text{val}}$, lattice size $L^3 \times T$, number of configurations N_{cfg}, number of total two-point correlator measurements $N_{\text{meas}}^{\text{2pt}}$, and separation times t_{sep} used in the three-point correlator fits of $N_f = 2 + 1 + 1$ clover valence fermions on HISQ ensembles generated by the MILC collaboration and analyzed in this study. More details on the parameters used in the calculation are included in the Table 7 in the appendix.

selected momenta P_z and Wilson-line length z. The ratios increase with increasing source-sink separation t_{sep} and continuously to approach the ground-state matrix elements as going to larger t_{sep}. The gray bands represent the ground-state matrix elements extracted using the two-sim fit to three-point correlators at five t_{sep}, where the energies are from the two-state fits of the two-point correlators. The one-state fit results increase as t_{sep} increases, which behaves similar to the ratios in the left-hand side plot. The third and fourth columns of Fig. 25 show two-sim fits using $t_{\text{sep}} \in [t_{\text{sep}}^{\text{min}}, 9]$ and $t_{\text{sep}} \in [5, t_{\text{sep}}^{\text{max}}]$ to study how the two-sim ground-state matrix elements depend on the source-sink separations input into fit. We observe that the matrix elements are consistent with each other within one standard deviation, and they begin to converge at large $t_{\text{sep}}^{\text{min}}$ and $t_{\text{sep}}^{\text{max}}$, showing consistent extraction of the ground-state matrix element. Taking a09m310 ensemble as an example, we observe larger fluctuations in the matrix element extractions when small $t_{\text{sep}}^{\text{min}} = 3$ and 4, or small $t_{\text{sep}}^{\text{max}} = 6$ and 7, are used. The ground state matrix element extracted from two-sim fits becomes very stable when $t_{\text{sep}}^{\text{min}} > 5$ and $t_{\text{sep}}^{\text{max}} > 8$.

V.3.2. Results and Discussions

V.3.2.1 $xg(x)/ < x >_g$ Results

The Ioffe-time pseudo-distribution (pITD) [203, 186] is:

$$\mathcal{M}(\nu, z^2) = \langle 0(P_z)|\mathcal{O}(z)|0(P_z)\rangle, \tag{V.10}$$

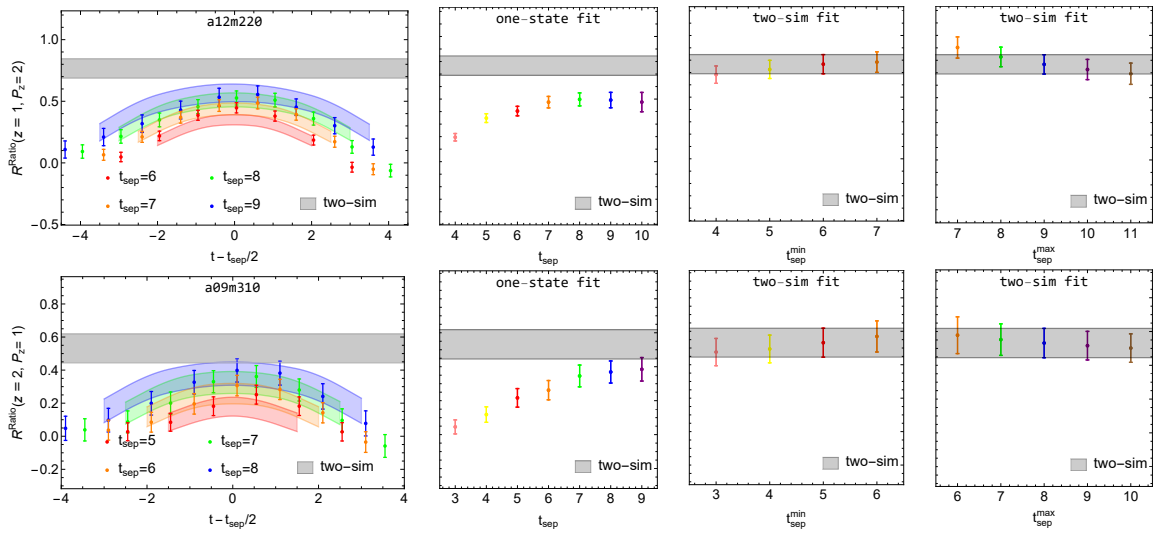

Figure 25 Example ratio plots (left), one-state fits (second column) and two-sim fits (last 2 columns) from a12m220 and a09m310 ensembles light nucleon correlators at pion masses $M_\pi \approx \{220, 310\}$ MeV. The gray band shown on all plots is the extracted ground-state matrix element from the two-sim fit we used as our final fit. From left to right, the columns are: the ratio of the three-point to two-point correlators with the reconstructed fit bands from the two-sim fit using the final t_{sep} inputs, shown as functions of $t - t_{\mathrm{sep}}/2$, the one-state fit results for the three-point correlators at each $t_{\mathrm{sep}} \in [3, 10]$, the two-sim fit results using $t_{\mathrm{sep}} \in [t_{\mathrm{sep}}^{\mathrm{min}}, t_{\mathrm{sep}}^{\mathrm{max}}]$ varying $t_{\mathrm{sep}}^{\mathrm{min}}$ and $t_{\mathrm{sep}}^{\mathrm{max}}$.

The reduced pITD (RpITD) [186, 201, 249] was constructed to remove the ultraviolet divergences in the pITD by taking a double-ratio of the pITD,

$$\mathscr{M}(\nu, z^2) = \frac{\mathcal{M}(zP_z, z^2)/\mathcal{M}(0 \cdot P_z, 0)}{\mathcal{M}(z \cdot 0, z^2)/\mathcal{M}(0 \cdot 0, 0)}. \tag{V.11}$$

The renormalization of $\mathcal{O}(z)$ and kinematic factors are cancelled in the RpITDs. By construction, the RpITD double ratios employed here are normalized to one at $z = 0$.

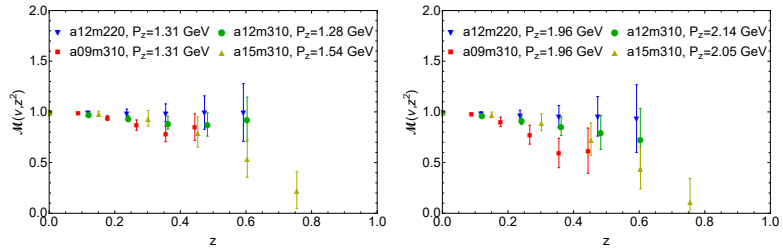

Figure 26 The RpITDs at boost momenta $P_z \approx 2$ GeV and 1.3 GeV as functions of z obtained from the fitted bare ground-state matrix elements for $M_\pi \approx \{220, 310, 310, 310\}$ MeV on a12m220, a09m310, a12m310, a15m310 ensembles respectively.

We can then extract the gluon PDF distribution through the pseudo-PDF matching condi-

tion [204] that connects the RpITD $\mathscr{M}$ to the lightcone gluon PDF $g(x,\mu^2)$ through

$$\mathscr{M}(\nu,z^2)=\int_0^1 dx\frac{xg(x,\mu^2)}{\langle x\rangle_g}R_{gg}(x\nu,z^2\mu^2), \tag{V.12}$$

where μ is the renormalization scale in the $\overline{\text{MS}}$ scheme and $\langle x\rangle_g = \int_0^1 dx\, xg(x,\mu^2)$ is the gluon momentum fraction of the nucleon. R_{gg} is the gluon-in-gluon matching kernel we used in Ref. [195, 212, 214], which originally derived in Ref. [204]. We ignore the quark PDF contributes to the RpITDs in this calculation based on our findings in the past pion gluon PDF study [212]. One can obtain the gluon PDF $g(x,\mu^2)$ by fitting the RpITD through the matching condition in Eq. V.12; a similar procedure has also been used by HadStruc Collaboration [191, 13, 213].

We examine the pion-mass and lattice-spacing dependence on the RpITDs extracted in the previous section. The left panel of Fig. 26 shows the RpITDs at boost momentum around 1.3 GeV as functions of the Wilson-line length z for the a12m220, a09m310, a12m310, and a15m310 ensembles. We see no noticeable lattice-spacing dependence. The bottom of Fig. 26 shows the pion RpITDs with boost momentum around 12 GeV for the same ensembles. Again, there is no visible lattice-spacing or pion-mass dependence.

To obtain the gluon PDF $g(x,\mu^2)$ on the right-hand side of Eq. V.12, we adopt the phenomenologically motivated form

$$f_g(x,\mu)=\frac{xg(x,\mu)}{\langle x\rangle_g(\mu)}=\frac{x^A(1-x)^C}{B(A+1,C+1)}, \tag{V.13}$$

for $x\in[0,1]$ and zero elsewhere. The beta function $B(A+1,C+1)=\int_0^1 dx\, x^A(1-x)^C$ is used to normalize the area to unity. Such a form is also used in global fits to obtain the nucleon gluon PDF by CT18 [2] and the pion gluon PDF by JAM [4, 24].

We fit the lattice RpITDs $\mathscr{M}^{\text{lat}}(\nu,z^2,a,M_\pi)$ obtained in Eq. V.11 to the parametrization form $\mathscr{M}^{\text{fit}}(\nu,\mu,z^2,a,M_\pi)$ in Eq. V.12 by minimizing the χ^2 function,

$$\begin{aligned}&\chi^2(\mu,a,M_\pi)=\\&\sum_{\nu,z}\frac{(\mathscr{M}^{\text{fit}}(\nu,\mu,z^2,a,M_\pi)-\mathscr{M}^{\text{lat}}(\nu,z^2,a,M_\pi))^2}{\sigma^2_{\mathscr{M}}(\nu,z^2,a,M_\pi)}.\end{aligned} \tag{V.14}$$

The reconstructed fit bands of the kaon RpITDs for the a12m220, a09m310, a12m310 and a15m310 ensembles, and nucleon RpITDs at each z^2, compared with the lattice calculation

points, are shown in Fig. 27 from left to right. We see almost no z^2-dependence (labeled in different colors) in the reconstructed bands in both a12m310 ensembles, but slightly more dependence in the a15m310 case. We found the a12m220, a12m310 fit to the nucleon gluon PDF to have very stable quality with χ^2/dof around 1 with consistent output of $f_g(x,\mu)$, regardless of the choice of the maximum value of the Wilson-line displacement z. However, for the a09m310, a15m310 ensemble, χ^2/dof can go as large as 4.2(1.3) and 6.0(2.0) respectively. We suspect that higher-twist effects are enhanced at this coarse lattice spacing such that the fit fails to accurately describe the lattice data. Possible future work including NNLO matching may help to improve the fit on this ensemble.

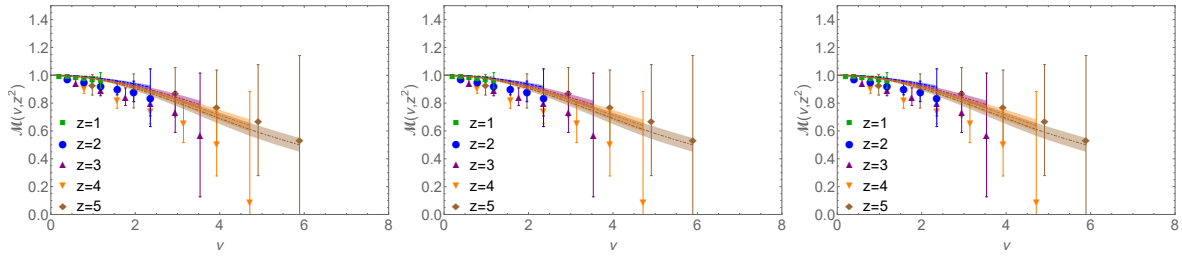

Figure 27 The RpITDs $\mathscr{M}$ with the reconstructed bands from fits in Eq. V.14 on the a09m310, a12m310, a15m310 lattice ensembles for nucleon respectively.

We also attempt to obtain the nucleon gluon PDF at physical pion mass and continuum limit based on the RpITDs for a12m220, a09m310, a12m310 and a15m310 ensembles. Similar to the calculations we performed previous based on RpITDs, we use "z-expansion" fit [241, 242] (also adopted by past pseudo-PDF calculations [191]) and include the pion mass M_π and lattice spacing a dependence terms into the fit as well,

$$\mathscr{M}(\nu, z^2, a, M_\pi) = \sum_{k=0}^{k_{\text{max}}} \lambda_k \tau^k + l_1 a^2 + l_2 (M_\pi^2 - (M_\pi^{\text{phys}})^2) + l_3 z^2, \tag{V.15}$$

where $\tau = \frac{\sqrt{\nu_{\text{cut}}+\nu}-\sqrt{\nu_{\text{cut}}}}{\sqrt{\nu_{\text{cut}}+\nu}+\sqrt{\nu_{\text{cut}}}}$. We vary ν_{cut} between [0.5,2] and the results are consistent with each other and we choose $\nu_{\text{cut}} = 1$ in our fits. We fix the $\lambda_0 = 1$ because of the normalization we have for the reduced ITD $\mathscr{M}(\nu, z^2)$ in Eq. V.11, and the maximum term $k_{\text{max}} = 3$ is used. The reconstructed fitted bands of a09m310 and a12m220 light nucleons are shown in the left plot of Fig. 28. The χ^2/dof of the fit is 0.72(64) with $k_{\text{max}} = 3$. We also analysis the a dependence in first order linear term, which are compared in the right plot of Fig. 28, where the a-term RpITD band is smaller than a^2-term RpITD band. The a^2-term RpITD at physical

pion mass and continuum limit can be also used in the parametrization form fit in Eq. V.14. A fit range of $\nu \in [0, 10]$ and $z \approx 0.1$ fm are used in the a^2-term RpITD fit. The extracted RpITD can be used in Eq. V.14 to obtain the gluon PDF directly. We choose to discretize the continuum fitted a^2-term RpITD by using $z = 0.1$ fm and $aL = 0.2 \times \pi$ fm to implement the same fit procedure as we did for the other RpITDs from different ensembles. The fit results are shown in Fig. 29, compared with the with the RpITDs matched from global-fit gluon PDFs from CT18 and NNPDF3.1 at NNLO. The RpITD bands are consistent with each other within the one-sigma error range. The reconstructed gluon PDF, $xg(x,\mu)/\langle x\rangle_g$ obtained from the fits to the different lattice ensembles data for the light nucleon, and the fit to the extrapolated data at physical pion mass and continuum limit are shown in Fig. 34, where the lattice spacing and pion mass dependence are shown to be weak.

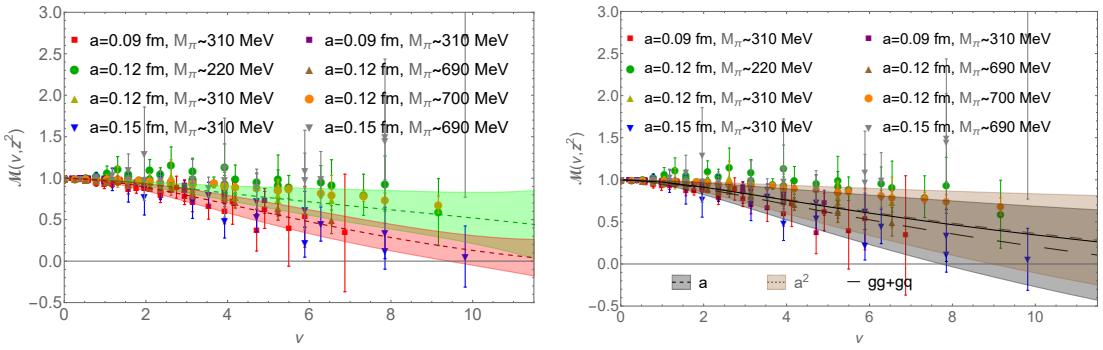

Figure 28 The preliminary RpITDs $\mathscr{M}$ with the example reconstructed bands from fits in Eq. V.15 on the a09m310 (red), a12m220 (green) lattice ensembles in the left-hand plot and the extrapolated bands at physical pion mass and continuum limit in the right one. The lattice spacing a dependence and gluon-in-quark contribution are studied and compared in the right-hand plot.

We investigate the systematic uncertainty comes from neglecting the contribution of the quark term based on the assumption (motivated by global fits) that the pion $q_S(x)$ is smaller than the gluon PDF. Currently, there are no $q_S(x)$ results from lattice simulation since only the isovector distribution of the nucleon has been done. Thus, we estimate the systematic due to omitting the $q_S(x)$ contribution by using the nucleon quark PDFs from CT18 at NNLO [2]. Using these, we obtain revised RpITDs including the gluon-in-quark R_{gq} term as shown in the right-hand side of Fig. 28, we show the mean value of $xg(x)/\langle x\rangle_g$ with both gluon-in-gluon (gg) and gluon-in-quark (gq) contributions (the black solid line) compared to the results using

the gluon-in-gluon contribution only (the black dashed line) in Fig. 34. There are smaller than 5% differences in the mean value including the gluon-in-gluon contribution for $x < 0.9$, which indicates that the gluon-in-quark contribution is relatively small at $\mu^2 = 4\,\text{GeV}^2$ compared to the current statistical errors in the small-x region. In the $x > 0.9$ region, the gluon-in-quark contribution becomes more significant, but it remains smaller than the statistical error.

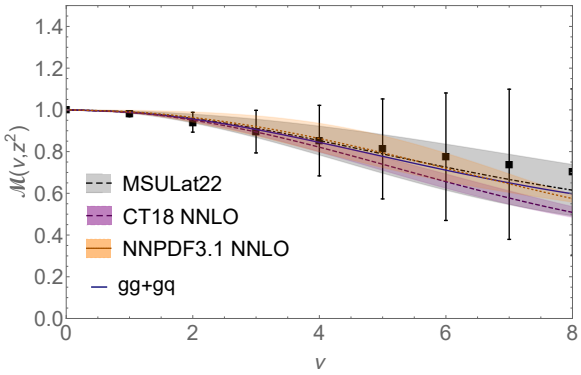

Figure 29 The preliminary RpITDs $\mathscr{M}$ with reconstructed bands from fits at phyiscal pion mass and continuum limit, comparing with the RpITDs matched from global-fit PDFs, and the RpITD mean value reconstructed included the gluon-in-quark contribution.

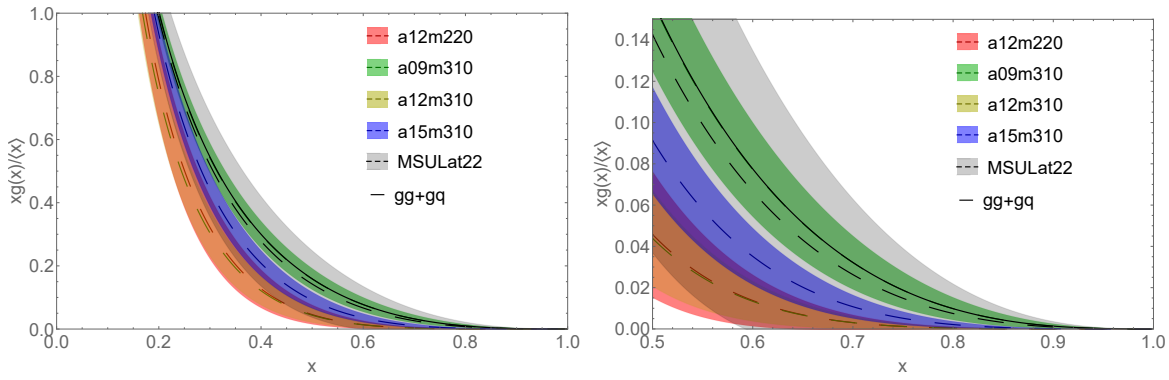

Figure 30 The preliminary unpolarized gluon PDF, $xg(x,\mu)/\langle x\rangle_g$ in the large-x region as a function of x and its zoomed in plot, obtained from the fits to the different lattice ensembles data compared with the fit to the extrapolated data at physical pion mass and continuum limit, and the mean value fit including the gluon-in-quark term in the matching.

V.3.2.2 Renormalized gluon moments

The gluon momentum faction $\langle x\rangle_g$ is important in understanding the nucleon momentum, mass and spin [260, 261]. Thus, a lattice-QCD calculation of the $\langle x\rangle_g$ itself is also of fundamental interest. Available calculations of $\langle x\rangle_g$ have significantly improved recently [262, 234]. For the bare gluon matrix element, it was found that hypercubic (HYP) smearing of the gluon

operators changes the bare matrix element significantly [263, 29]. Therefore, a nonperturbative renormalization (NPR) [118] of the the gluon momentum fraction is needed. The gluon momentum fraction operator we use is

$$O_{g,\mu\nu}(x) = \sum_{\alpha=0,1,2,3} (F^{\mu\alpha}(x)F^{\mu\alpha}(x) - F^{\nu\alpha}(x)F^{\nu\alpha}(x)), \tag{V.16}$$

where the field tensor

$$F_{\mu\nu} = \frac{i}{8a^2 g}(\mathcal{P}_{[\mu,\nu]} + \mathcal{P}_{[\nu,-\mu]} + \mathcal{P}_{[-\mu,-\nu]} + \mathcal{P}_{[-\nu,\mu]}), \tag{V.17}$$

where the plaquette $\mathcal{P}_{\mu,\nu} = U_\mu(x)U_\nu(x+a\hat{\mu})U_\mu^\dagger(x+a\hat{\nu})U_\nu^\dagger(x)$ and $\mathcal{P}_{[\mu,\nu]} = \mathcal{P}_{\mu,\nu} - \mathcal{P}_{\nu,\mu}$. After we obtain the gluon bare matrix element from lattice calculation, we renormalize using a nonperturbative RI-MOM scheme and then implement a perturbative matching to get the renormalized operators in the $\overline{\text{MS}}$ scheme:

$$O_g = R^{\overline{\text{MS}}}(\mu^2, \mu_R^2) Z_{O_g}(\mu_R^2) O_g^{\text{bare}}. \tag{V.18}$$

The matching factor $R^{\overline{\text{MS}}}(\mu^2, \mu_R^2)$ is calculated via perturbation theory in Ref. [125]. The RI-MOM renormalization factor $Z_{O_g}(\mu_R^2)$ can be obtained with the nonperturbative renormalization condition,

$$Z_g(p^2) Z_{O_g}(p^2) \Lambda_{O_g}^{\text{bare}}(p) (\Lambda_{O_g}^{\text{tree}}(p))^{-1}|_{p^2=\mu_R^2} = 1, \tag{V.19}$$

where $Z_g(p^2)$ is the gluon-field renormalization and $\Lambda_{O_g}(p)$ is the amputated Green function for the operator O_g in the Landau gauge-fixed gluon state. The NPR factor $Z_{O_g}(p^2)$ of the operator in Eq. V.16 is derived in Ref. [234, 30],

$$Z_{O_g}^{-1}(\mu_R^2) = \left. \frac{p^2 \langle O_{g,\mu\nu} \operatorname{Tr}[A_\tau(p) A_\tau(-p)] \rangle}{2(p_\mu^2 - p_\nu^2) \langle \operatorname{Tr}[A_\tau(p) A_\tau(-p)] \rangle} \right|_{p^2=\mu_R^2, \tau\neq\mu\neq\nu, p_\tau=0}. \tag{V.20}$$

Therefore, the gluon propagator $D_g(p)$ and gluon amputated Green's function $\Lambda_{O_g}(p)$ need to be calculated for the further calculation of the NPR factor,

$$\begin{aligned} D_{\mu\nu}(p) &= \langle \operatorname{Tr}[A_\tau(p) A_\tau(-p)] \rangle \\ \Lambda_{O_g}(p) &= \langle O_{g,\mu\nu} \operatorname{Tr}[A_\tau(p) A_\tau(-p)] \rangle. \end{aligned} \tag{V.21}$$

In Ref. [258, 30], a technique called cluster-decomposition error reduction (CDER) is used

to increase the signal to error ratio of NPR factor. The reason for such error reduction is that, for the disconnected insertions, the vacuum insertion dominates the variance, so that the relevant operators fluctuate independently and are independent of the time separation. This explains why the signal falls off exponentially, while the error remains constant in the disconnected insertions. The gluon operator inserted into the propagator in Eq. V.20 is a disconnected insertion on which the CDER technique can be used. Reference [30] introduces two cutoffs, r_1 between the glue operator and one of the gauge fields, and r_2 between the gauge fields in the gluon propagator to gluon amputated Green function $\Lambda_{O_g}(p)$,

$$\Lambda_{O_g} \equiv \Big\langle \int_{|r|<r_1} d^4r \int_{|r'|<r_2} d^4r' \int d^4x\, e^{ip\cdot r'} O_{g,\mu\nu}(x+r)\, \mathrm{Tr}[A_\rho(x) A_\rho(x+r')] \Big\rangle. \tag{V.22}$$

Reference [30] studies the gluon nonperturbative renormalization on the 2+1-flavor RBC/UKQCD domain-wall fermion (DWF) Iwasaki gauge ensemble with lattice spacing $a = 0.114$ fm, $m_\pi = 140$ MeV and lattice volume $L^3 \times T = 48^3 \times 96$ with 0 and 1 step of HYP smearing [263], a quenched Wilson gauge ensemble and two two-flavor clover fermion Lüscher-Weisz gauge ensembles as well. They finds that the CDER technique provide improvement on the lattice with the cutoffs $r_1 \approx 0.9$ fm and $r_2 \approx 1.3$ fm, and such improvement is insensitive of the lattice definition of operators and the HYP smearing steps within their uncertainties.

In our work, instead of using the CDER radius cutoffs from Ref. [263], we use $L_c^4\times$ truncated lattices to calculate the NPR factor $Z_{O_g}(p^2)$ on the original $L^3 \times T$ lattice. For different ensembles, we have $L_c^4\times$ truncated lattices listed in Table 5.

ensemble	a09m310	a12m310	a15m310
L_c	$\{16, 20, 24, 28\}$	$\{12, 16, 20\}$	$\{8, 12\}$
N_{cfg}	94	88	100
N_{meas}	1504	1408	1600

Table 5 The truncation length L_c, the number of configurations N_{cfg} and measurements N_{meas} that we used for different lattice ensembles. We use 16 sources for the truncation on each configurations; thus, N_{meas} is 16 times N_{cfg}.

The smallest cutoff L_c we used are about 1.4, 1.4, and 1.2 fm for a09m310, a12m310, and a15m310 ensembles respectively, which are larger than the smallest cutoff $2r_1 \approx 0.8$ fm used in Ref. [30]. Though Ref. [30] show results for which the $2r_1 \geq 1.8$ fm cutoff give consistent results with the full calculation NPR factors, the small cutoff results in the region

$0.8 \leq 2r_1 \leq 1.8$ are still helpful in the final fit of the NPR factors. Therefore, our cutoff from the smallest $L_c \approx 1.2$ fm to the largest full lattice size are reasonable choices.

Following the procedure to renormalize the bare matrix element to a nonperturbative RI-MOM scheme and then implement a perturbative matching, we get the renormalized moment in the $\overline{\text{MS}}$ scheme,

$$\langle x \rangle_g^{\text{MS}} = Z_{\mathcal{O}}^{\overline{\text{MS}}}(\mu^2, \mu_R^2) \langle x \rangle_g^{\text{bare}} = R^{\overline{\text{MS}}}(\mu^2, \mu_R^2) Z_{\mathcal{O}}(\mu_R^2) \langle x \rangle_g^{\text{bare}} \tag{V.23}$$

where the $Z_{\mathcal{O}}^{\overline{\text{MS}}}(\mu^2, \mu_R^2)$ is the complete multiplicative renormalization constant, and the one-loop expression for the perturbative matching, derived in Ref. [125] is used:

$$R^{\overline{\text{MS}}}(\mu^2, \mu_R^2) = 1 - \frac{g^2 N_f}{16\pi^2}\left(\frac{2}{3}\log(\mu^2/\mu_R^2) + \frac{10}{9}\right) - \frac{g^2 N_c}{16\pi^2}\left(\frac{4}{3} - 2\xi + \frac{\xi^2}{4}\right) \tag{V.24}$$

where $N_f = 4$, $N_c = 3$, $\xi = 0$ in the Landau gauge, g^2 is $4\pi\alpha(\mu)$ [126, 127, 128], and $\mu = 2$ GeV is used in our calculation. With the functional form

$$\left(Z_{\mathcal{O}}^{\overline{\text{MS}}}\right)^{-1}((\mu = 2\text{ GeV})^2, p^2) = \left(Z_{\mathcal{O}}^{\overline{\text{MS}}}\right)^{-1}(0) + C_1 p^2 + C_2 p^4, \tag{V.25}$$

we fit the renormalization factor $(Z_{\mathcal{O}}^{\overline{\text{MS}}})^{-1}(p^2)$ and the fit bands from different ensembles are shown in Fig. 31. Different cutoff lengths L_c give consistent results for $(Z_{\mathcal{O}}^{\overline{\text{MS}}})^{-1}(0)$ within one sigma error. The multiplicative renormalization constants $(Z_{\mathcal{O}}^{\overline{\text{MS}}})^{-1}(0)$ for the three ensembles are listed in Table 6.

To calculate the bare gluon first moment (gluon momentum fraction) $\langle x \rangle_g^{\text{bare}}$, we use the gluon operator we defined in Ref. [163],

$$\mathcal{O}(z) \equiv \sum_{i,j=x,y,z,t} \mathcal{O}(F^{ti}, F^{ti}; z) - \frac{1}{4} \sum_{i,j=x,y,z,t} \mathcal{O}(F^{ij}, F^{ij}; z), \tag{V.26}$$

After normalizing the bare matrix elements with the kinematic factor $\frac{E_0}{\frac{3}{4}E_0^2 + \frac{1}{4}P_z^2}$, the bare gluon momentum fraction $\langle x \rangle_g^{\text{bare}}$ is the normalized bare matrix element at $z = 0$. Figure 32 shows the bare matrix element extracted from three-point and two-point correlators. The bare matrix elements we calculated for the gluon moments use the same parameter settings and number of measurements as listed in Table 4. We fit $\langle x \rangle_g^{\text{bare}}$ to a constant with the fit range $P_z \in [0, 5] \times 2\pi/L$, and we extract $\langle x \rangle_g^{\text{bare}} = 0.567(47)$ on the a12m310 ensemble. Using Eq. V.23 and the extracted $(Z_{\mathcal{O}}^{\overline{\text{MS}}})^{-1}$ results, we obtain the $\langle x \rangle_g^{\overline{\text{MS}}} = 0.457(38)_{\text{stat}}(20)_{\text{NPR}}$, where the second error

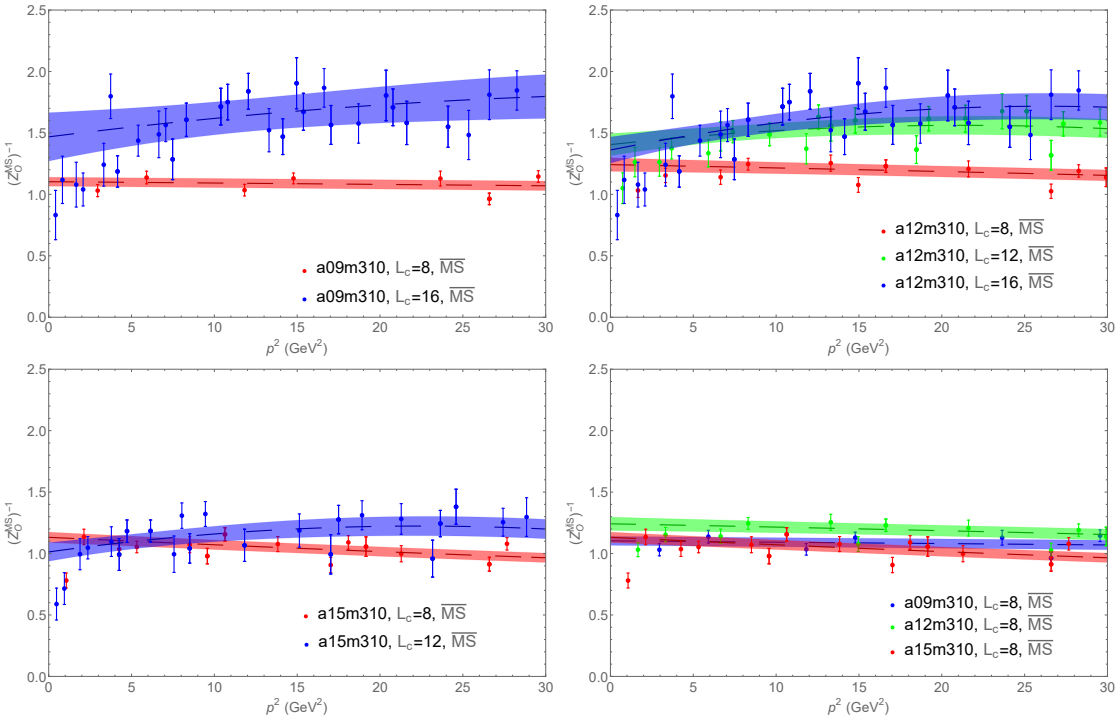

Figure 31 The preliminary multiplicative renormalization constants $(Z_{\mathcal{O}}^{\overline{\text{MS}}})^{-1}((\mu = 2\,\text{GeV})^2, p^2)$ as function of p^2 for a09m310, a12m310, a15m310 ensembles are shown in the upper-left, upper-right, lower-left plots, respectively. A comparison of different ensembles renormalization factor and their fit bands are shown in the lower-right plot. The fit band comes from the fit form in Eq. V.25. The lower limits of the fit range of the momentum are chosen to be the same as in Ref. [28].

comes from the renormalization error. The numbers for the bare gluon momentum fraction $\langle x \rangle_g^{\text{bare}}$, and the renormalized gluon momentum fraction $\langle x \rangle_g^{\overline{\text{MS}}}$ for all four ensembles are listed in Table 6.

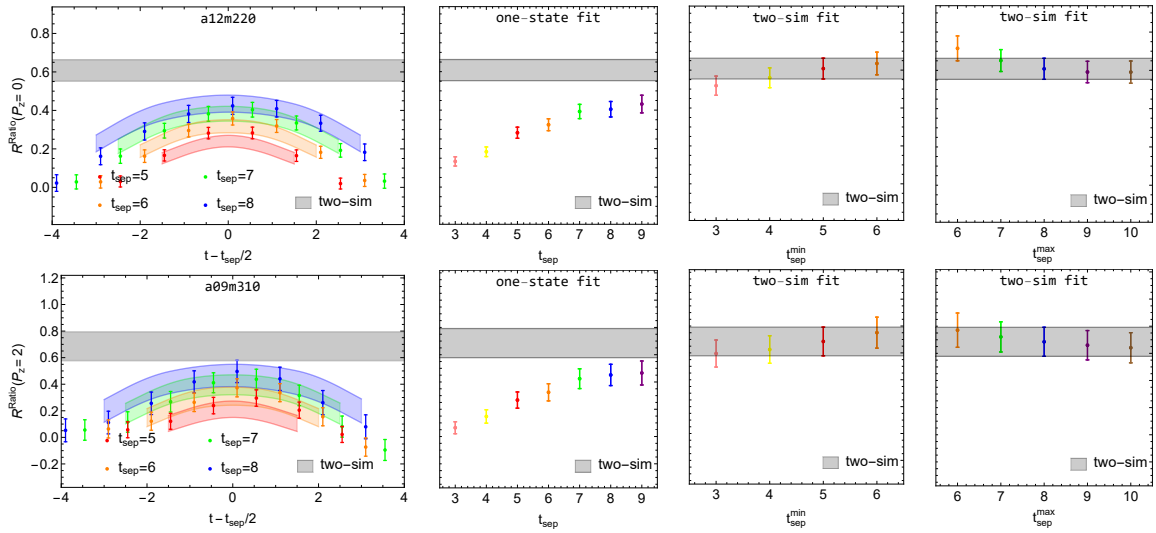

Figure 32 Example ratio plots (left), one-state fits (second column) and two-sim fits (last 2 columns) from the a15m310 light nucleon correlators at pion masses $M_\pi \approx 310$ MeV. The gray band shown on all plots is the extracted ground-state matrix element from the two-sim fit using $t_{\text{sep}} \in [5, 8]$. From left to right, the columns are: the ratio of the three-point to two-point correlators with the reconstructed fit bands from the two-sim fit using $t_{\text{sep}} \in [5, 8]$, shown as functions of $t - t_{\text{sep}}/2$, the one-state fit results for the three-point correlators at each $t_{\text{sep}} \in [3, 9]$, the two-sim fit results using $t_{\text{sep}} \in [t_{\text{sep}}^{\text{min}}, 8]$ as functions of $t_{\text{sep}}^{\text{min}}$, and the two-sim fit results using $t_{\text{sep}} \in [5, t_{\text{sep}}^{\text{max}}]$ as functions of $t_{\text{sep}}^{\text{max}}$.

ensemble	$\langle x \rangle_g^{\text{bare}}$	L_c	$(Z_{\mathcal{O}}^{\overline{\text{MS}}})^{-1}(0)$	$\langle x \rangle_g^{\overline{\text{MS}}}$
a12m220	0.639(40)	12	1.33(11)	$0.480(30)_{\text{stat}}(38)_{\text{NPR}}$
		16	1.18(14)	$0.541(34)_{\text{stat}}(66)_{\text{NPR}}$
a09m310	0.615(84)	16	1.11(14)	$0.555(76)_{\text{stat}}(71)_{\text{NPR}}$
		20	1.08(18)	$0.567(77)_{\text{stat}}(92)_{\text{NPR}}$
a12m310	0.594(46)	12	1.33(11)	$0.447(34)_{\text{stat}}(36)_{\text{NPR}}$
		16	1.18(14)	$0.503(39)_{\text{stat}}(61)_{\text{NPR}}$
a15m310	0.310(51)	8	1.01(06)	$0.307(50)_{\text{stat}}(19)_{\text{NPR}}$
		12	1.05(13)	$0.295(49)_{\text{stat}}(36)_{\text{NPR}}$

Table 6 The complete multiplicative renormalization constant $\left(Z_{\mathcal{O}}^{\overline{\text{MS}}}\right)^{-1}(0)$, the bare gluon momentum fraction $\langle x \rangle_g^{\text{bare}}$, and the renormalized gluon momentum fraction $\langle x \rangle_g^{\overline{\text{MS}}}$ for four ensembles used in this calculation. We use the a12m310 NPR factors for a12m220 $\langle x \rangle_g^{\overline{\text{MS}}}$ calculation, since the mass dependence is weak for the NPR factors.

Since we have data from four ensembles at roughly three lattice spacings and three pion masses, we are able to do a controlled extrapolation to the physical pion mass $M_\pi = 135$ MeV

and lattice spacing $a = 0$. We assume a simple quadratic relation for M_π and a,

$$\langle x\rangle_g^{\overline{\rm MS}}(M_\pi, a) = \langle x\rangle_g^{\overline{\rm MS},\rm cont} + k_M(M_\pi^2 - (M_\pi^{\rm phys})^2) + k_a a^2 \tag{V.27}$$

where the $M_\pi^{\rm phys} = 135$ MeV. The $\langle x\rangle_g^{\overline{\rm MS},\rm cont}$ fit result is $0.640(59)$ with $\chi^2/\text{dof} = 0.46(37)$. The reconstructed fit bands at $M_\pi \in \{135, 310, 690\}$ MeV as functions of a are shown in the left plot of Fig. 33, and the bands at $a \in \{0, 0.09, 0.12, 0.15\}$ fm as functions of M_π are shown in the right plot of Fig. 33. As we can see in the plots, the pion-mass dependence of the gluon momentum fraction is weak. They show some lattice-spacing dependence on different pion masses. In both pion-mass cases, the gluon momentum fraction $\langle x\rangle_g^{\overline{\rm MS}}$ becomes larger at the lattice spacing a approaches zero.

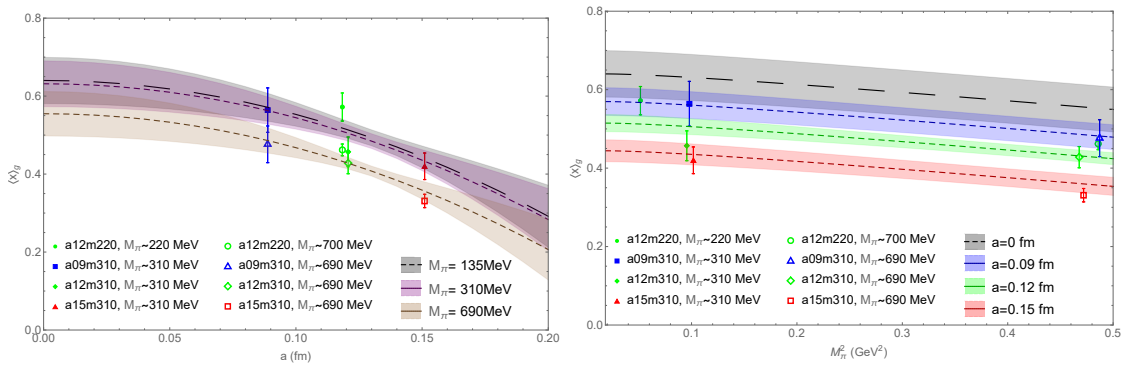

Figure 33 The preliminary renormalized gluon momentum fraction $\langle x\rangle_g^{\overline{\rm MS}}$ extrapolation in lattice spacing a and pion mass M_π. The reconstructed fit bands at $M_\pi \in \{135, 310, 690\}$ MeV as function of a and the bands at $a \in \{0, 0.09, 0.12, 0.15\}$ fm as function of M_π are shown in the left and right plots, respectively.

V.3.2.3 $xg(x)$ Results

The unpolarized nucleon gluon PDF $xg(x)$ can be extracted by taking the ratio of $f_g(x,\mu) = xg(x,\mu)/\langle x\rangle_g(\mu)$ and the gluon momentum fraction obtained $\langle x\rangle_g(\mu)$ in Sec. V.3.2.2. The unpolarized nucleon gluon PDF $xg(x)$ at physical pion mass $M_\pi = 135$ MeV and the continuum limit $a \to 0$ is obtained from the extrapolated $\langle x\rangle_g^{\overline{\rm MS},\rm cont}$ and $xg(x)/\langle x\rangle_g$ fitted from the extrapolated RpITDs. The unpolarized nucleon gluon PDF $xg(x)$ at physical pion mass and the continuum limit is included as gray bands in all plots in Fig. 34. The upper two plots in Fig. 34 show $xg(x)$ from the light nucleons of four ensembles compared with the extrapolated $xg(x)$. A comparison of our unpolarized nucleon gluon PDF with CT18 NNLO and NNPDF3.1 NNLO at $\mu = 2$ GeV in the $\overline{\rm MS}$ scheme is shown in lower-left plot in Fig. 34. We found that

our gluon PDF is consistent with the one from CT18 NNLO and NNPDF3.1 NNLO within one sigma error. The strong deviation between our lattice results and the global fits in our previous work [195] is not seen in this work. One major reason for the disappearance of the difference is that the gluon momentum fractions $\langle x \rangle_g^{\overline{\rm MS}}$ are different, ours $\langle x \rangle_g^{\overline{\rm MS}} \approx 0.6$ and the global fits $\langle x \rangle_g^{\overline{\rm MS}} \approx 0.4$. Other possible reasons include statistical improvement and the change of fit strategy. To better show the large-x behavior, we zoom into the large-x region with $x \in [0.5, 1]$ for nucleon gluon PDFs, as shown in the Fig. 34. Our large-x results are consistent with global fits over $x \in [0.5, 1]$.

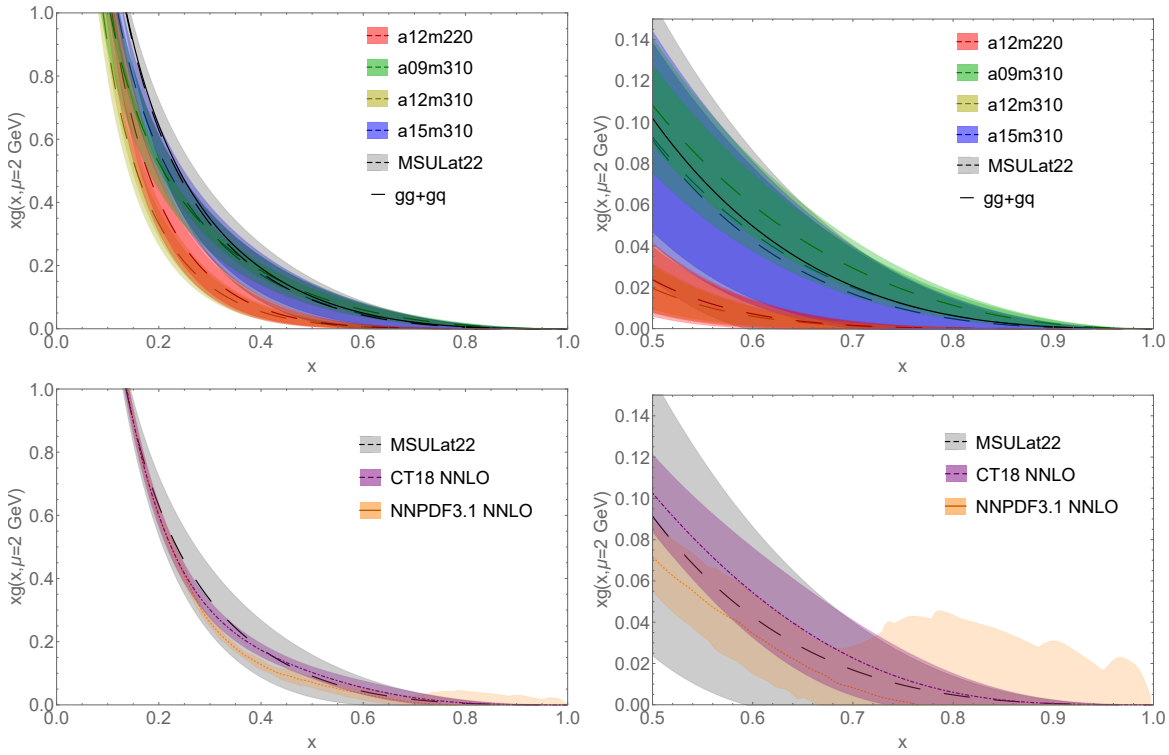

Figure 34 The preliminary unpolarized gluon PDF, $xg(x, \mu)$ in the large-x region as a function of x and a zoomed plot, obtained from the fit to the different lattice ensembles data compared with the CT18 NNLO (red band with dot-dashed line) and NNPDF3.1 NNLO (orange band with solid line) gluon PDFs. Our PDF results are consistent with the CT18 NNLO and NNPDF3.1 NNLO unpolarized gluon PDFs at $\mu = 2$ GeV in the $\overline{\rm MS}$ scheme within errors.

V.3.3. Summary

We extract the nucleon x-dependent gluon PDFs $xg(x)$ using clover fermions as valence action and 310-MeV 2+1+1 HISQ configurations generated by the MILC collaboration at three pion masses and three lattice spacings and find their dependence to be weak under the current statistics. We carefully studied the excited-state contributions to the matrix elements using

a two-state fitting strategy and made sure that our ground-state matrix elements were stably obtained. We then calculated the reduced pseudo-ITD using the obtained fitted ground-state matrix elements and extracted the gluon parton distribution. We extract the bare ground momentum fraction on the operator provided better signal-to-noise ratio and the NPR factors using a truncation method of lattices. The renormalized $\langle x \rangle_g^{\overline{\text{MS}}}$ is obtain by combining the bare results and renormalized factors. At last, we extract the $xg(x)$ by the combination of $xg(x)/\langle x \rangle_g$ through the pseudo-PDF matching of the RpITD and $\langle x \rangle_g^{\overline{\text{MS}}}$. Our lattice calculated unpolarized nucleon gluon PDF $xg(x)$ is consistent with the current global fit PDFs up to small-x region. There are systematics yet to be studied for the nucleon gluon PDF, such as quark PDF mixing, and the finite ν extent of the EpITD data. Thus, in our following work, we will study the the nucleon and pion gluon PDFs with improved statistics and better systematic control.

VI. Conclusion

In this thesis, we mainly focus on the unpolarized nucleon and pion gluon PDFs. Gluon PDF $g(x)$ contributes to the next-to-leading order (NLO) in the deep inelastic scattering (DIS) cross section, and enters at leading order in jet production. Gluon PDF dominates at low-x region especially at large scale μ. However, $g(x)$ is still the least known unpolarized PDF experimentally because the gluon does not couple to electromagnetic probes. Lattice QCD can be used to calculate the $g(x)$ since it is the main numerical tool to study the nonperturbative QCD. There are approaches such as, quasi-PDF, pseudo-PDF, "good lattice cross sections" and etc that make the x-dependent PDF calculations possible through lattice simulation.

The pion and nucleon x-dependent gluon PDFs are extracted using lattice simulation via quasi-PDF and pseudo-PDF methods in this theis. We use an improved gluon operator that is proved to be multiplicatively renormalizable. The use of the improved sources in the nucleon two-point correlators allowed us to reach higher nucleon boost momentum up to 2.3 GeV. The gluon nucleon matrix elements were obtained using two-state fits. The pion mass and lattice spacing dependents are studied, the systematics from functional forms used in the reconstruction fits and quark contribution in the matching are investigated.

In Chap. IV, we presented the first calculation of the pion gluon PDF using the pseudo-PDF approach using a 2-step fit on EpITDs. We employed clover valence fermions on ensembles with $N_f = 2 + 1 + 1$ HISQ at two lattice spacings and three pion masses, the pion mass and lattice spacing dependence appears to be weak. Our pion gluon PDF for the lightest pion mass is consistent with JAM'21 and DSE'20 for $x > 0.2$, and with xFitter'20 for $x > 0.5$ within uncertainty. We also studied the asymptotic behavior of the pion gluon PDF in the large-x region in terms of $(1 - x)^C$. $C > 3$ is implied from our study at two lattice spacings and three pion masses.

In Chap. V, we presented an exploratory study of the nucleon gluon PDF using the quasi-PDF approach, two studies of the nucleon gluon PDF using pseudo-PDF approach on one ensemble based on 2-step fit on EpITDs and on four ensembles based on 1-step fit on RpITDs, respectively. In the exploratory study using quasi-PDF, the renormalized quasi-PDF matrix elements are compared with the FT of the global-fit PDF and they are consistent within statistical

uncertainty. In the study using pseudo-PDF approach via 2-step fit, the $xg(x)/\langle x\rangle_g$ extrapolated to the physical pion mass $M_\pi = 135$ MeV is obtained, which is consistent with the one from CT18 NNLO and NNPDF3.1 NNLO within one sigma in the $x > 0.3$ region. In the study using pseudo-PDF approach via 1-step fit, we calculate gluon momentum fraction $langlex\rangle_g$, i.e. the first moment of gluon PDF under proper renomalization. The $xg(x)$ is then calculated on four ensembles with three lattice spacings and three pion masses.

APPENDIX

APPENDIX

In this section, we present the parameters that were not listed in Tab. 4. The plots for the 4 ensembles are shown as following order, the 2-point energy fit, effective mass, dispersion relation plots, the matrix element ratio plots, bare matrix element as function of z plots, RpITD as function of z/ν plots, and z_{max} fits RpITDs and $xg(x)$ plots.

ensemble	a09m310	a12m220	a12m310	a15m310
a (fm)	$0.0888(8)$	$0.1184(10)$	$0.1207(11)$	$0.1510(20)$
$L^3 \times T$	$32^3 \times 96$	$32^3 \times 64$	$24^3 \times 64$	$16^3 \times 48$
M_π^{val} (MeV)	$313.1(13)$	$226.6(3)$	$309.0(11)$	$319.1(31)$
$M_{\eta_s}^{\text{val}}$ (MeV)	698.0(7)	$696.9(2)$	$684.1(6)$	$687.3(13)$
P_z (GeV)	[0,2.18]	$[0, 2.29]$	$[0, 2.14]$	$[0, 2.56]$
N_{meas}	387,456	1,466,944	324,160	129,600
$\{\alpha, N_{\text{interation}}\}$	{3,60}	{3,60}	{3,60}	{3,60}
k	3.9	3.5	2.9	2.3
m_l	-0.075	-0.05138	-0.0695	-0.0893
m_s	-0.019938	-0.017	-0.0194	-0.021
t_{sep}	{6,7,8,9}	{5,6,7,8}	{5,6,7,8}	{6,7,8,9}

Table 7 Lattice spacing a, valence pion mass M_π^{val} and η_s mass $M_{\eta_s}^{\text{val}}$, lattice size $L^3 \times T$, number of configurations N_{cfg}, number of total two-point correlator measurements $N_{\text{meas}}^{\text{2pt}}$, the Gaussian smearing parameters $\{\alpha, N_{\text{interation}}\}$, the momentum smearing parameters **k** in $q(x) + \alpha \sum_j U_j(x) e^{i(\frac{2\pi}{L})\mathbf{k}\hat{e}_j} q(x + \hat{e}_j)$, mass parameters m_l and m_s for light and strange quarks respectively, and separation times t_{sep} used in the three-point correlator fits of $N_f = 2 + 1 + 1$ clover valence fermions on HISQ ensembles generated by the MILC collaboration and analyzed in this study.

.0.1. Two-point Energy Fit

The nucleons two-point correlators are then fitted to a two-state ansatz

$$C_N^{\text{2pt}}(P_z, t) = |A_{N,0}|^2 e^{-E_{N,0}t} + |A_{N,1}|^2 e^{-E_{N,1}t} + ..., \tag{1}$$

where the $|A_{N,i}|^2$ and $E_{N,i}$ are the ground-state ($i = 0$) and first excited state ($i = 1$) amplitude and energy, respectively. In this work, we use N_s to denote a nucleon composed of quarks such that $M_\pi \approx 690$ MeV and N_l to denote a nucleon composed of quarks such that $M_\pi \approx 310$ MeV. We perform an analysis of two exponential fits on 2-point correlators to obtain more reliable results for the excited state energies. We used E_0 as a prior to performed more stable two-exponential fits. The E_0 results as function of the fit range $[t_{\text{min}}, 11]$ from the two-state

exponential fits at $P_z \in [0,5] \times 2\pi/L$ for a09m310, a12m310, and a15m310 ensembles, $P_z \in [0,7] \times 2\pi/L$ for a12m220 ensemble are shown in Figs. 35, 36, 37, 38, 39, 40, 41. Taking a12m310 light nucleon at pion masses $M_\pi \approx 310$ MeV as an example, the E_0 results reach a plateau at t_{min}, therefore, $t_{\text{min}} = 4$ is used in the final 2-state fits for a12m310 light nucleon 2-point correlators.

.0.1.1 Strange Nucleon

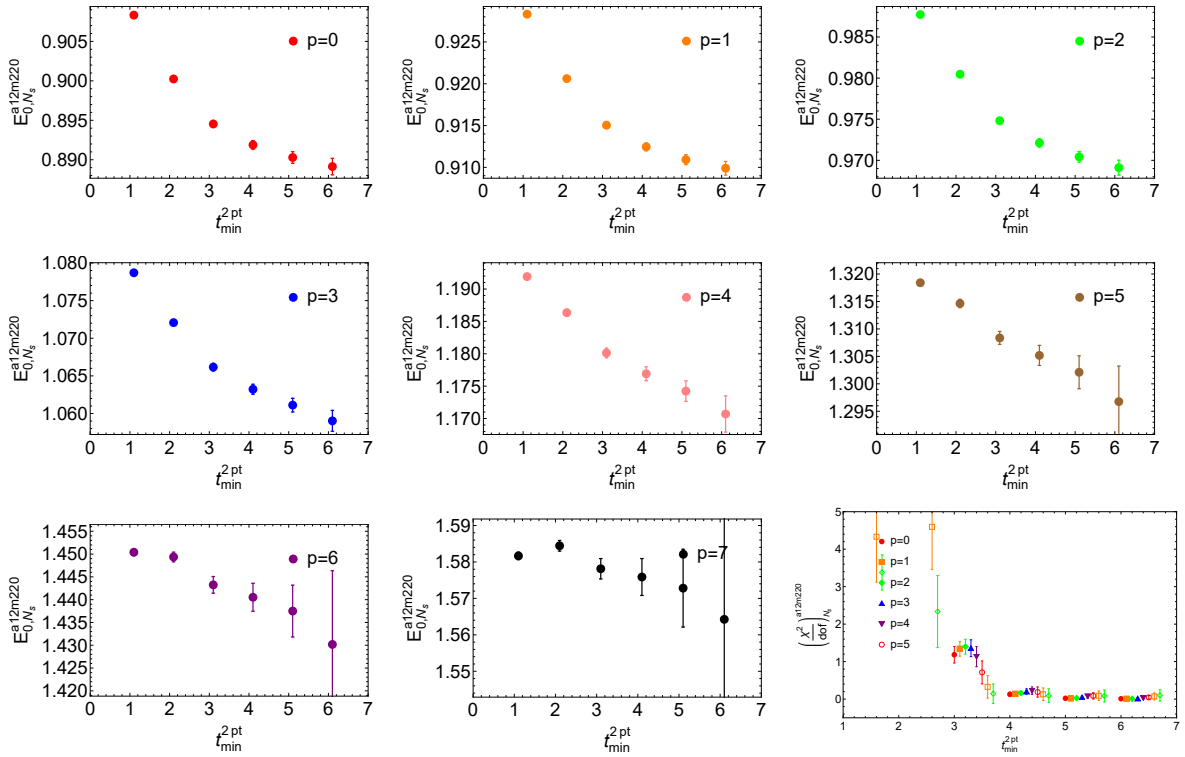

Figure 35 The fitted ground state energy and the χ^2/dof of 2-state fit as function of the 2-point correlator fit range $[t_{\text{min}}, 11]$ for the a12m220 ensemble strange nucleon at pion masses $M_\pi \approx 700$ MeV, at the momentum $P_z \in [0,7] \times 2\pi/L$. $t_{\text{min}} = 4$ is used in the final 2-state fits for a12m220 strange nucleon 2-point correlators.

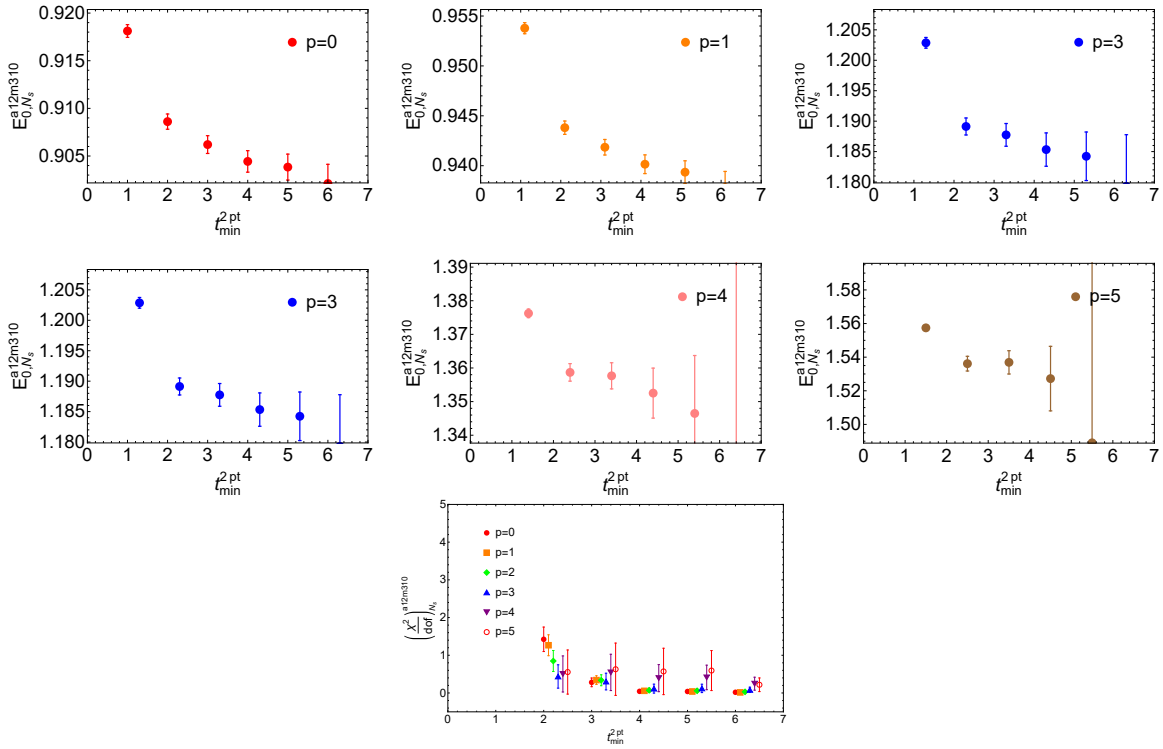

Figure 36 The fitted ground state energy and the χ^2/dof of 2-state fit as function of the 2-point correlator fit range $[t_{\text{min}}, 11]$ for the a12m310 ensemble strange nucleon at pion masses $M_\pi \approx 690$ MeV, at the momentum $P_z \in [0,5] \times 2\pi/L$. $t_{\text{min}} = 4$ is used in the final 2-state fits for a12m310 strange nucleon 2-point correlators.

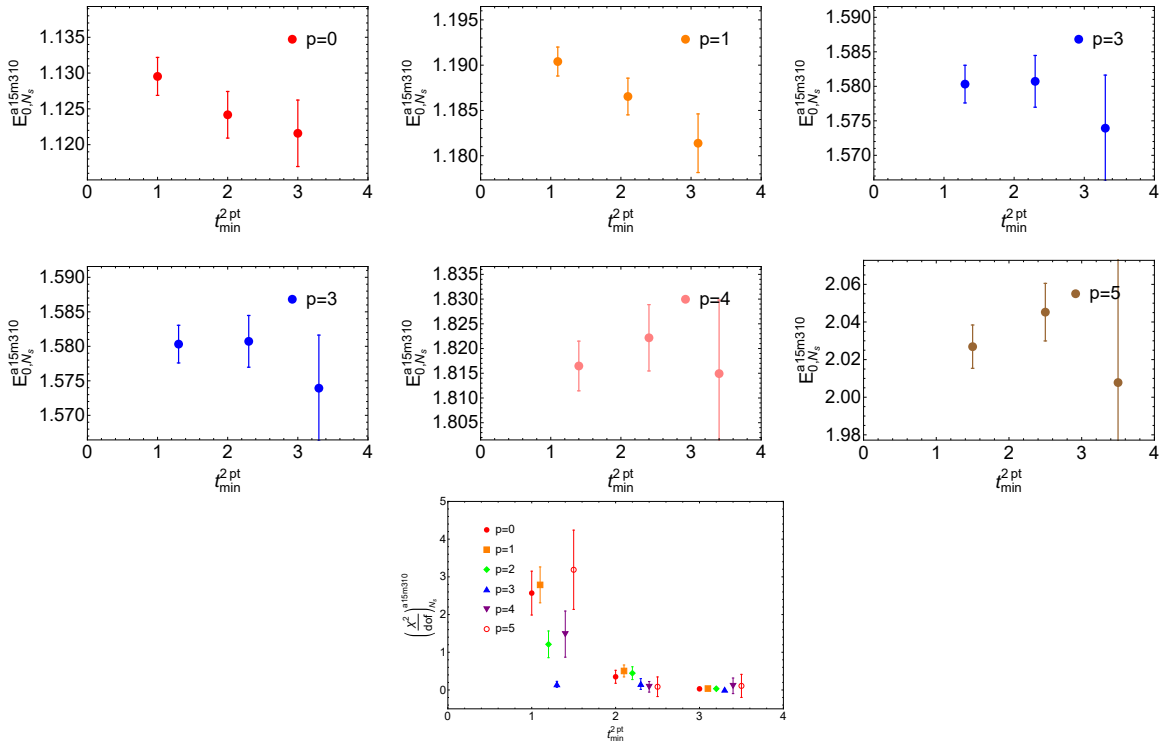

Figure 37 The fitted ground state energy and the χ^2/dof of 2-state fit as function of the 2-point correlator fit range $[t_{\text{min}}, 10]$ for the a15m310 ensemble strange nucleon at pion masses $M_\pi \approx 690$ MeV, at the momentum $P_z \in [0, 5] \times 2\pi/L$. $t_{\text{min}} = 1$ is used in the final 2-state fits for a15m310 strange nucleon 2-point correlators.

.0.1.2 Light Nucleon

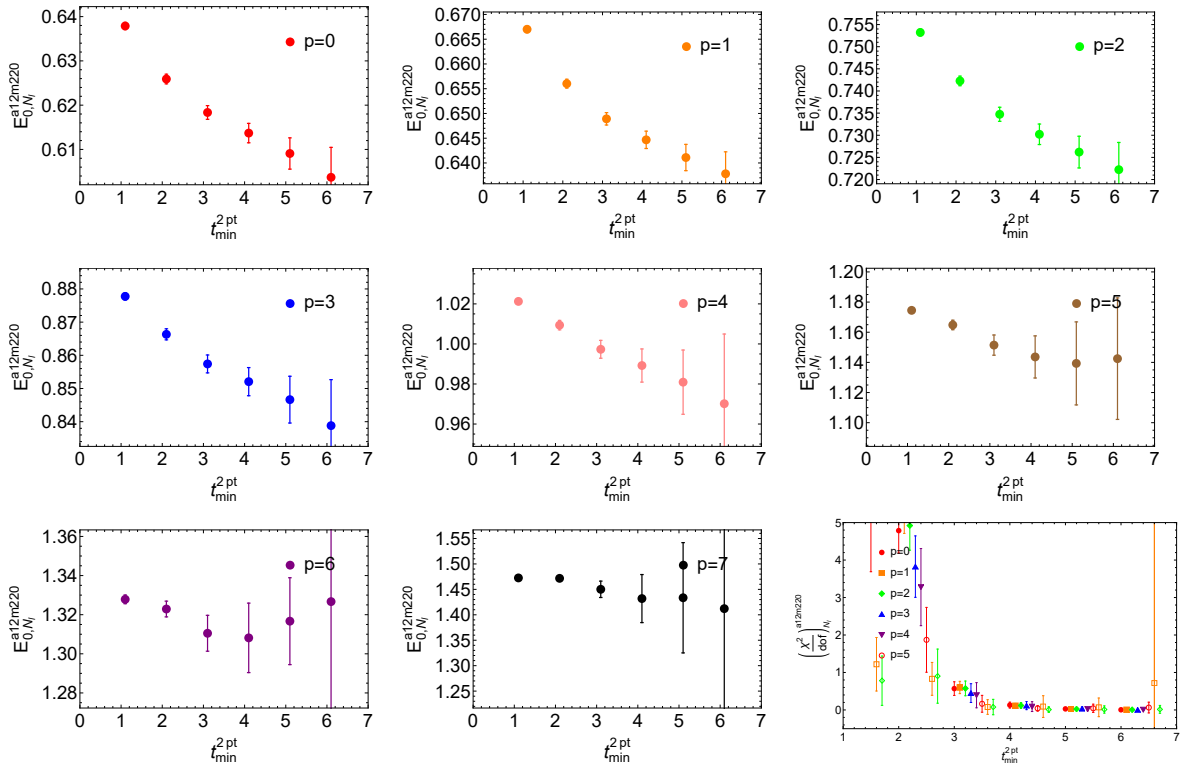

Figure 38 The fitted ground state energy and the χ^2/dof of 2-state fit as function of the 2-point correlator fit range $[t_{\text{min}}, 11]$ for the a12m220 ensemble light nucleon at pion masses $M_\pi \approx 220$ MeV, at the momentum $P_z \in [0, 7] \times 2\pi/L$. $t_{\text{min}} = 4$ is used in the final 2-state fits for a12m220 light nucleon 2-point correlators.

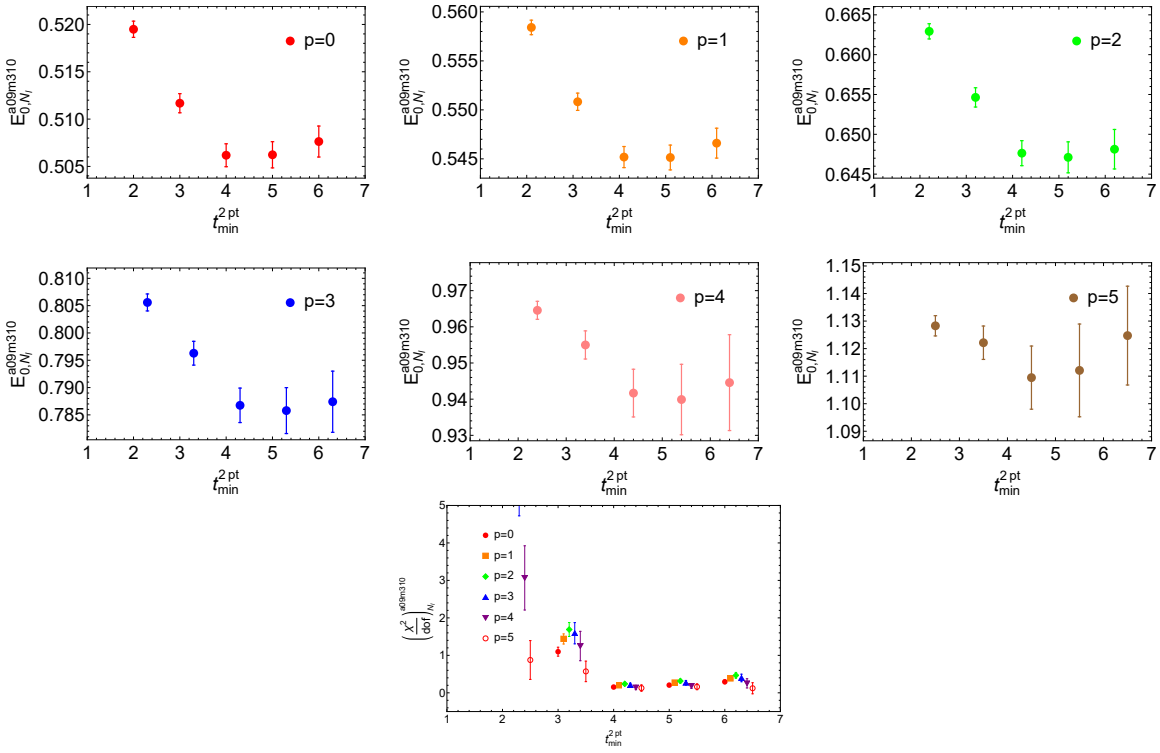

Figure 39 The fitted ground state energy and the χ^2/dof of 2-state fit as function of the 2-point correlator fit range $[t_{\text{min}}, 13]$ for the a09m310 ensemble light nucleon at pion masses $M_\pi \approx 310$ MeV, at the momentum $P_z \in [0,5] \times 2\pi/L$. $t_{\text{min}} = 4$ is used in the final 2-state fits for a09m310 light nucleon 2-point correlators.

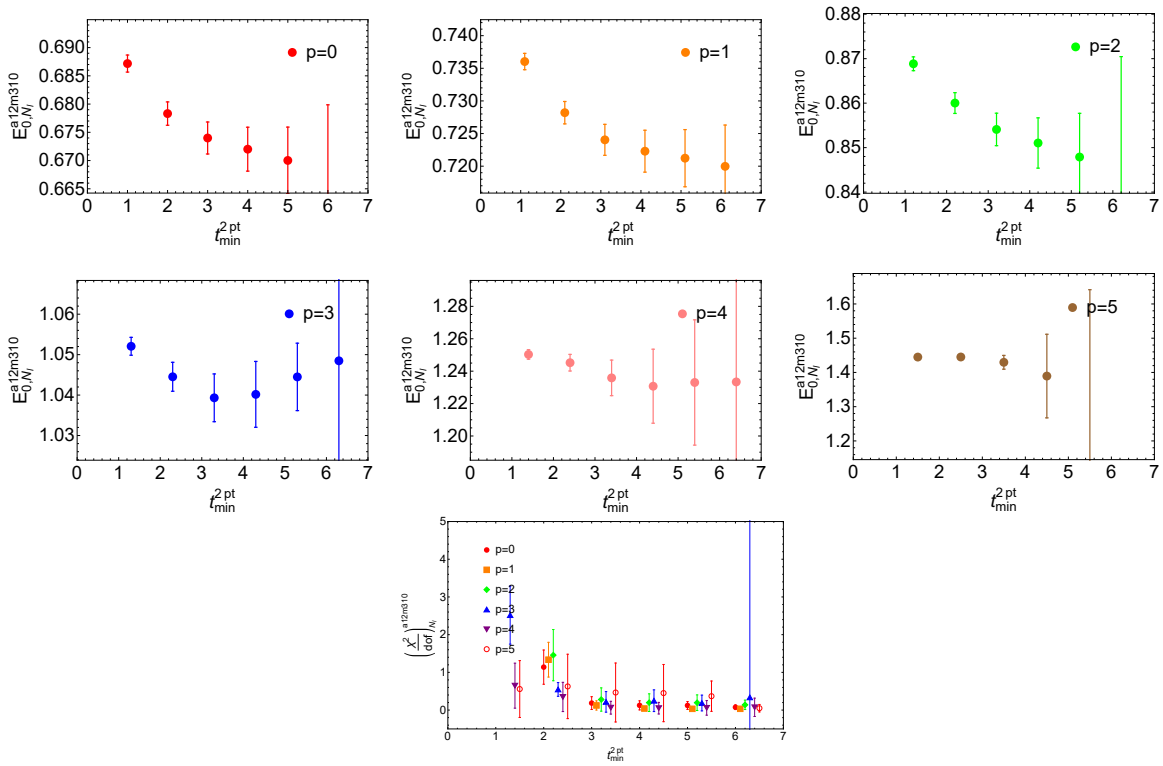

Figure 40 The fitted ground state energy and the χ^2/dof of 2-state fit as function of the 2-point correlator fit range $[t_{\text{min}}, 11]$ for the a12m310 ensemble light nucleon at pion masses $M_\pi \approx 310$ MeV, at the momentum $P_z \in [0,5] \times 2\pi/L$. $t_{\text{min}} = 4$ is used in the final 2-state fits for a12m310 light nucleon 2-point correlators.

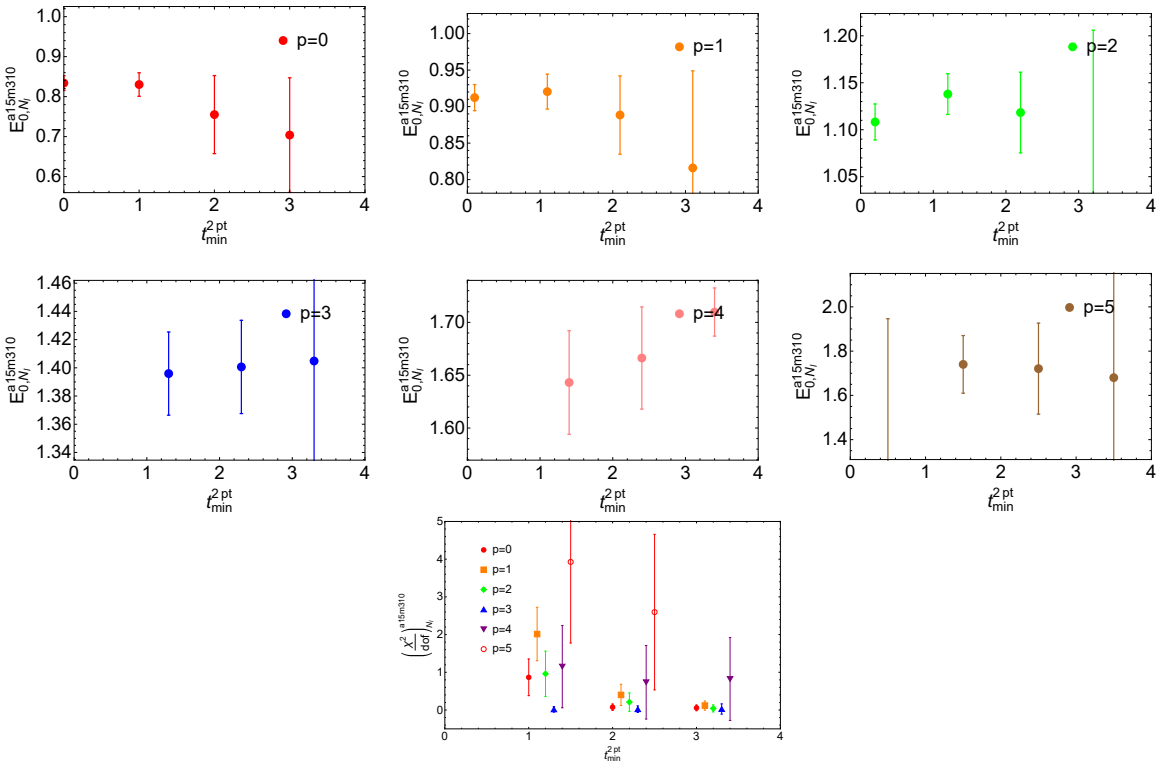

Figure 41 The fitted ground state energy and the χ^2/dof of 2-state fit as function of the 2-point correlator fit range $[t_{\text{min}}, 10]$ for the a15m310 ensemble light nucleon at pion masses $M_\pi \approx 310$ MeV, at the momentum $P_z \in [0, 5] \times 2\pi/L$. $t_{\text{min}} = 1$ is used in the final 2-state fits for a15m310 light nucleon 2-point correlators.

.0.2. Effective mass plot and fits

Figures 42, 43, 44, 45, 46, 47 and 48 shows the effective-mass plots for the nucleon two-point functions with at $P_z \in [0,5] \times 2\pi/L$ for a09m310, a12m310, and a15m310 ensembles, $P_z \in [0,7] \times 2\pi/L$ for a12m220 ensemble. The bands show the corresponding reconstructed fits using Eq. 1 with fit range $[4,13]$ for a09m310 ensemble, $[4,11]$ for a12m310 and a12m220 ensembles, $[1,10]$ for a15m310 ensemble. The bands are consistent with the data except where P_z and t are both large. The error of the effective masses at large P_z and t region is too large to fit. However, our reconstructed effective mass bands still match the the data points for the smaller t values even for the largest $P_z = 5 \times 2\pi/L$. We check the dispersion-relation $E^2 = E_0^2 + c^2 P_z^2$ of the nucleon energy as a function of the momentum, as shown in Fig. 49, 50. The speed of light c for the light quark is consistent with 1 within two sigma errors for a09m310, a12m220, a12m310 ensembles, however, deviated from 1 for the a15m310 ensemble light quark and all ensembles strange quark.

.0.2.1 Strange Nucleon

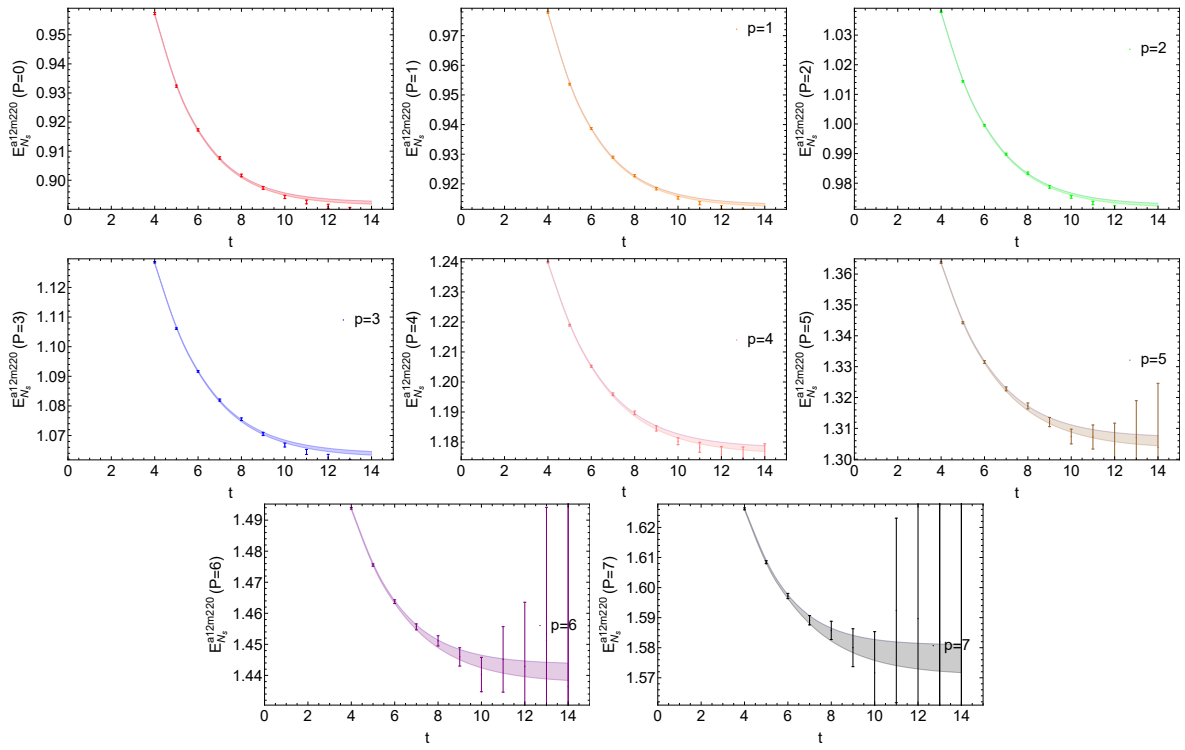

Figure 42 Nucleon effective-mass plots for $M_\pi \approx 700$ MeV, at $P_z = [0,7] \times \frac{2\pi}{L}$ on the a12m220 ensemble. The bands are reconstructed from the two-state fitted parameters of two-point correlators. The momentum $P_z = 7\frac{2\pi}{L}$ is the largest momentum we used, and it is the noisiest data set.

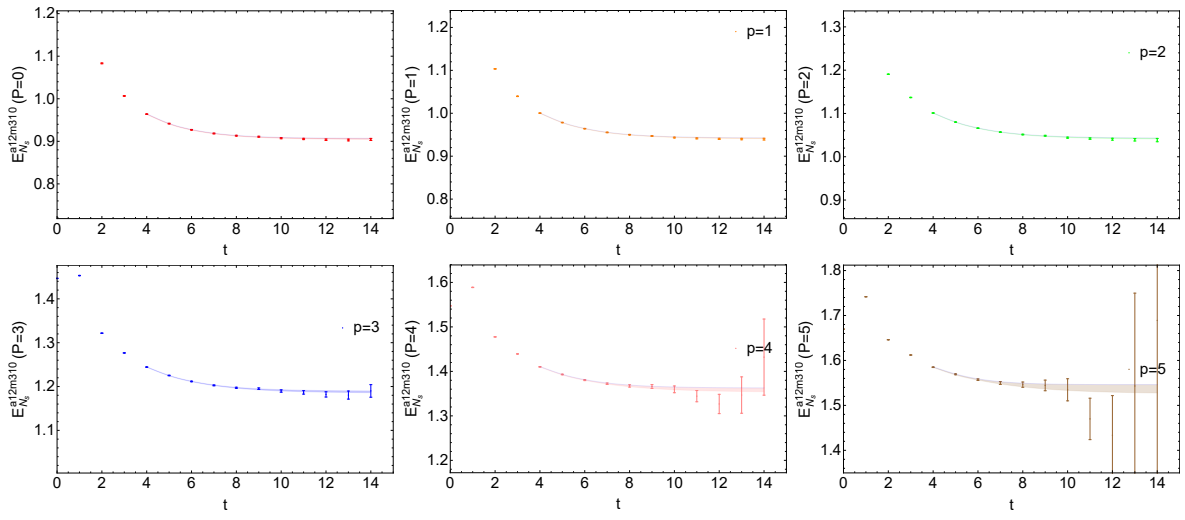

Figure 43 Nucleon effective-mass plots for $M_\pi \approx 690$ MeV, at $P_z = [0,5] \times \frac{2\pi}{L}$ on the a12m310 ensemble. The bands are reconstructed from the two-state fitted parameters of two-point correlators. The momentum $P_z = 5\frac{2\pi}{L}$ is the largest momentum we used, and it is the noisiest data set.

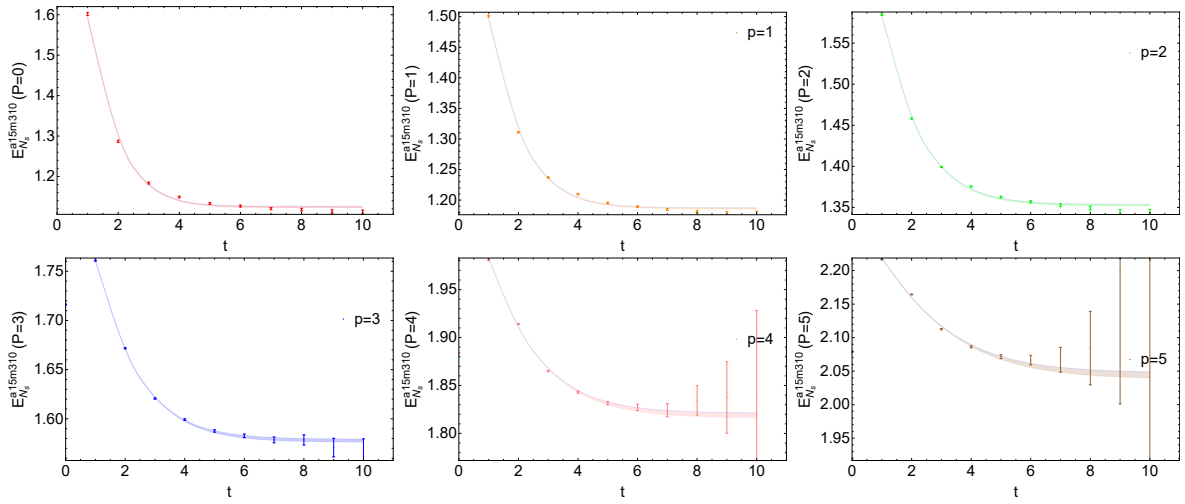

Figure 44 Nucleon effective-mass plots for $M_\pi \approx 690$ MeV, at $P_z = [0, 5] \times \frac{2\pi}{L}$ on the a15m310 ensemble. The bands are reconstructed from the two-state fitted parameters of two-point correlators. The momentum $P_z = 5\frac{2\pi}{L}$ is the largest momentum we used, and it is the noisiest data set.

.0.2.2 Light Nucleon

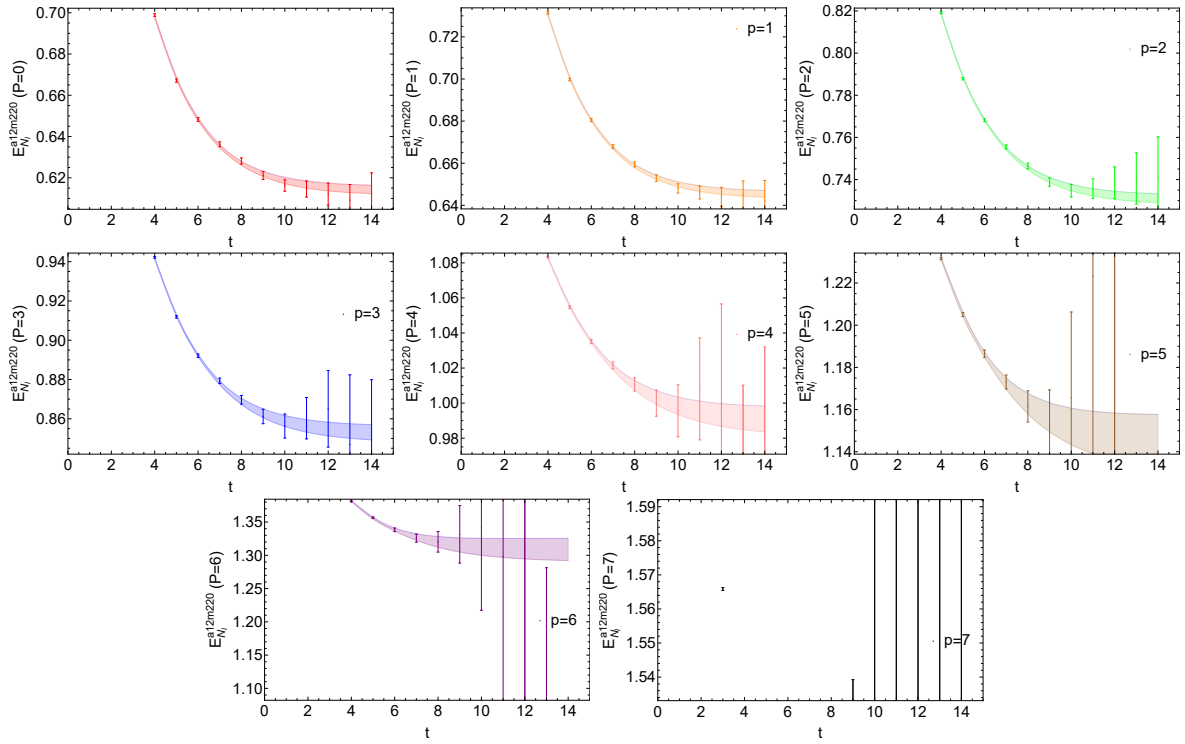

Figure 45 Nucleon effective-mass plots for $M_\pi \approx 220$ MeV, at $P_z = [0, 7] \times \frac{2\pi}{L}$ on the a12m310 ensemble. The bands are reconstructed from the two-state fitted parameters of two-point correlators. The momentum $P_z = 7\frac{2\pi}{L}$ is the largest momentum we used, and it is the noisiest data set.

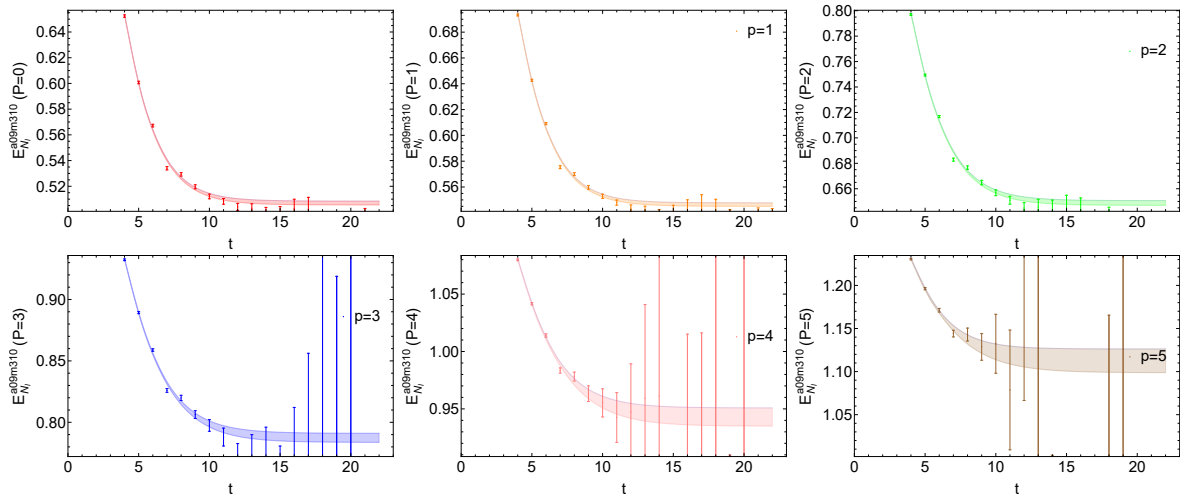

Figure 46 Nucleon effective-mass plots for $M_\pi \approx 310$ MeV, at $P_z = [0,5] \times \frac{2\pi}{L}$ on the a09m310 ensemble. The bands are reconstructed from the two-state fitted parameters of two-point correlators. The momentum $P_z = 5\frac{2\pi}{L}$ is the largest momentum we used, and it is the noisiest data set.

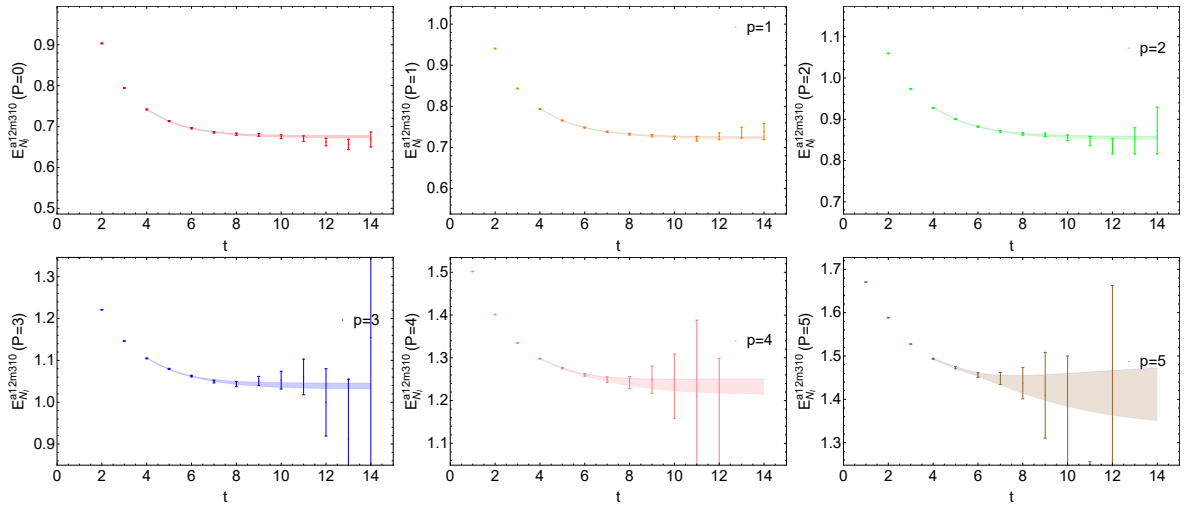

Figure 47 Nucleon effective-mass plots for $M_\pi \approx 310$ MeV, at $P_z = [0,5] \times \frac{2\pi}{L}$ on the a12m310 ensemble. The bands are reconstructed from the two-state fitted parameters of two-point correlators. The momentum $P_z = 5\frac{2\pi}{L}$ is the largest momentum we used, and it is the noisiest data set.

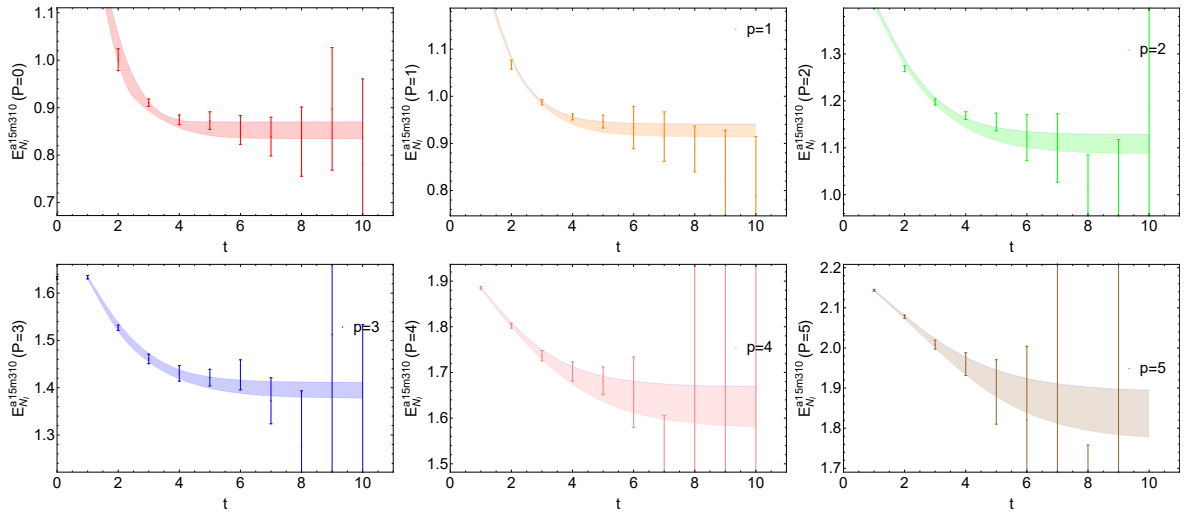

Figure 48 Nucleon effective-mass plots for $M_\pi \approx 310$ MeV, at $P_z = [0,5] \times \frac{2\pi}{L}$ on the a15m310 ensemble. The bands are reconstructed from the two-state fitted parameters of two-point correlators. The momentum $P_z = 5\frac{2\pi}{L}$ is the largest momentum we used, and it is the noisiest data set.

.0.3. Dispersion Plots

.0.3.1 Strange Nucleon

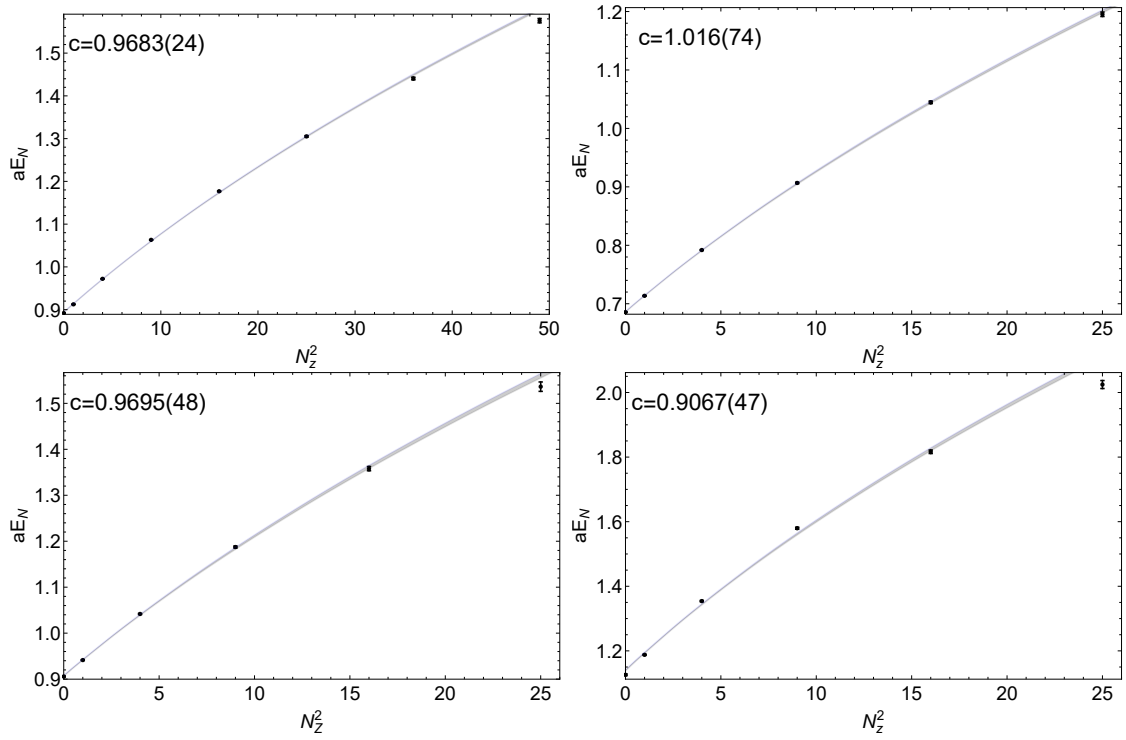

Figure 49 Dispersion relations of the nucleon energy from the two-state fits for $M_\pi \approx \{700, 690, 690, 690\}$ MeV (left) on a12m220, a09m310, a12m310, a15m310 ensembles respectively. The speed of ligt $c = 0.9638(24), 0.9695(48), 0.9067(47)$ repespectively.

.0.2 Light Nucleon

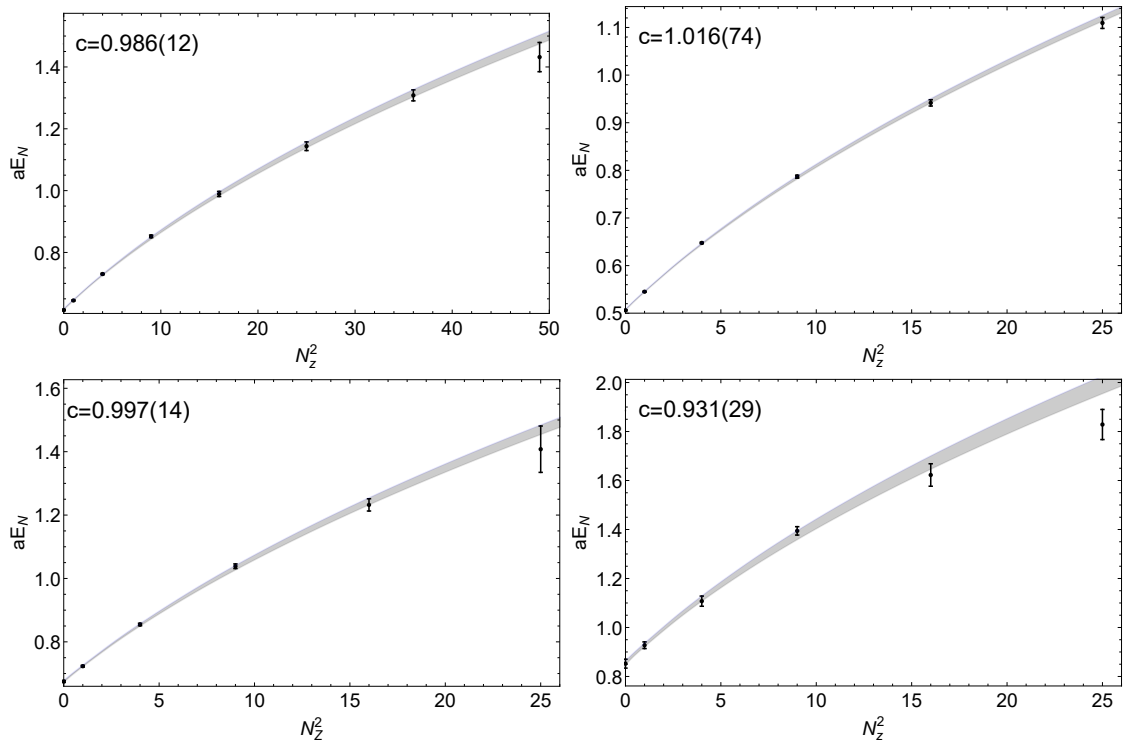

Figure 50 Dispersion relations of the nucleon energy from the two-state fits for $M_\pi \approx \{220, 310, 310, 310\}$ MeV (left) on a12m220, a09m310, a12m310, a15m310 ensembles respectively. The speed of ligt $c = 0.986(12), 1.0174(89), 0.997(14), 0.931(29)$ repespectively.

.0.4. Excited-State Check (ratio plot) for Matrix Elements

.0.4.1 Strange Nucleon

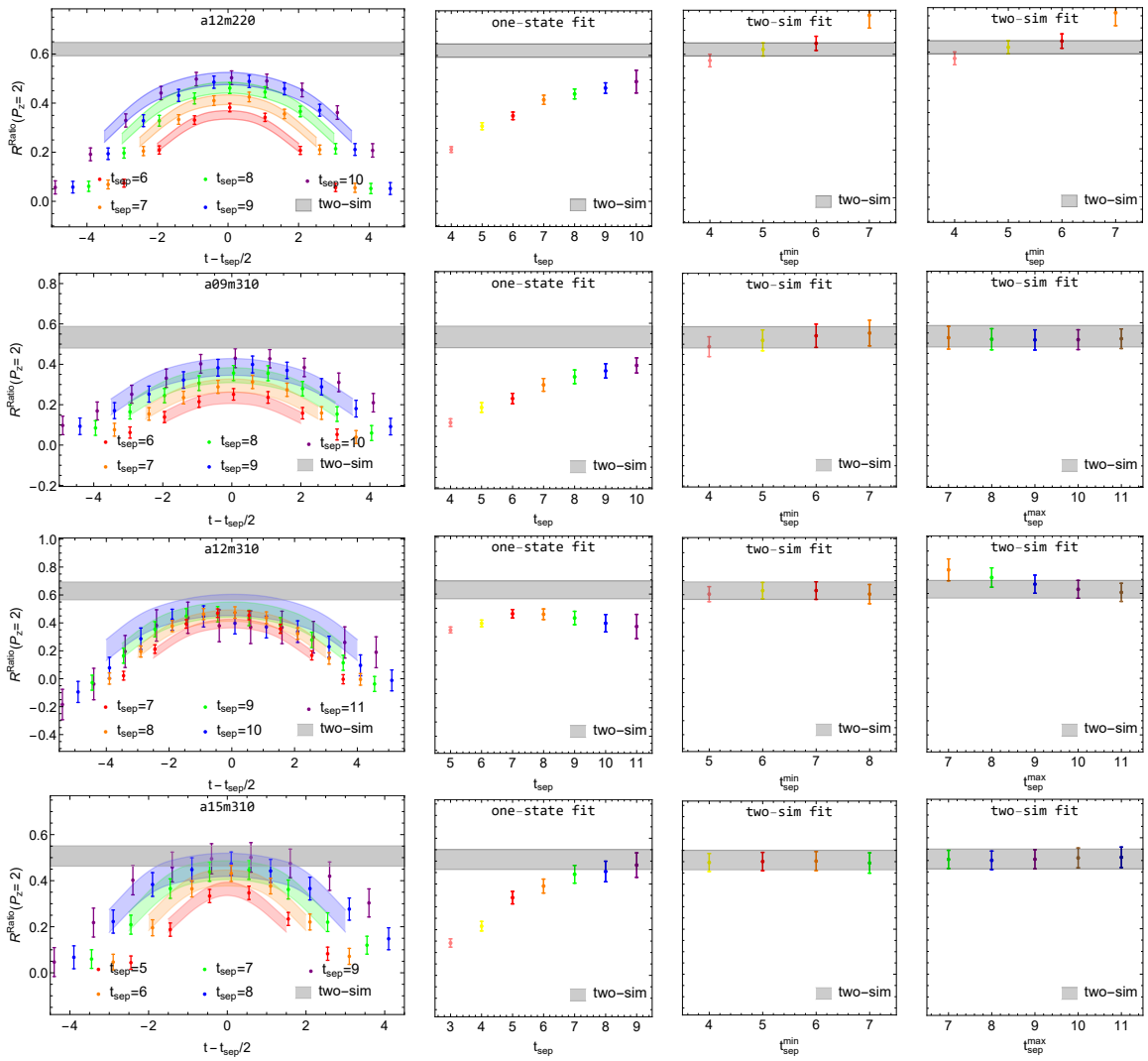

Figure 51 Example ratio plots (left), one-state fits (second column) and two-sim fits (last 2 columns) from the a12m220, a09m310, a12m310, a15m310 ensembles light nucleon correlators from top to bottom, at pion masses $M_\pi \approx \{700, 690, 690, 690\}$ MeV. The gray band shown on all plots is the extracted ground-state matrix element from the two-sim fit using $t_{\text{sep}} \in [5, 8]$. From left to right, the columns are: the ratio of the three-point to two-point correlators with the reconstructed fit bands from the two-sim fit using $t_{\text{sep}} \in [5, 8]$, shown as functions of $t - t_{\text{sep}}/2$, the one-state fit results for the three-point correlators at each $t_{\text{sep}} \in [3, 9]$, the two-sim fit results using $t_{\text{sep}} \in [t_{\text{sep}}^{\text{min}}, 8]$ as functions of $t_{\text{sep}}^{\text{min}}$, and the two-sim fit results using $t_{\text{sep}} \in [5, t_{\text{sep}}^{\text{max}}]$ as functions of $t_{\text{sep}}^{\text{max}}$.

.0.2 Light Nucleon

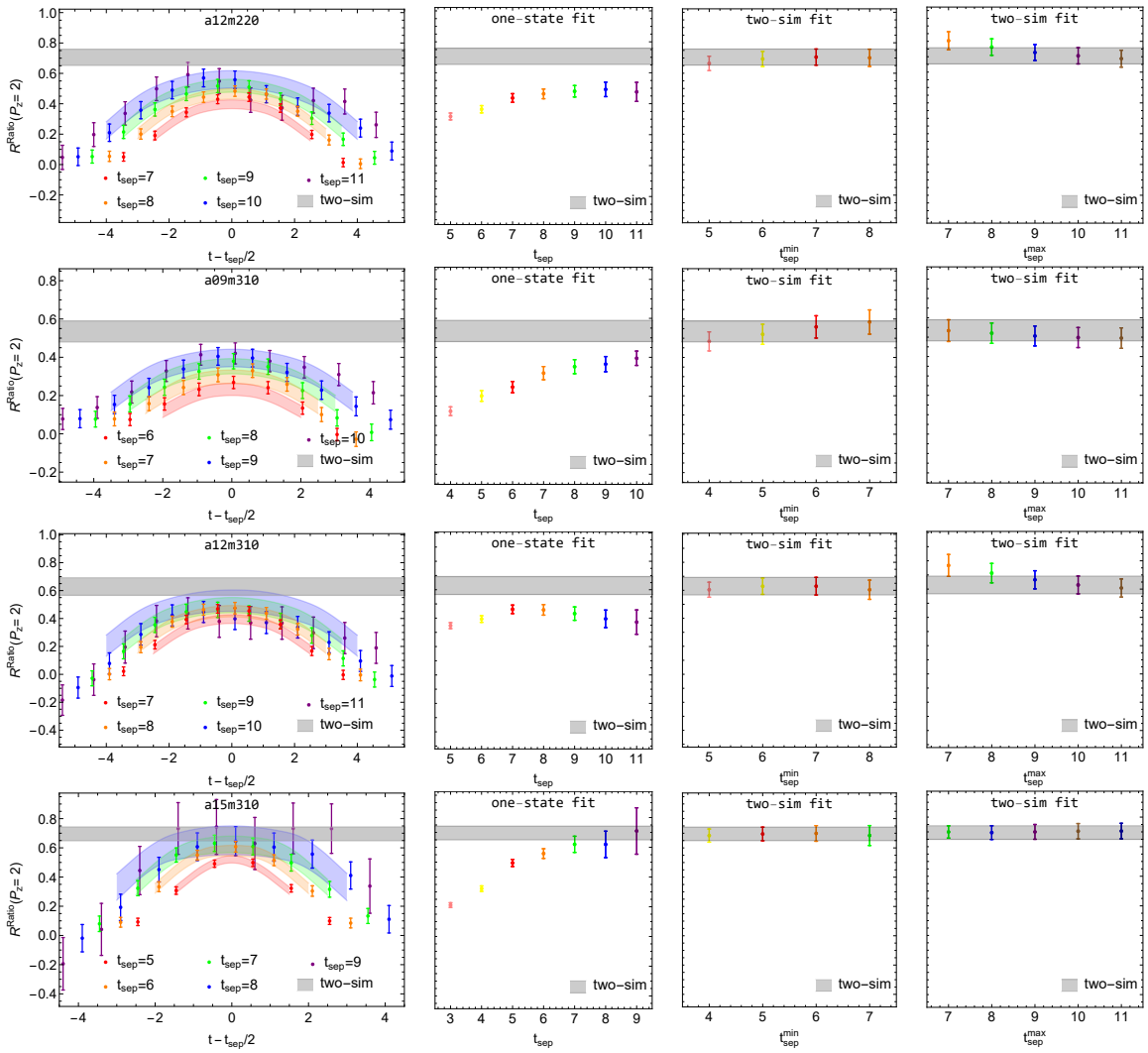

Figure 52 Example ratio plots (left), one-state fits (second column) and two-sim fits (last 2 columns) from the a12m220, a09m310, a12m310, a15m310 ensembles light nucleon correlators from top to bottom, at pion masses $M_\pi \approx \{220, 310, 310, 310\}$ MeV. The gray band shown on all plots is the extracted ground-state matrix element from the two-sim fit using $t_{\text{sep}} \in [5, 8]$. From left to right, the columns are: the ratio of the three-point to two-point correlators with the reconstructed fit bands from the two-sim fit using $t_{\text{sep}} \in [5, 8]$, shown as functions of $t - t_{\text{sep}}/2$, the one-state fit results for the three-point correlators at each $t_{\text{sep}} \in [3, 9]$, the two-sim fit results using $t_{\text{sep}} \in [t_{\text{sep}}^{\text{min}}, 8]$ as functions of $t_{\text{sep}}^{\text{min}}$, and the two-sim fit results using $t_{\text{sep}} \in [5, t_{\text{sep}}^{\text{max}}]$ as functions of $t_{\text{sep}}^{\text{max}}$.

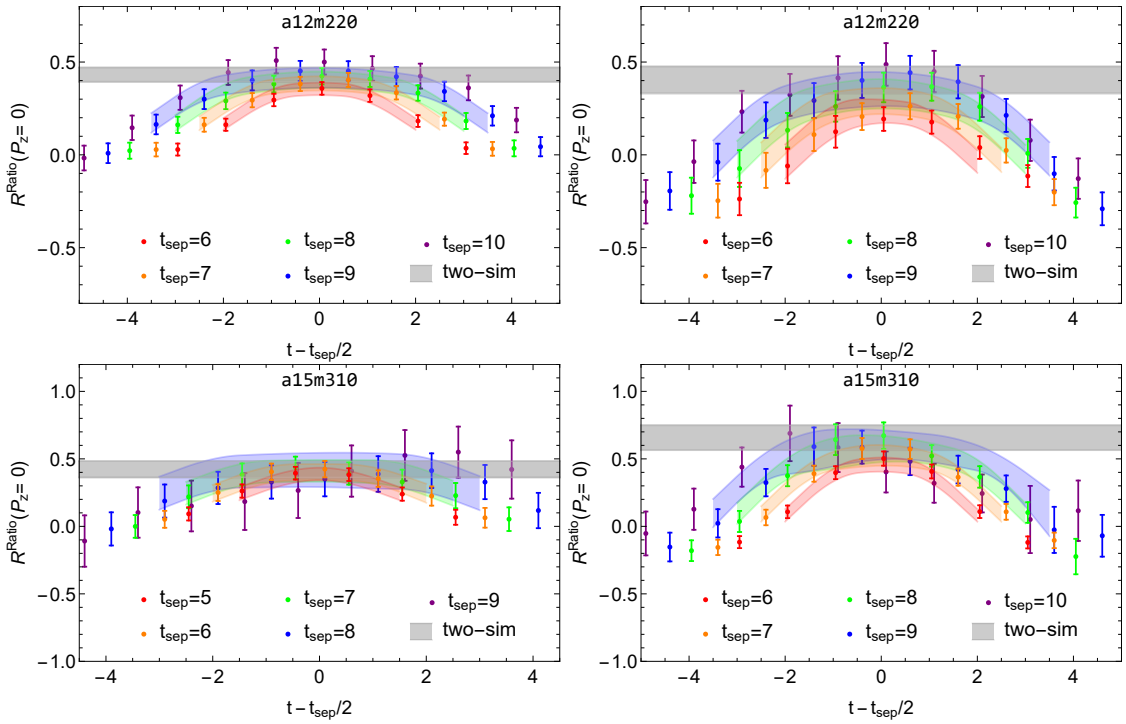

Figure 53 Example ratio plots from the a15m310 light nucleon correlators at pion masses $M_\pi \approx 310$ MeV from momentum smearing parameter $\mathbf{k} \neq 0$ listed in Tab. 7 and $\mathbf{k} = 0$ from the PNDME collaboration from left to right, respectively.

.0.5. Bare gluon momentum fraction

.0.5.1 Strange Nucleon

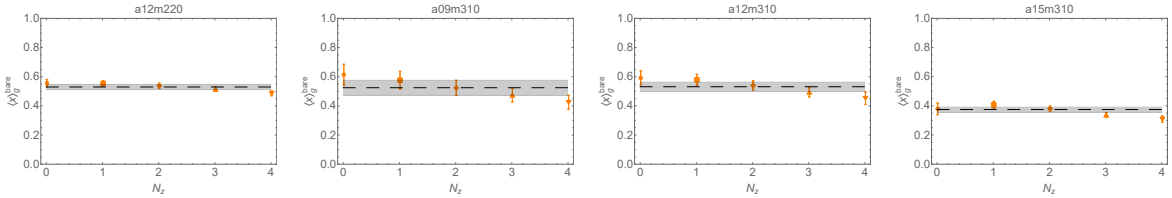

Figure 54 The bare gluon momentum fraction $\langle x \rangle_g^{\text{bare}}$ and fitted bands normalization by kinematic factors as functions of momentum $P_z = 2\pi \times N_z/L$ for $M_\pi \approx \{700, 690, 690, 690\}$ MeV on a12m220, a09m310, a12m310, a15m310 ensembles respectively.

.0.5.2 Light Nucleon

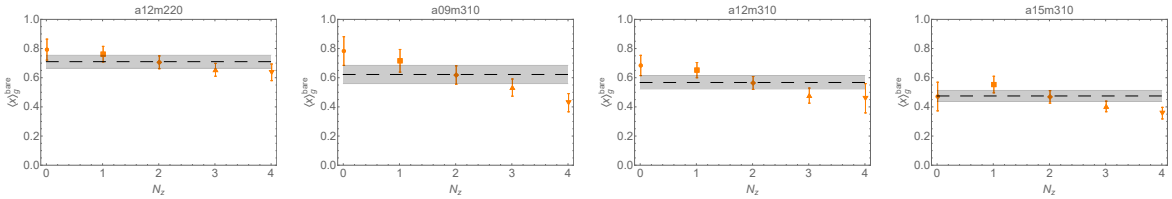

Figure 55 The bare gluon momentum fraction $\langle x \rangle_g^{\text{bare}}$ and fitted bands normalization by kinematic factors as functions of momentum $P_z = 2\pi \times N_z/L$ for $M_\pi \approx \{220, 310, 310, 310\}$ MeV on a12m220, a09m310, a12m310, a15m310 ensembles respectively.

.0.6. Bare Matrix Elements

.0.6.1 Strange Nucleon

Figures. 56 show the fitted bare ground-state matrix elements without normalization by kinematic factors as functions of z obtained from the two-sim fit for $M_\pi \approx \{700, 690, 690, 690\}$ MeV on a12m220, a09m310, a12m310, a15m310 ensembles respectively.

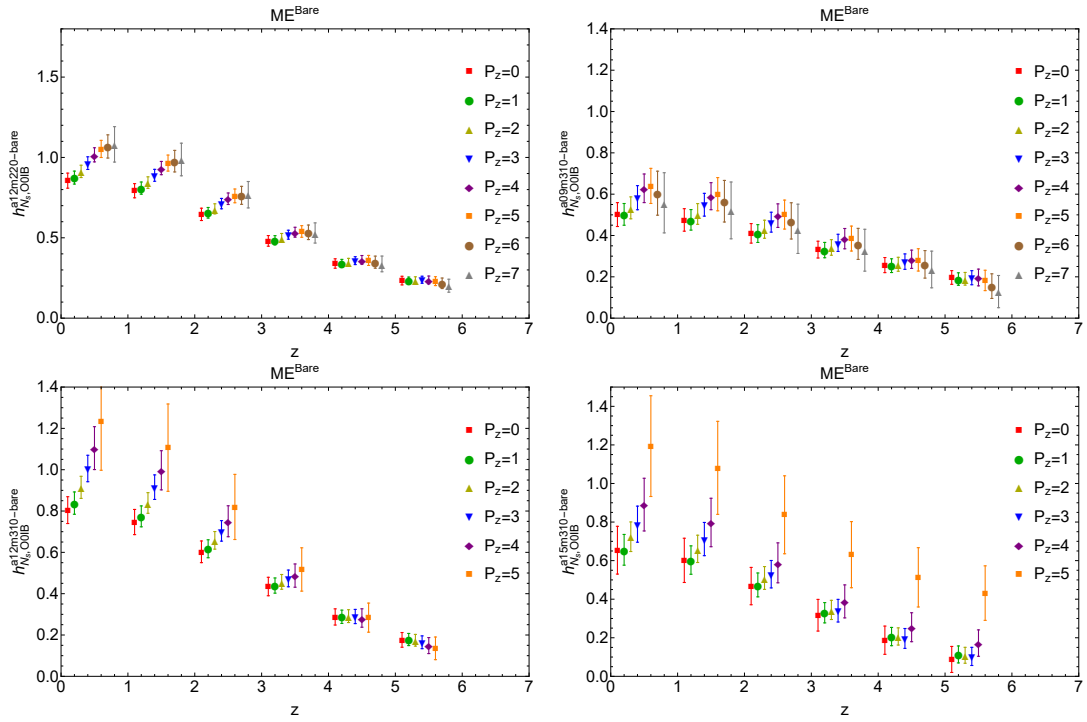

Figure 56 The fitted bare ground-state matrix elements without normalization by kinematic factors as functions of z obtained from the two-sim fit for $M_\pi \approx \{700, 690, 690, 690\}$ MeV on a12m220, a09m310, a12m310, a15m310 ensembles respectively.

.0.6.2 Light Nucleon

Figures. 57 show the fitted bare ground-state matrix elements without normalization by kinematic factors as functions of z obtained from the two-sim fit for $M_\pi \approx \{220, 310, 310, 310\}$ MeV on a12m220, a09m310, a12m310, a15m310 ensembles respectively. respectively.

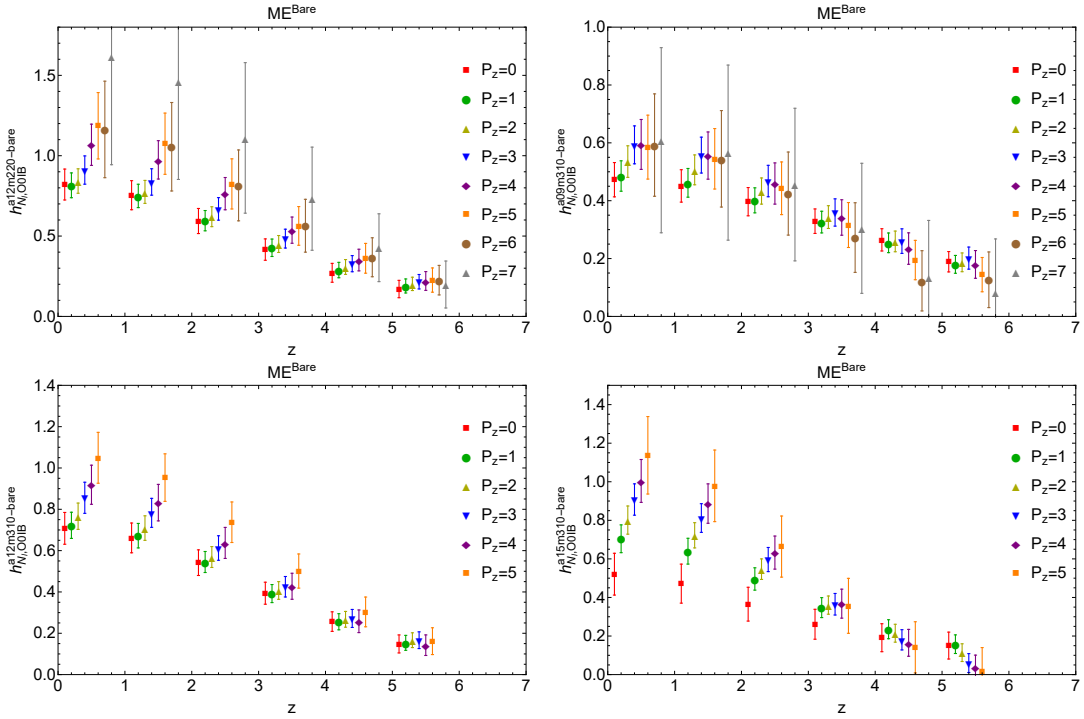

Figure 57 The fitted bare ground-state matrix elements without normalization by kinematic factors as functions of z obtained from the two-sim fit for $M_\pi \approx \{220, 310, 310, 310\}$ MeV on a12m220, a09m310, a12m310, a15m310 ensembles respectively.

.0.7. Lattice Spacing Dependence on RpITD

.0.7.1 Strange Nucleon

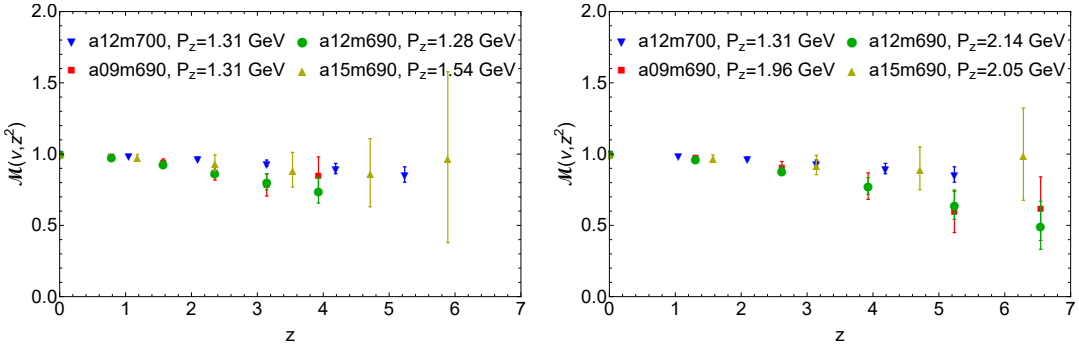

Figure 58 The RpITDs at boost momenta $P_z \approx 2$ GeV and 1.3 GeV as functions of ν obtained from the fitted bare ground-state matrix elements for $M_\pi \approx \{700, 690, 690, 690\}$ MeV on a12m220, a09m310, a12m310, a15m310 ensembles respectively.

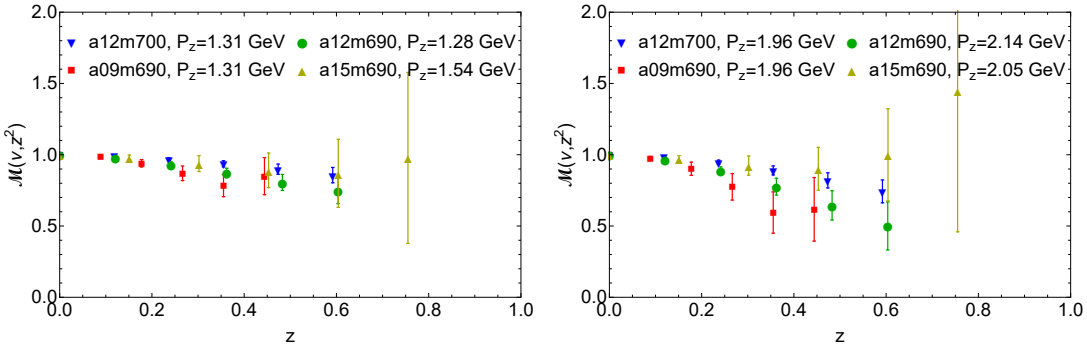

Figure 59 The RpITDs at boost momenta $P_z \approx 2$ GeV and 1.3 GeV as functions of s obtained from the fitted bare ground-state matrix elements for $M_\pi \approx \{700, 690, 690, 690\}$ MeV on a12m220, a09m310, a12m310, a15m310 ensembles respectively.

.0.7.2 Light Nucleon

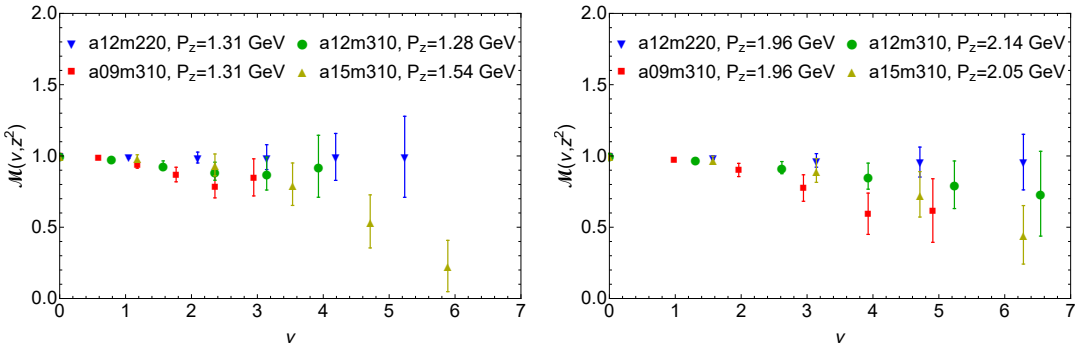

Figure 60 The RpITDs at boost momenta $P_z \approx 2$ GeV and 1.3 GeV as functions of ν obtained from the fitted bare ground-state matrix elements for $M_\pi \approx \{220, 310, 310, 310\}$ MeV on a12m220, a09m310, a12m310, a15m310 ensembles respectively.

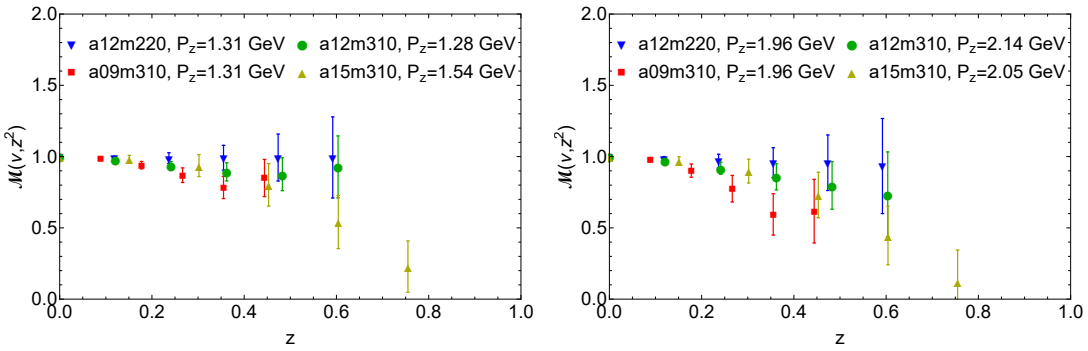

Figure 61 The RpITDs at boost momenta $P_z \approx 2$ GeV and 1.3 GeV as functions of z obtained from the fitted bare ground-state matrix elements for $M_\pi \approx \{220, 310, 310, 310\}$ MeV on a12m220, a09m310, a12m310, a15m310 ensembles respectively.

.0.8. z_{cut}-dependent fits

Figures. 62 and 63 show the RpITD fit in Eq. V.14 with different fit range $z \in [0, z_{\text{cut}}]$, with the χ^2/dof of each fit listed in the plot legends.

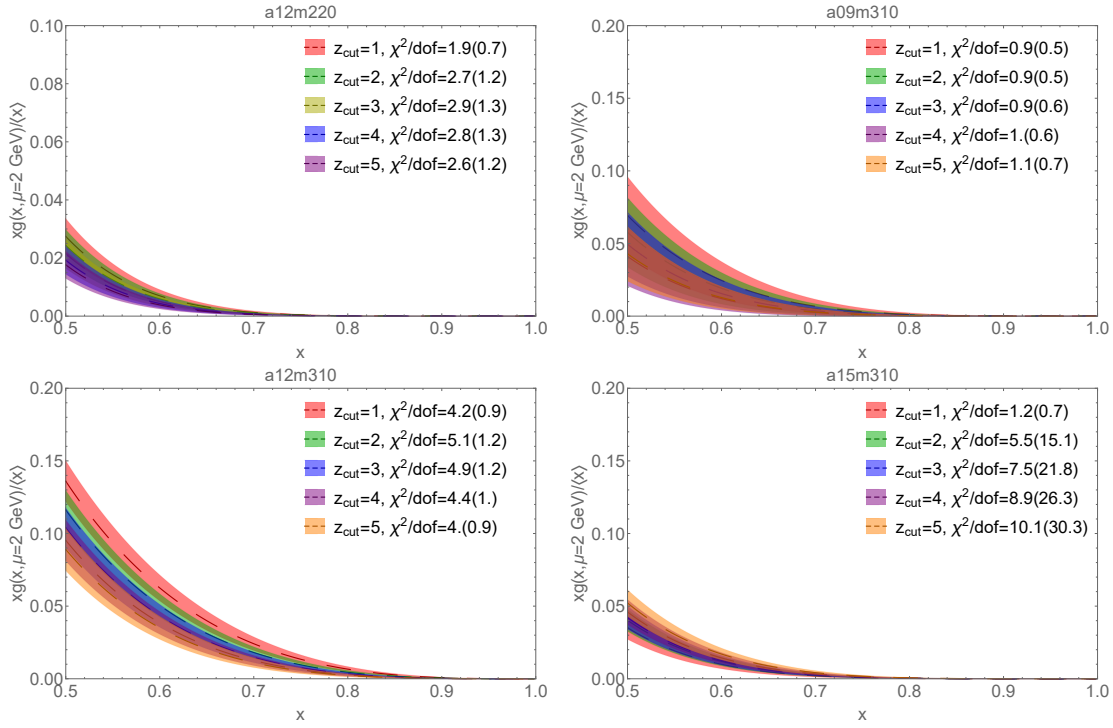

Figure 62 RpITD fits in Eq. V.14 with different fit range $z \in [0, z_{\text{cut}}]$ for $M_\pi \approx \{700, 690, 690, 690\}$ MeV on a12m220, a09m310, a12m310, a15m310 ensembles respectively. The χ^2/dof of the fits are listed in the plot legends.

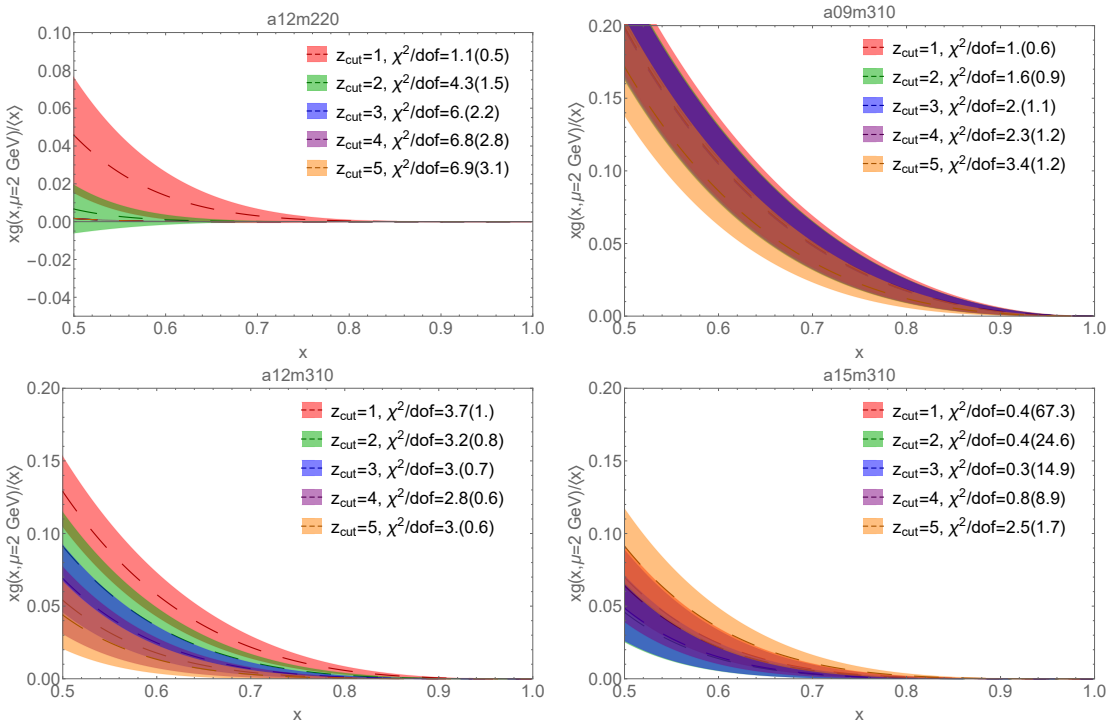

Figure 63 RpITD fits in Eq. V.14 with different fit range $z \in [0, z_{\text{cut}}]$ for $M_\pi \approx \{220, 310, 310, 310\}$ MeV on a12m220, a09m310, a12m310, a15m310 ensembles respectively. The χ^2/dof of the fits are listed in the plot legends.

BIBLIOGRAPHY

BIBLIOGRAPHY

[1] Robert G. Edwards and Balint Joo. The Chroma software system for lattice QCD. *Nucl. Phys. B Proc. Suppl.*, 140:832, 2005.

[2] Tie-Jiun Hou et al. New CTEQ global analysis of quantum chromodynamics with high-precision data from the LHC. 12 2019.

[3] Ivan Novikov et al. Parton Distribution Functions of the Charged Pion Within The xFitter Framework. *Phys. Rev. D*, 102(1):014040, 2020.

[4] P. C. Barry, N. Sato, W. Melnitchouk, and Chueng-Ryong Ji. First Monte Carlo Global QCD Analysis of Pion Parton Distributions. *Phys. Rev. Lett.*, 121(15):152001, 2018.

[5] M. Gluck, E. Reya, and A. Vogt. Pionic parton distributions. *Z. Phys. C*, 53:651–656, 1992.

[6] Jiunn-Wei Chen, Luchang Jin, Huey-Wen Lin, Yu-Sheng Liu, Yi-Bo Yang, Jian-Hui Zhang, and Yong Zhao. Lattice Calculation of Parton Distribution Function from LaMET at Physical Pion Mass with Large Nucleon Momentum. 2018.

[7] Huey-Wen Lin, Jiunn-Wei Chen, Xiangdong Ji, Luchang Jin, Ruizi Li, Yu-Sheng Liu, Yi-Bo Yang, Jian-Hui Zhang, and Yong Zhao. Proton Isovector Helicity Distribution on the Lattice at Physical Pion Mass. *Phys. Rev. Lett.*, 121(24):242003, 2018.

[8] Yu-Sheng Liu, Jiunn-Wei Chen, Luchang Jin, Ruizi Li, Huey-Wen Lin, Yi-Bo Yang, Jian-Hui Zhang, and Yong Zhao. Nucleon Transversity Distribution at the Physical Pion Mass from Lattice QCD. 2018.

[9] Constantia Alexandrou, Krzysztof Cichy, Martha Constantinou, Karl Jansen, Aurora Scapellato, and Fernanda Steffens. Light-Cone Parton Distribution Functions from Lattice QCD. *Phys. Rev. Lett.*, 121(11):112001, 2018.

[10] Constantia Alexandrou, Krzysztof Cichy, Martha Constantinou, Karl Jansen, Aurora Scapellato, and Fernanda Steffens. Transversity parton distribution functions from lattice QCD. *Phys. Rev.*, D98(9):091503, 2018.

[11] Constantia Alexandrou, Krzysztof Cichy, Martha Constantinou, Kyriakos Hadjiyiannakou, Karl Jansen, Aurora Scapellato, and Fernanda Steffens. Systematic uncertainties in parton distribution functions from lattice QCD simulations at the physical point. *Phys. Rev. D*, 99(11):114504, 2019.

[12] Manjunath Bhat, Krzysztof Cichy, Martha Constantinou, and Aurora Scapellato. Parton distribution functions from lattice QCD at physical quark masses via the pseudo-distribution approach. 5 2020.

[13] Bálint Joó, Joseph Karpie, Kostas Orginos, Anatoly V. Radyushkin, David G. Richards, and Savvas Zafeiropoulos. Parton Distribution Functions from Ioffe time pseudo-distributions from lattice caclulations; approaching the physical point. 4 2020.

[14] S. Alekhin, J. Blümlein, S. Moch, and R. Placakyte. Parton distribution functions, α_s, and heavy-quark masses for LHC Run II. *Phys. Rev. D*, 96(1):014011, 2017.

[15] Richard D. Ball et al. Parton distributions from high-precision collider data. *Eur. Phys. J.*, C77(10):663, 2017.

[16] A. Accardi, L. T. Brady, W. Melnitchouk, J. F. Owens, and N. Sato. Constraints on large-x parton distributions from new weak boson production and deep-inelastic scattering data. *Phys. Rev.*, D93(11):114017, 2016.

[17] Daniel de Florian, Rodolfo Sassot, Marco Stratmann, and Werner Vogelsang. Extraction of Spin-Dependent Parton Densities and Their Uncertainties. *Phys. Rev. D*, 80:034030, 2009.

[18] Emanuele R. Nocera, Richard D. Ball, Stefano Forte, Giovanni Ridolfi, and Juan Rojo. A first unbiased global determination of polarized PDFs and their uncertainties. *Nucl. Phys.*, B887:276–308, 2014.

[19] J. J. Ethier, N. Sato, and W. Melnitchouk. First simultaneous extraction of spin-dependent parton distributions and fragmentation functions from a global QCD analysis. *Phys. Rev. Lett.*, 119(13):132001, 2017.

[20] Huey-Wen Lin, W. Melnitchouk, Alexei Prokudin, N. Sato, and H. Shows. First Monte Carlo Global Analysis of Nucleon Transversity with Lattice QCD Constraints. *Phys. Rev. Lett.*, 120(15):152502, 2018.

[21] Marco Radici and Alessandro Bacchetta. First Extraction of Transversity from a Global Analysis of Electron-Proton and Proton-Proton Data. *Phys. Rev. Lett.*, 120(19):192001, 2018.

[22] J. Benel, A. Courtoy, and R. Ferro-Hernandez. A constrained fit of the valence transversity distributions from dihadron production. *Eur. Phys. J. C*, 80(5):465, 2020.

[23] Martha Constantinou et al. Parton distributions and lattice-QCD calculations: Toward 3D structure. *Prog. Part. Nucl. Phys.*, 121:103908, 2021.

[24] N. Y. Cao, P. C. Barry, N. Sato, and W. Melnitchouk. Towards the 3-dimensional parton structure of the pion: integrating transverse momentum data into global QCD analysis. 3 2021.

[25] Zhu-Fang Cui, Minghui Ding, Fei Gao, Khépani Raya, Daniele Binosi, Lei Chang, Craig D Roberts, Jose Rodríguez-Quintero, and Sebastian M Schmidt. Kaon and pion parton distributions. *Eur. Phys. J. C*, 80(11):1064, 2020.

[26] Sayipjamal Dulat, Tie-Jiun Hou, Jun Gao, Marco Guzzi, Joey Huston, Pavel Nadolsky, Jon Pumplin, Carl Schmidt, Daniel Stump, and C. P. Yuan. New parton distribution functions from a global analysis of quantum chromodynamics. *Phys. Rev.*, D93(3):033006, 2016.

[27] Jon Butterworth et al. PDF4LHC recommendations for LHC Run II. *J. Phys. G*, 43:023001, 2016.

[28] Santanu Mondal, Rajan Gupta, Sungwoo Park, Boram Yoon, Tanmoy Bhattacharya, and Huey-Wen Lin. Moments of nucleon isovector structure functions in $2 + 1 + 1$-flavor QCD. *Phys. Rev. D*, 102(5):054512, 2020.

[29] Yi-Bo Yang, Raza Sabbir Sufian, Andrei Alexandru, Terrence Draper, Michael J. Glatzmaier, Keh-Fei Liu, and Yong Zhao. Glue Spin and Helicity in the Proton from Lattice QCD. *Phys. Rev. Lett.*, 118(10):102001, 2017.

[30] Yi-Bo Yang, Ming Gong, Jian Liang, Huey-Wen Lin, Keh-Fei Liu, Dimitra Pefkou, and Phiala Shanahan. Nonperturbatively renormalized glue momentum fraction at the physical pion mass from lattice QCD. *Phys. Rev. D*, 98(7):074506, 2018.

[31] Phiala Shanahan. The gluon structure of hadrons and nuclei from lattice QCD. *EPJ Web Conf.*, 175:01015, 2018.

[32] Michal Czakon, Michelangelo L. Mangano, Alexander Mitov, and Juan Rojo. Constraints on the gluon PDF from top quark pair production at hadron colliders. *JHEP*, 07:167, 2013.

[33] Rhorry Gauld, Juan Rojo, Luca Rottoli, and Jim Talbert. Charm production in the forward region: constraints on the small-x gluon and backgrounds for neutrino astronomy. *JHEP*, 11:009, 2015.

[34] J Currie, E. W. N. Glover, and J Pires. Next-to-Next-to Leading Order QCD Predictions for Single Jet Inclusive Production at the LHC. *Phys. Rev. Lett.*, 118(7):072002, 2017.

[35] Michał Czakon, Nathan P. Hartland, Alexander Mitov, Emanuele R. Nocera, and Juan Rojo. Pinning down the large-x gluon with NNLO top-quark pair differential distributions. *JHEP*, 04:044, 2017.

[36] Marco Guzzi, Katerina Lipka, and Sven-Olaf Moch. Top-quark pair production at hadron colliders: differential cross section and phenomenological applications with DiffTop. *JHEP*, 01:082, 2015.

[37] John M. Campbell, R. Keith Ellis, and Ciaran Williams. Direct Photon Production at Next-to–Next-to-Leading Order. *Phys. Rev. Lett.*, 118(22):222001, 2017. [Erratum: Phys.Rev.Lett. 124, 259901 (2020)].

[38] H. Abramowicz et al. Combination of measurements of inclusive deep inelastic $e^{\pm}p$ scattering cross sections and QCD analysis of HERA data. *Eur. Phys. J. C*, 75(12):580, 2015.

[39] Oleksandr Zenaiev et al. Impact of heavy-flavour production cross sections measured by the LHCb experiment on parton distribution functions at low x. *Eur. Phys. J. C*, 75(8):396, 2015.

[40] Rhorry Gauld and Juan Rojo. Precision determination of the small-x gluon from charm production at LHCb. *Phys. Rev. Lett.*, 118(7):072001, 2017.

[41] Radja Boughezal, Alberto Guffanti, Frank Petriello, and Maria Ubiali. The impact of the LHC Z-boson transverse momentum data on PDF determinations. *JHEP*, 07:130, 2017.

[42] A. Accardi et al. Electron Ion Collider: The Next QCD Frontier: Understanding the glue that binds us all. *Eur. Phys. J. A*, 52(9):268, 2016.

[43] J. Arrington et al. Revealing the structure of light pseudoscalar mesons at the Electron-Ion Collider. 2 2021.

[44] Arlene C. Aguilar et al. Pion and Kaon Structure at the Electron-Ion Collider. *Eur. Phys. J. A*, 55(10):190, 2019.

[45] Daniele P. Anderle et al. Electron-Ion Collider in China. 2 2021.

[46] Richard D. Ball et al. Parton distributions from high-precision collider data. *Eur. Phys. J. C*, 77(10):663, 2017.

[47] L. A. Harland-Lang, A. D. Martin, P. Motylinski, and R. S. Thorne. Parton distributions in the LHC era: MMHT 2014 PDFs. *Eur. Phys. J. C*, 75(5):204, 2015.

[48] N. Sato, C. Andres, J. J. Ethier, and W. Melnitchouk. Strange quark suppression from a simultaneous Monte Carlo analysis of parton distributions and fragmentation functions. *Phys. Rev. D*, 101(7):074020, 2020.

[49] Amanda M. Cooper-Sarkar. HERAPDF2.0Jets NNLO (prel.), the completion ofthe HERAPDF2.0 family. *PoS*, DIS2019:029, 2019.

[50] J. F. Owens. Q**2 Dependent Parametrizations of Pion Parton Distribution Functions. *Phys. Rev. D*, 30:943, 1984.

[51] P. Aurenche, R. Baier, M. Fontannaz, M. N. Kienzle-Focacci, and M. Werlen. The Gluon Content of the Pion From High p_T Direct Photon Production. *Phys. Lett. B*, 233:517–521, 1989.

[52] P. J. Sutton, Alan D. Martin, R. G. Roberts, and W. James Stirling. Parton distributions for the pion extracted from Drell-Yan and prompt photon experiments. *Phys. Rev. D*, 45:2349–2359, 1992.

[53] M. Gluck, E. Reya, and I. Schienbein. Pionic parton distributions revisited. *Eur. Phys. J. C*, 10:313–317, 1999.

[54] Claude Bourrely and Jacques Soffer. Statistical approach of pion parton distributions from Drell–Yan process. *Nucl. Phys. A*, 981:118–129, 2019.

[55] Wen-Chen Chang, Jen-Chieh Peng, Stephane Platchkov, and Takahiro Sawada. Constraining gluon density of pions at large x by pion-induced J/ψ production. *Phys. Rev. D*, 102(5):054024, 2020.

[56] Kenneth G. Wilson. Confinement of Quarks. *Phys. Rev. D*, 10:2445–2459, 1974.

[57] Kenneth G. Wilson. Quarks and Strings on a Lattice. In *13th International School of Subnuclear Physics: New Phenomena in Subnuclear Physics*, 11 1975.

[58] M. Luscher and P. Weisz. On-Shell Improved Lattice Gauge Theories. *Commun. Math. Phys.*, 97:59, 1985. [Erratum: Commun.Math.Phys. 98, 433 (1985)].

[59] B. Sheikholeslami and R. Wohlert. Improved Continuum Limit Lattice Action for QCD with Wilson Fermions. *Nucl. Phys. B*, 259:572, 1985.

[60] Martin Luscher, Stefan Sint, Rainer Sommer, and Peter Weisz. Chiral symmetry and O(a) improvement in lattice QCD. *Nucl. Phys. B*, 478:365–400, 1996.

[61] Gerard 't Hooft, C. Itzykson, A. Jaffe, H. Lehmann, P. K. Mitter, I. M. Singer, and R. Stora, editors. *Recent Developments in Gauge Theories. Proceedings, Nato Advanced Study Institute, Cargese, France, August 26 - September 8, 1979*, volume 59, 1980.

[62] Y. Iwasaki. Renormalization Group Analysis of Lattice Theories and Improved Lattice Action. II. Four-dimensional non-Abelian SU(N) gauge model. 12 1983.

[63] A. Bazavov et al. Scaling studies of QCD with the dynamical HISQ action. *Phys. Rev. D*, 82:074501, 2010.

[64] A. Bazavov et al. Lattice QCD Ensembles with Four Flavors of Highly Improved Staggered Quarks. *Phys. Rev.*, D87(5):054505, 2013.

[65] Chulwoo Jung. Nucleon mass and strange content from (2+1)-flavor Domain Wall Fermion. *PoS*, LATTICE2012:164, 2012.

[66] Kostas Orginos and Doug Toussaint. Testing improved actions for dynamical Kogut-Susskind quarks. *Phys. Rev. D*, 59:014501, 1999.

[67] G. Peter Lepage. Flavor symmetry restoration and Symanzik improvement for staggered quarks. *Phys. Rev. D*, 59:074502, 1999.

[68] G. Peter Lepage and Paul B. Mackenzie. On the viability of lattice perturbation theory. *Phys. Rev. D*, 48:2250–2264, 1993.

[69] G. Peter Lepage. Simulating heavy quarks. *Nucl. Phys. B Proc. Suppl.*, 26:45–56, 1992.

[70] G. Peter Lepage. Redesigning lattice QCD. *Lect. Notes Phys.*, 479:1–48, 1997.

[71] E. Follana, Q. Mason, C. Davies, K. Hornbostel, G. P. Lepage, J. Shigemitsu, H. Trottier, and K. Wong. Highly improved staggered quarks on the lattice, with applications to charm physics. *Phys. Rev. D*, 75:054502, 2007.

[72] C. T. H. Davies et al. High precision lattice QCD confronts experiment. *Phys. Rev. Lett.*, 92:022001, 2004.

[73] Wolfgang Bietenholz, Philippe de Forcrand, Urs Gerber, Héctor Mejía-Díaz, and Ilya O. Sandoval. Topological Susceptibility of the 2d O(3) Model under Gradient Flow. *Phys. Rev. D*, 98(11):114501, 2018.

[74] A. Bazavov et al. Nonperturbative QCD Simulations with 2+1 Flavors of Improved Staggered Quarks. *Rev. Mod. Phys.*, 82:1349–1417, 2010.

[75] Rajamani Narayanan and Herbert Neuberger. Infinitely many regulator fields for chiral fermions. *Phys. Lett. B*, 302:62–69, 1993.

[76] Rajamani Narayanan and Herbert Neuberger. A Construction of lattice chiral gauge theories. *Nucl. Phys. B*, 443:305–385, 1995.

[77] Shung-ichi Ando and Dong-Pil Min. Radiative muon capture in heavy baryon chiral perturbation theory. *Phys. Lett. B*, 417:177–185, 1998.

[78] Herbert Neuberger. More about exactly massless quarks on the lattice. *Phys. Lett. B*, 427:353–355, 1998.

[79] David B. Kaplan. A Method for simulating chiral fermions on the lattice. *Phys. Lett. B*, 288:342–347, 1992.

[80] Yigal Shamir. Chiral fermions from lattice boundaries. *Nucl. Phys. B*, 406:90–106, 1993.

[81] Albert M Sirunyan et al. Observation of a New Excited Beauty Strange Baryon Decaying to$\Xi_b^- \pi^+ \pi^-$. *Phys. Rev. Lett.*, 126(25):252003, 2021.

[82] Vadim Furman and Yigal Shamir. Axial symmetries in lattice QCD with Kaplan fermions. *Nucl. Phys. B*, 439:54–78, 1995.

[83] Maxwell T. Hansen and Stephen R. Sharpe. Threshold expansion of the three-particle quantization condition. *Phys. Rev. D*, 93(9):096006, 2016. [Erratum: Phys.Rev.D 96, 039901 (2017)].

[84] Roberto Frezzotti, Pietro Antonio Grassi, Stefan Sint, and Peter Weisz. A Local formulation of lattice QCD without unphysical fermion zero modes. *Nucl. Phys. B Proc. Suppl.*, 83:941–946, 2000.

[85] Roberto Frezzotti, Pietro Antonio Grassi, Stefan Sint, and Peter Weisz. Lattice QCD with a chirally twisted mass term. *JHEP*, 08:058, 2001.

[86] K. C. Bowler, B. Joo, R. D. Kenway, C. M. Maynard, and R. J. Tweedie. Lattice QCD with mixed actions. *JHEP*, 08:003, 2005.

[87] A. Bazavov et al. Lattice QCD Ensembles with Four Flavors of Highly Improved Staggered Quarks. *Phys. Rev. D*, 87(5):054505, 2013.

[88] M. Albanese et al. Glueball Masses and String Tension in Lattice QCD. *Phys. Lett. B*, 192:163–169, 1987.

[89] Anna Hasenfratz and Francesco Knechtli. Flavor symmetry and the static potential with hypercubic blocking. *Phys. Rev. D*, 64:034504, 2001.

[90] A. Hasenfratz, R. Hoffmann, and F. Knechtli. The Static potential with hypercubic blocking. *Nucl. Phys. B Proc. Suppl.*, 106:418–420, 2002.

[91] Colin Morningstar and Mike J. Peardon. Analytic smearing of SU(3) link variables in lattice QCD. *Phys. Rev. D*, 69:054501, 2004.

[92] S. Gusken, U. Low, K. H. Mutter, R. Sommer, A. Patel, and K. Schilling. Nonsinglet Axial Vector Couplings of the Baryon Octet in Lattice QCD. *Phys. Lett. B*, 227:266–269, 1989.

[93] S. Gusken. A Study of smearing techniques for hadron correlation functions. *Nucl. Phys. B Proc. Suppl.*, 17:361–364, 1990.

[94] C. Alexandrou, F. Jegerlehner, S. Gusken, K. Schilling, and R. Sommer. B meson properties from lattice QCD. *Phys. Lett. B*, 256:60–67, 1991.

[95] S. Collins. Gauge invariant smearing and the extraction of excited state masses using Wilson fermions at beta = 6.2. *Nucl. Phys. B Proc. Suppl.*, 30:393–396, 1993.

[96] C. R. Allton et al. Gauge invariant smearing and matrix correlators using Wilson fermions at Beta = 6.2. *Phys. Rev. D*, 47:5128–5137, 1993.

[97] P. Lacock, A. McKerrell, Christopher Michael, I. M. Stopher, and P. W. Stephenson. Efficient hadronic operators in lattice gauge theory. *Phys. Rev. D*, 51:6403–6410, 1995.

[98] P Boyle. A Novel gauge invariant multistate smearing technique. *J. Comput. Phys.*, 179:349–370, 2002.

[99] Georg M. von Hippel, Benjamin Jäger, Thomas D. Rae, and Hartmut Wittig. The Shape of Covariantly Smeared Sources in Lattice QCD. *JHEP*, 09:014, 2013.

[100] P. Bacilieri et al. The Hadronic Mass Spectrum in Quenched Lattice QCD: Results at Beta = 5.7 and Beta = 6.0. *Phys. Lett. B*, 214:115–119, 1988.

[101] William Detmold, Kostas Orginos, and Zhifeng Shi. Lattice QCD at non-zero isospin chemical potential. *Phys. Rev. D*, 86:054507, 2012.

[102] C. R. Allton, Christopher T. Sachrajda, V. Lubicz, L. Maiani, and G. Martinelli. A lattice computation of the decay constant of the B meson. *Nucl. Phys. B*, 349:598–616, 1991.

[103] Thomas A. DeGrand and Richard D. Loft. Wave function tests for lattice QCD spectroscopy. *Comput. Phys. Commun.*, 65:84–91, 1991.

[104] Thomas A. DeGrand and Matthew Hecht. Observation of orbitally excited hadrons in simulations of lattice QCD. *Phys. Lett. B*, 275:435–440, 1992.

[105] Dale S. Roberts, Waseem Kamleh, Derek B. Leinweber, M. S. Mahbub, and Benjamin J. Menadue. Accessing High Momentum States In Lattice QCD. *Phys. Rev. D*, 86:074504, 2012.

[106] Michele Della Morte, Benjamin Jaeger, Thomas Rae, and Hartmut Wittig. Improved interpolating fields for hadrons at non-zero momentum. *Eur. Phys. J. A*, 48:139, 2012.

[107] Gunnar S. Bali, Bernhard Lang, Bernhard U. Musch, and Andreas Schäfer. Novel quark smearing for hadrons with high momenta in lattice QCD. *Phys. Rev.*, D93(9):094515, 2016.

[108] Magnus Rudolph Hestenes, Eduard Stiefel, et al. *Methods of conjugate gradients for solving linear systems*, volume 49. NBS Washington, DC, 1952.

[109] Christopher C Paige and Michael A Saunders. Solution of sparse indefinite systems of linear equations. *SIAM journal on numerical analysis*, 12(4):617–629, 1975.

[110] Roger Fletcher. Conjugate gradient methods for indefinite systems. In *Numerical analysis*, pages 73–89. Springer, 1976.

[111] R. Babich, J. Brannick, R.C. Brower, M.A. Clark, T.A. Manteuffel, S.F. McCormick, J.C. Osborn, and C. Rebbi. Adaptive multigrid algorithm for the lattice Wilson-Dirac operator. *Phys. Rev. Lett.*, 105:201602, 2010.

[112] J.C. Osborn, R. Babich, J. Brannick, R.C. Brower, M.A. Clark, S.D. Cohen, and C. Rebbi. Multigrid solver for clover fermions. *PoS*, LATTICE2010:037, 2010.

[113] Rajamani Narayanan. A derivation of the CG algorithm for a shifted matrix. 1998.

[114] Marco Bochicchio, Luciano Maiani, Guido Martinelli, Gian Carlo Rossi, and Massimo Testa. Chiral Symmetry on the Lattice with Wilson Fermions. *Nucl. Phys. B*, 262:331, 1985.

[115] L. Maiani and G. Martinelli. Current Algebra and Quark Masses from a Monte Carlo Simulation with Wilson Fermions. *Phys. Lett. B*, 178:265–271, 1986.

[116] L. Maiani, G. Martinelli, G. C. Rossi, and M. Testa. The Octet Nonleptonic Hamiltonian and Current Algebra on the Lattice With Wilson Fermions. *Nucl. Phys. B*, 289:505–534, 1987.

[117] L. Maiani, G. Martinelli, G. C. Rossi, and M. Testa. The weak hamiltonian on the lattice. *Phys. Lett. B*, 176:445–448, 1986.

[118] G. Martinelli, C. Pittori, Christopher T. Sachrajda, M. Testa, and A. Vladikas. A General method for nonperturbative renormalization of lattice operators. *Nucl. Phys. B*, 445:81–108, 1995.

[119] Guido Altarelli, G. Curci, G. Martinelli, and S. Petrarca. QCD Nonleading Corrections to Weak Decays as an Application of Regularization by Dimensional Reduction. *Nucl. Phys. B*, 187:461–513, 1981.

[120] Andrzej J. Buras, Matthias Jamin, Markus E. Lautenbacher, and Peter H. Weisz. Two loop anomalous dimension matrix for $\Delta S = 1$ weak nonleptonic decays I: $\mathcal{O}(\alpha_s^2)$. *Nucl. Phys. B*, 400:37–74, 1993.

[121] K. G. Chetyrkin and A. Retey. Renormalization and running of quark mass and field in the regularization invariant and MS-bar schemes at three loops and four loops. *Nucl. Phys. B*, 583:3–34, 2000.

[122] Aleksey I. Alekseev. Strong coupling constant to four loops in the analytic approach to QCD. *Few Body Syst.*, 32:193–217, 2003.

[123] T. van Ritbergen, J. A. M. Vermaseren, and S. A. Larin. The Four loop beta function in quantum chromodynamics. *Phys. Lett. B*, 400:379–384, 1997.

[124] John C. Collins and Randall J. Scalise. The Renormalization of composite operators in Yang-Mills theories using general covariant gauge. *Phys. Rev. D*, 50:4117–4136, 1994.

[125] Yi-Bo Yang, Michael Glatzmaier, Keh-Fei Liu, and Yong Zhao. The 1-loop correction of the QCD energy momentum tensor with the overlap fermion and HYP smeared Iwasaki gluon. 12 2016.

[126] Florian Herren and Matthias Steinhauser. Version 3 of RunDec and CRunDec. *Comput. Phys. Commun.*, 224:333–345, 2018.

[127] Barbara Schmidt and Matthias Steinhauser. CRunDec: a C++ package for running and decoupling of the strong coupling and quark masses. *Comput. Phys. Commun.*, 183:1845–1848, 2012.

[128] K. G. Chetyrkin, Johann H. Kuhn, and M. Steinhauser. RunDec: A Mathematica package for running and decoupling of the strong coupling and quark masses. *Comput. Phys. Commun.*, 133:43–65, 2000.

[129] William Detmold, W. Melnitchouk, and Anthony William Thomas. Extraction of parton distributions from lattice QCD. *Mod. Phys. Lett. A*, 18:2681–2698, 2003.

[130] Zohreh Davoudi and Martin J. Savage. Restoration of Rotational Symmetry in the Continuum Limit of Lattice Field Theories. *Phys. Rev. D*, 86:054505, 2012.

[131] William Detmold and C. J. David Lin. Deep-inelastic scattering and the operator product expansion in lattice QCD. *Phys. Rev.*, D73:014501, 2006.

[132] William Detmold, Issaku Kanamori, C. J. David Lin, Santanu Mondal, and Yong Zhao. Moments of pion distribution amplitude using operator product expansion on the lattice. *PoS*, LATTICE2018:106, 2018.

[133] William Detmold, Anthony V. Grebe, Issaku Kanamori, C. J. David Lin, Santanu Mondal, Robert J. Perry, and Yong Zhao. A Preliminary Determination of the Second Mellin Moment of the Pion's Distribution Amplitude Using the Heavy Quark Operator Product Expansion. In *Asia-Pacific Symposium for Lattice Field Theory*, 9 2020.

[134] V. Braun and Dieter Müller. Exclusive processes in position space and the pion distribution amplitude. *Eur. Phys. J.*, C55:349–361, 2008.

[135] U. Aglietti, Marco Ciuchini, G. Corbo, E. Franco, G. Martinelli, and L. Silvestrini. Model independent determination of the light cone wave functions for exclusive processes. *Phys. Lett. B*, 441:371–375, 1998.

[136] G. Martinelli. Hadronic weak interactions of light quarks. *Nucl. Phys. B Proc. Suppl.*, 73:58–71, 1999.

[137] C. Dawson, G. Martinelli, G. C. Rossi, Christopher T. Sachrajda, Stephen R. Sharpe, M. Talevi, and M. Testa. New lattice approaches to the delta I = 1/2 rule. *Nucl. Phys. B*, 514:313–335, 1998.

[138] S. Capitani, M. Gockeler, R. Horsley, H. Oelrich, D. Petters, Paul E. L. Rakow, and G. Schierholz. Towards a nonperturbative calculation of DIS Wilson coefficients. *Nucl. Phys. B Proc. Suppl.*, 73:288–290, 1999.

[139] S. Capitani, M. Gockeler, R. Horsley, D. Petters, D. Pleiter, Paul E. L. Rakow, and G. Schierholz. Higher twist corrections to nucleon structure functions from lattice QCD. *Nucl. Phys. B Proc. Suppl.*, 79:173–175, 1999.

[140] A. J. Chambers, R. Horsley, Y. Nakamura, H. Perlt, P. E. L. Rakow, G. Schierholz, A. Schiller, K. Somfleth, R. D. Young, and J. M. Zanotti. Nucleon Structure Functions from Operator Product Expansion on the Lattice. *Phys. Rev. Lett.*, 118(24):242001, 2017.

[141] A. Hannaford-Gunn, R. Horsley, Y. Nakamura, H. Perlt, P. E. L. Rakow, G. Schierholz, K. Somfleth, H. Stüben, R. D. Young, and J. M. Zanotti. Scaling and higher twist in the nucleon Compton amplitude. *PoS*, LATTICE2019:278, 2020.

[142] Roger Horsley, Yoshifumi Nakamura, Holger Perlt, Paul E. L. Rakow, Gerrit Schierholz, Kim Somfleth, Ross D. Young, and James M. Zanotti. Structure functions from the Compton amplitude. *PoS*, LATTICE2019:137, 2020.

[143] Keh-Fei Liu and Shao-Jing Dong. Origin of difference between anti-d and anti-u partons in the nucleon. *Phys. Rev. Lett.*, 72:1790–1793, 1994.

[144] K. F. Liu, S. J. Dong, Terrence Draper, D. Leinweber, J. H. Sloan, W. Wilcox, and R. M. Woloshyn. Valence QCD: Connecting QCD to the quark model. *Phys. Rev. D*, 59:112001, 1999.

[145] Keh-Fei Liu. Parton degrees of freedom from the path integral formalism. *Phys. Rev. D*, 62:074501, 2000.

[146] Keh-Fei Liu. Parton Distribution Function from the Hadronic Tensor on the Lattice. *PoS*, LATTICE2015:115, 2016.

[147] Keh-Fei Liu. Evolution equations for connected and disconnected sea parton distributions. *Phys. Rev. D*, 96(3):033001, 2017.

[148] Keh-Fei Liu. PDF in PDFs from Hadronic Tensor and LaMET. *Phys. Rev. D*, 102(7):074502, 2020.

[149] Xiangdong Ji. Parton Physics on a Euclidean Lattice. *Phys. Rev. Lett.*, 110:262002, 2013.

[150] Xiangdong Ji. Parton Physics from Large-Momentum Effective Field Theory. *Sci. China Phys. Mech. Astron.*, 57:1407–1412, 2014.

[151] Xiangdong Ji, Jian-Hui Zhang, and Yong Zhao. More On Large-Momentum Effective Theory Approach to Parton Physics. *Nucl. Phys.*, B924:366–376, 2017.

[152] Yan-Qing Ma and Jian-Wei Qiu. Exploring Partonic Structure of Hadrons Using ab initio Lattice QCD Calculations. *Phys. Rev. Lett.*, 120(2):022003, 2018.

[153] Yu-Sheng Liu, Wei Wang, Ji Xu, Qi-An Zhang, Jian-Hui Zhang, Shuai Zhao, and Yong Zhao. Matching Quasi Generalized Parton Distributions in the RI/MOM scheme. 2019.

[154] Huey-Wen Lin. Calculating the x Dependence of Hadron Parton Distribution Functions. *PoS*, LATTICE2013:293, 2014.

[155] Huey-Wen Lin, Jiunn-Wei Chen, Saul D. Cohen, and Xiangdong Ji. Flavor Structure of the Nucleon Sea from Lattice QCD. *Phys. Rev.*, D91:054510, 2015.

[156] Jiunn-Wei Chen, Saul D. Cohen, Xiangdong Ji, Huey-Wen Lin, and Jian-Hui Zhang. Nucleon Helicity and Transversity Parton Distributions from Lattice QCD. *Nucl. Phys.*, B911:246–273, 2016.

[157] Huey-Wen Lin, Jiunn-Wei Chen, Tomomi Ishikawa, and Jian-Hui Zhang. Improved parton distribution functions at the physical pion mass. *Phys. Rev.*, D98(5):054504, 2018.

[158] Constantia Alexandrou, Krzysztof Cichy, Vincent Drach, Elena Garcia-Ramos, Kyriakos Hadjiyiannakou, Karl Jansen, Fernanda Steffens, and Christian Wiese. Lattice calculation of parton distributions. *Phys. Rev. D*, 92:014502, 2015.

[159] Constantia Alexandrou, Krzysztof Cichy, Martha Constantinou, Kyriakos Hadjiyiannakou, Karl Jansen, Fernanda Steffens, and Christian Wiese. Updated Lattice Results for Parton Distributions. *Phys. Rev.*, D96(1):014513, 2017.

[160] Constantia Alexandrou, Krzysztof Cichy, Martha Constantinou, Kyriakos Hadjiyiannakou, Karl Jansen, Haralambos Panagopoulos, and Fernanda Steffens. A complete nonperturbative renormalization prescription for quasi-PDFs. *Nucl. Phys.*, B923:394–415, 2017.

[161] Jiunn-Wei Chen, Tomomi Ishikawa, Luchang Jin, Huey-Wen Lin, Yi-Bo Yang, Jian-Hui Zhang, and Yong Zhao. Parton distribution function with nonperturbative renormalization from lattice QCD. *Phys. Rev. D*, 97(1):014505, 2018.

[162] Jian-Hui Zhang, Jiunn-Wei Chen, Luchang Jin, Huey-Wen Lin, Andreas Schäfer, and Yong Zhao. First direct lattice-QCD calculation of the x-dependence of the pion parton distribution function. *Phys. Rev. D*, 100(3):034505, 2019.

[163] Zhou-You Fan, Yi-Bo Yang, Adam Anthony, Huey-Wen Lin, and Keh-Fei Liu. Gluon Quasi-Parton-Distribution Functions from Lattice QCD. *Phys. Rev. Lett.*, 121(24):242001, 2018.

[164] Wei Wang, Jian-Hui Zhang, Shuai Zhao, and Ruilin Zhu. A Complete Matching for Quasi-distribution Functions in Large Momentum Effective Theory. 2019.

[165] Huey-Wen Lin and Rui Zhang. Lattice finite-volume dependence of the nucleon parton distributions. *Phys. Rev.*, D100(7):074502, 2019.

[166] Jiunn-Wei Chen, Huey-Wen Lin, and Jian-Hui Zhang. Pion generalized parton distribution from lattice QCD. 2019.

[167] Huey-Wen Lin. Frontiers in lattice nucleon structure. *Int. J. Mod. Phys. A*, 35(11n12):2030006, 2020.

[168] Yahui Chai et al. Parton distribution functions of Δ^+ on the lattice. 2 2020.

[169] Shohini Bhattacharya, Krzysztof Cichy, Martha Constantinou, Andreas Metz, Aurora Scapellato, and Fernanda Steffens. New insights on proton structure from lattice QCD: the twist-3 parton distribution function $g_T(x)$. 4 2020.

[170] Huey-Wen Lin, Jiunn-Wei Chen, Zhouyou Fan, Jian-Hui Zhang, and Rui Zhang. The Valence-Quark Distribution of the Kaon from Lattice QCD. 3 2020.

[171] Rui Zhang, Huey-Wen Lin, and Boram Yoon. Probing nucleon strange and charm distributions with lattice QCD. 5 2020.

[172] Zheng-Yang Li, Yan-Qing Ma, and Jian-Wei Qiu. Extraction of Next-to-Next-to-Leading-Order Parton Distribution Functions from Lattice QCD Calculations. *Phys. Rev. Lett.*, 126(7):072001, 2021.

[173] Zhouyou Fan, Xiang Gao, Ruizi Li, Huey-Wen Lin, Nikhil Karthik, Swagato Mukherjee, Peter Petreczky, Sergey Syritsyn, Yi-Bo Yang, and Rui Zhang. Isovector Parton Distribution Functions of Proton on a Superfine Lattice. 5 2020.

[174] Xiang Gao, Luchang Jin, Christos Kallidonis, Nikhil Karthik, Swagato Mukherjee, Peter Petreczky, Charles Shugert, Sergey Syritsyn, and Yong Zhao. Valence parton distribution of the pion from lattice QCD: Approaching the continuum limit. *Phys. Rev. D*, 102(9):094513, 2020.

[175] Huey-Wen Lin, Jiunn-Wei Chen, and Rui Zhang. Lattice Nucleon Isovector Unpolarized Parton Distribution in the Physical-Continuum Limit. 11 2020.

[176] Kuan Zhang, Yuan-Yuan Li, Yi-Kai Huo, Peng Sun, and Yi-Bo Yang. Continuum limit of the quasi-PDF operator using chiral fermion. 12 2020.

[177] Constantia Alexandrou, Krzysztof Cichy, Martha Constantinou, Jeremy R. Green, Kyriakos Hadjiyiannakou, Karl Jansen, Floriano Manigrasso, Aurora Scapellato, and Fernanda Steffens. Lattice continuum-limit study of nucleon quasi-PDFs. 11 2020.

[178] Constantia Alexandrou, Krzysztof Cichy, Martha Constantinou, Kyriakos Hadjiyiannakou, Karl Jansen, Aurora Scapellato, and Fernanda Steffens. Unpolarized and helicity generalized parton distributions of the proton within lattice QCD. *Phys. Rev. Lett.*, 125(26):262001, 2020.

[179] Huey-Wen Lin. Nucleon Tomography and Generalized Parton Distribution at Physical Pion Mass from Lattice QCD. 8 2020.

[180] Xiang Gao, Kyle Lee, Swagato Mukherjee, and Yong Zhao. Origin and Resummation of Threshold Logarithms in the Lattice QCD Calculations of PDFs. 2 2021.

[181] Martha Constantinou et al. Parton distributions and lattice QCD calculations: toward 3D structure. 6 2020.

[182] Gunnar S. Bali et al. Pion distribution amplitude from Euclidean correlation functions. *Eur. Phys. J.*, C78(3):217, 2018.

[183] Gunnar S. Bali, Vladimir M. Braun, Benjamin Gläßle, Meinulf Göckeler, Michael Gruber, Fabian Hutzler, Piotr Korcyl, Andreas Schäfer, Philipp Wein, and Jian-Hui Zhang. Pion distribution amplitude from Euclidean correlation functions: Exploring universality and higher-twist effects. *Phys. Rev. D*, 98(9):094507, 2018.

[184] Raza Sabbir Sufian, Joseph Karpie, Colin Egerer, Kostas Orginos, Jian-Wei Qiu, and David G. Richards. Pion Valence Quark Distribution from Matrix Element Calculated in Lattice QCD. *Phys. Rev. D*, 99(7):074507, 2019.

[185] Raza Sabbir Sufian, Colin Egerer, Joseph Karpie, Robert G. Edwards, Bálint Joó, Yan-Qing Ma, Kostas Orginos, Jian-Wei Qiu, and David G. Richards. Pion Valence Quark Distribution from Current-Current Correlation in Lattice QCD. *Phys. Rev. D*, 102(5):054508, 2020.

[186] Kostas Orginos, Anatoly Radyushkin, Joseph Karpie, and Savvas Zafeiropoulos. Lattice QCD exploration of parton pseudo-distribution functions. *Phys. Rev.*, D96(9):094503, 2017.

[187] Joseph Karpie, Kostas Orginos, Anatoly Radyushkin, and Savvas Zafeiropoulos. Parton distribution functions on the lattice and in the continuum. *EPJ Web Conf.*, 175:06032, 2018.

[188] Joseph Karpie, Kostas Orginos, and Savvas Zafeiropoulos. Moments of Ioffe time parton distribution functions from non-local matrix elements. *JHEP*, 11:178, 2018.

[189] Joseph Karpie, Kostas Orginos, Alexander Rothkopf, and Savvas Zafeiropoulos. Reconstructing parton distribution functions from Ioffe time data: from Bayesian methods to Neural Networks. *JHEP*, 04:057, 2019.

[190] Bálint Joó, Joseph Karpie, Kostas Orginos, Anatoly Radyushkin, David Richards, and Savvas Zafeiropoulos. Parton Distribution Functions from Ioffe time pseudo-distributions. *JHEP*, 12:081, 2019.

[191] Bálint Joó, Joseph Karpie, Kostas Orginos, Anatoly V. Radyushkin, David G. Richards, Raza Sabbir Sufian, and Savvas Zafeiropoulos. Pion valence structure from Ioffe-time parton pseudodistribution functions. *Phys. Rev. D*, 100(11):114512, 2019.

[192] Anatoly Radyushkin. One-loop evolution of parton pseudo-distribution functions on the lattice. *Phys. Rev.*, D98(1):014019, 2018.

[193] Jian-Hui Zhang, Jiunn-Wei Chen, and Christopher Monahan. Parton distribution functions from reduced Ioffe-time distributions. *Phys. Rev.*, D97(7):074508, 2018.

[194] Taku Izubuchi, Xiangdong Ji, Luchang Jin, Iain W. Stewart, and Yong Zhao. Factorization Theorem Relating Euclidean and Light-Cone Parton Distributions. *Phys. Rev.*, D98(5):056004, 2018.

[195] Zhouyou Fan, Rui Zhang, and Huey-Wen Lin. Nucleon Gluon Distribution Function from 2+1+1-Flavor Lattice QCD. 7 2020.

[196] Raza Sabbir Sufian, Tianbo Liu, and Arpon Paul. Gluon distributions and their applications to Ioffe-time distributions. *Phys. Rev. D*, 103(3):036007, 2021.

[197] Nikhil Karthik. Quark distribution inside a pion in many-flavor 2+1 dimensional QCD using lattice: UV listens to IR. 1 2021.

[198] John C. Collins and Davison E. Soper. Parton Distribution and Decay Functions. *Nucl. Phys. B*, 194:445–492, 1982.

[199] Iain W. Stewart and Yong Zhao. Matching the quasiparton distribution in a momentum subtraction scheme. *Phys. Rev.*, D97(5):054512, 2018.

[200] Yu-Sheng Liu, Jiunn-Wei Chen, Luchang Jin, Huey-Wen Lin, Yi-Bo Yang, Jian-Hui Zhang, and Yong Zhao. Unpolarized quark distribution from lattice QCD: A systematic analysis of renormalization and matching. 2018.

[201] Jian-Hui Zhang, Xiangdong Ji, Andreas Schäfer, Wei Wang, and Shuai Zhao. Accessing Gluon Parton Distributions in Large Momentum Effective Theory. *Phys. Rev. Lett.*, 122(14):142001, 2019.

[202] Anatoly Radyushkin. Nonperturbative Evolution of Parton Quasi-Distributions. *Phys. Lett.*, B767:314–320, 2017.

[203] A. V. Radyushkin. Quasi-parton distribution functions, momentum distributions, and pseudo-parton distribution functions. *Phys. Rev.*, D96(3):034025, 2017.

[204] Ian Balitsky, Wayne Morris, and Anatoly Radyushkin. Gluon Pseudo-Distributions at Short Distances: Forward Case. *Phys. Lett. B*, 808:135621, 2020.

[205] Ian Balitsky, Wayne Morris, and Anatoly Radyushkin. Polarized Gluon Pseudodistributions at Short Distances. 12 2021.

[206] B. L. Ioffe. Space-time picture of photon and neutrino scattering and electroproduction cross-section asymptotics. *Phys. Lett. B*, 30:123–125, 1969.

[207] V. Braun, P. Gornicki, and L. Mankiewicz. Ioffe - time distributions instead of parton momentum distributions in description of deep inelastic scattering. *Phys. Rev. D*, 51:6036–6051, 1995.

[208] Wojciech Broniowski and Enrique Ruiz Arriola. Partonic quasidistributions of the proton and pion from transverse-momentum distributions. *Phys. Rev. D*, 97(3):034031, 2018.

[209] Constantia Alexandrou, Simone Bacchio, Krzysztof Cichy, Martha Constantinou, Kyriakos Hadjiyiannakou, Karl Jansen, Giannis Koutsou, Aurora Scapellato, and Fernanda Steffens. Computation of parton distributions from the quasi-PDF approach at the physical point. *EPJ Web Conf.*, 175:14008, 2018.

[210] Huey-Wen Lin. Calculating the x Dependence of Hadron Parton Distribution Functions. *PoS*, LATTICE2013:293, 2014.

[211] Constantia Alexandrou, Krzysztof Cichy, Vincent Drach, Elena Garcia-Ramos, Kyriakos Hadjiyiannakou, Karl Jansen, Fernanda Steffens, and Christian Wiese. First results with twisted mass fermions towards the computation of parton distribution functions on the lattice. *PoS*, LATTICE2014:135, 2014.

[212] Zhouyou Fan and Huey-Wen Lin. Gluon parton distribution of the pion from lattice QCD. *Phys. Lett. B*, 823:136778, 2021.

[213] Tanjib Khan et al. Unpolarized gluon distribution in the nucleon from lattice quantum chromodynamics. *Phys. Rev. D*, 104(9):094516, 2021.

[214] Alejandro Salas-Chavira, Zhouyou Fan, and Huey-Wen Lin. First Glimpse into the Kaon Gluon Parton Distribution Using Lattice QCD. 12 2021.

[215] Craig D. Roberts, David G. Richards, Tanja Horn, and Lei Chang. Insights into the emergence of mass from studies of pion and kaon structure. *Prog. Part. Nucl. Phys.*, 120:103883, 2021.

[216] B. Adams et al. Letter of Intent: A New QCD facility at the M2 beam line of the CERN SPS (COMPASS++/AMBER). 8 2018.

[217] Seung-il Nam. Parton-distribution functions for the pion and kaon in the gauge-invariant nonlocal chiral-quark model. *Phys. Rev. D*, 86:074005, 2012.

[218] Akira Watanabe, Chung Wen Kao, and Katsuhiko Suzuki. Meson cloud effects on the pion quark distribution function in the chiral constituent quark model. *Phys. Rev. D*, 94(11):114008, 2016.

[219] Akira Watanabe, Takahiro Sawada, and Chung Wen Kao. Kaon quark distribution functions in the chiral constituent quark model. *Phys. Rev. D*, 97(7):074015, 2018.

[220] Parada T. P. Hutauruk, Ian C. Cloet, and Anthony W. Thomas. Flavor dependence of the pion and kaon form factors and parton distribution functions. *Phys. Rev. C*, 94(3):035201, 2016.

[221] Jiangshan Lan, Chandan Mondal, Shaoyang Jia, Xingbo Zhao, and James P. Vary. Parton Distribution Functions from a Light Front Hamiltonian and QCD Evolution for Light Mesons. *Phys. Rev. Lett.*, 122(17):172001, 2019.

[222] Jiangshan Lan, Chandan Mondal, Shaoyang Jia, Xingbo Zhao, and James P. Vary. Pion and kaon parton distribution functions from basis light front quantization and QCD evolution. *Phys. Rev. D*, 101(3):034024, 2020.

[223] Guy F. de Teramond, Tianbo Liu, Raza Sabbir Sufian, Hans Günter Dosch, Stanley J. Brodsky, and Alexandre Deur. Universality of Generalized Parton Distributions in Light-Front Holographic QCD. *Phys. Rev. Lett.*, 120(18):182001, 2018.

[224] Akira Watanabe, Takahiro Sawada, and Mei Huang. Extraction of gluon distributions from structure functions at small x in holographic QCD. *Phys. Lett. B*, 805:135470, 2020.

[225] Chengdong Han, Hanyang Xing, Xiaopeng Wang, Qiang Fu, Rong Wang, and Xurong Chen. Pion Valence Quark Distributions from Maximum Entropy Method. *Phys. Lett. B*, 800:135066, 2020.

[226] Lei Chang, Cédric Mezrag, Hervé Moutarde, Craig D. Roberts, Jose Rodríguez-Quintero, and Peter C. Tandy. Basic features of the pion valence-quark distribution function. *Phys. Lett. B*, 737:23–29, 2014.

[227] Lei Chang and Anthony W. Thomas. Pion Valence-quark Parton Distribution Function. *Phys. Lett. B*, 749:547–550, 2015.

[228] Chen Chen, Lei Chang, Craig D. Roberts, Shaolong Wan, and Hong-Shi Zong. Valence-quark distribution functions in the kaon and pion. *Phys. Rev. D*, 93(7):074021, 2016.

[229] Chao Shi, Cédric Mezrag, and Hong-shi Zong. Pion and kaon valence quark distribution functions from Dyson-Schwinger equations. *Phys. Rev. D*, 98(5):054029, 2018.

[230] Kyle D. Bednar, Ian C. Cloët, and Peter C. Tandy. Distinguishing Quarks and Gluons in Pion and Kaon Parton Distribution Functions. *Phys. Rev. Lett.*, 124(4):042002, 2020.

[231] Minghui Ding, Khépani Raya, Daniele Binosi, Lei Chang, Craig D Roberts, and Sebastian M. Schmidt. Symmetry, symmetry breaking, and pion parton distributions. *Phys. Rev. D*, 101(5):054014, 2020.

[232] Adam Freese, Ian C. Cloët, and Peter C. Tandy. Gluon PDF from Quark dressing in the Nucleon and Pion. 3 2021.

[233] Harvey B. Meyer and John W. Negele. Gluon contributions to the pion mass and light cone momentum fraction. *Phys. Rev. D*, 77:037501, 2008.

[234] P.E. Shanahan and W. Detmold. Gluon gravitational form factors of the nucleon and the pion from lattice QCD. *Phys. Rev. D*, 99(1):014511, 2019.

[235] A. Bazavov et al. B- and D-meson leptonic decay constants from four-flavor lattice QCD. *Phys. Rev. D*, 98(7):074512, 2018.

[236] B. Chakraborty et al. Strong-Isospin-Breaking Correction to the Muon Anomalous Magnetic Moment from Lattice QCD at the Physical Point. *Phys. Rev. Lett.*, 120(15):152001, 2018.

[237] Rajan Gupta, Yong-Chull Jang, Huey-Wen Lin, Boram Yoon, and Tanmoy Bhattacharya. Axial Vector Form Factors of the Nucleon from Lattice QCD. *Phys. Rev.*, D96(11):114503, 2017.

[238] Tanmoy Bhattacharya, Vincenzo Cirigliano, Saul Cohen, Rajan Gupta, Anosh Joseph, Huey-Wen Lin, and Boram Yoon. Iso-vector and Iso-scalar Tensor Charges of the Nucleon from Lattice QCD. *Phys. Rev.*, D92(9):094511, 2015.

[239] Tanmoy Bhattacharya, Vincenzo Cirigliano, Rajan Gupta, Huey-Wen Lin, and Boram Yoon. Neutron Electric Dipole Moment and Tensor Charges from Lattice QCD. *Phys. Rev. Lett.*, 115(21):212002, 2015.

[240] Tanmoy Bhattacharya, Saul D. Cohen, Rajan Gupta, Anosh Joseph, Huey-Wen Lin, and Boram Yoon. Nucleon Charges and Electromagnetic Form Factors from 2+1+1-Flavor Lattice QCD. *Phys. Rev.*, D89(9):094502, 2014.

[241] C.Glenn Boyd, Benjamin Grinstein, and Richard F. Lebed. Constraints on form-factors for exclusive semileptonic heavy to light meson decays. *Phys. Rev. Lett.*, 74:4603–4606, 1995.

[242] Claude Bourrely, Irinel Caprini, and Laurent Lellouch. Model-independent description of B —¿ pi l nu decays and a determination of —V(ub)—. *Phys. Rev. D*, 79:013008, 2009. [Erratum: Phys.Rev.D 82, 099902 (2010)].

[243] Wei-Yang Liu and Jiunn-Wei Chen. Chiral Perturbation for Large Momentum Effective Field Theory. 11 2020.

[244] F. E. Close and Dennis W. Sivers. Whirlpools in the Sea: Polarization of anti-Quarks in a Spinning Proton. *Phys. Rev. Lett.*, 39:1116–1120, 1977.

[245] Dennis W. Sivers. WHAT CAN WE COUNT ON? *Ann. Rev. Nucl. Part. Sci.*, 32:149–175, 1982.

[246] L.A. Harland-Lang, A.D. Martin, R. Nathvani, and R.S. Thorne. Ad Lucem: QED Parton Distribution Functions in the MMHT Framework. *Eur. Phys. J. C*, 79(10):811, 2019.

[247] Valerio Bertone, Stefano Carrazza, Nathan P. Hartland, and Juan Rojo. Illuminating the photon content of the proton within a global PDF analysis. *SciPost Phys.*, 5(1):008, 2018.

[248] Aneesh V. Manohar, Paolo Nason, Gavin P. Salam, and Giulia Zanderighi. The Photon Content of the Proton. *JHEP*, 12:046, 2017.

[249] Zheng-Yang Li, Yan-Qing Ma, and Jian-Wei Qiu. Multiplicative Renormalizability of Operators defining Quasiparton Distributions. *Phys. Rev. Lett.*, 122(6):062002, 2019.

[250] Wei Wang, Shuai Zhao, and Ruilin Zhu. Gluon quasidistribution function at one loop. *Eur. Phys. J.*, C78(2):147, 2018.

[251] Wei Wang and Shuai Zhao. On the power divergence in quasi gluon distribution function. *JHEP*, 05:142, 2018.

[252] Y. Aoki et al. Continuum Limit Physics from 2+1 Flavor Domain Wall QCD. *Phys. Rev. D*, 83:074508, 2011.

[253] A. Li et al. Overlap Valence on 2+1 Flavor Domain Wall Fermion Configurations with Deflation and Low-mode Substitution. *Phys. Rev. D*, 82:114501, 2010.

[254] M. Gong et al. Strangeness and charmness content of the nucleon from overlap fermions on 2+1-flavor domain-wall fermion configurations. *Phys. Rev. D*, 88:014503, 2013.

[255] Evan Berkowitz et al. An accurate calculation of the nucleon axial charge with lattice QCD. 4 2017.

[256] C. C. Chang et al. A per-cent-level determination of the nucleon axial coupling from quantum chromodynamics. *Nature*, 558(7708):91–94, 2018.

[257] Yi-Bo Yang, Jian Liang, Yu-Jiang Bi, Ying Chen, Terrence Draper, Keh-Fei Liu, and Zhaofeng Liu. Proton Mass Decomposition from the QCD Energy Momentum Tensor. *Phys. Rev. Lett.*, 121(21):212001, 2018.

[258] Keh-Fei Liu, Jian Liang, and Yi-Bo Yang. Variance Reduction and Cluster Decomposition. *Phys. Rev. D*, 97(3):034507, 2018.

[259] Jiunn-Wei Chen, Tomomi Ishikawa, Luchang Jin, Huey-Wen Lin, Yi-Bo Yang, Jian-Hui Zhang, and Yong Zhao. Symmetry Properties of Nonlocal Quark Bilinear Operators on a Lattice. 2017.

[260] Xiang-Dong Ji. A QCD analysis of the mass structure of the nucleon. *Phys. Rev. Lett.*, 74:1071–1074, 1995.

[261] M. Deka et al. Lattice study of quark and glue momenta and angular momenta in the nucleon. *Phys. Rev. D*, 91(1):014505, 2015.

[262] Constantia Alexandrou, Martha Constantinou, Kyriakos Hadjiyiannakou, Karl Jansen, Haralambos Panagopoulos, and Christian Wiese. Gluon momentum fraction of the nucleon from lattice QCD. *Phys. Rev. D*, 96(5):054503, 2017.

[263] T. Blum et al. Domain wall QCD with physical quark masses. *Phys. Rev. D*, 93(7):074505, 2016.